In silico modelling and simulation of tumour growth and response to radiotherapy

Carlos Sosa Marrero

DOCTORAT BRETAGNE LOIRE / MATHSTIC

UNIVERSITÉ DE RENNES 1

THÈSE DE DOCTORAT DE

L'UNIVERSITÉ DE RENNES 1

ÉCOLE DOCTORALE N° 601
Mathématiques et Sciences et Technologies de l'Information et de la Communication
Spécialité : *AST - Signal, Image, Vision*

Par
Carlos SOSA MARRERO

Modélisation et simulation numérique de croissance tumorale et réponse à la radiothérapie

Thèse présentée et soutenue à Rennes, le 7 juillet 2021
Unité de recherche : LTSI - UMR 1099

Rapporteurs avant soutenance :

Fabrice MÉRIAUDEAU — PU, Université de Bourgogne, Dijon
Víctor M. PÉREZ GARCÍA — Full professor, Universidad de Castilla-La Mancha, Ciudad Real, Espagne

Composition du Jury :

Président :	Stéphane SUPIOT	PU/PH, Université de Nantes, Nantes
Examinateurs :	Fabrice MÉRIAUDEAU	PU, Université de Bourgogne, Dijon
	Víctor M. PÉREZ GARCÍA	Full professor, Universidad de Castilla-La Mancha, Ciudad Real, Espagne
	Beatriz SÁNCHEZ NIETO	Associate professor, Pontificia Universidad Católica de Chile, Santiago, Chili
	Elisa SCALCO	Permanent researcher, Istituto di Tecnologie Biomediche - CNR, Milan, Italie
Dir. de thèse :	Renaud DE CREVOISIER	PU/PH, Université de Rennes 1, Rennes
Co-dir. de thèse :	Oscar ACOSTA	MCU, Université de Rennes 1, Rennes

Invité(s) :

François PARIS — DR, Université de Nantes, Nantes

Acknowledgements

Je voudrais remercier dans les lignes suivantes toutes les personnes qui, d'une façon ou une autre, m'ont aidé à réaliser cette thèse doctorale. Vous avez été très nombreux et j'aurais voulu tous vous citer, mais l'espace dont je dispose est limité et ma mémoire commence à me trahir. Je vous présente mes excuses pour tout oubli éventuel.

First of all, I would like to thank every member of the jury for having accepted the invitation. It was such an honour for me. Thank you, Fabrice Mériaudeau, Víctor M. Pérez Garcia, Beatriz Sánchez Nieto, Elisa Scalco, Stéphane Supiot and François Paris, for the quality of your comments, your questions and your suggestions.

Je voudrais ensuite remercier sincèrement mes directeurs de thèse pour la confiance qu'ils m'ont accordée dès mon premier stage de master 1. Merci, Renaud, pour ta gentillesse, pour tes conseils et pour tes explications cliniques. Merci aussi, Óscar, pour ton dynamisme, tes nombreuses idées scientifiques et ton optimisme.

Je tiens aussi à remercier mes collègues et anciens collègues du LTSI pour tous les moments agréables que nous avons vécus au sein du laboratoire ou dans les rues rennaises. Mes pensées vont d'abord à son directeur, Lotfi. Merci beaucoup pour l'accueil très chaleureux que tu réserves à tous les membres du laboratoire. Ensuite, je voudrais exprimer ma gratitude aux doctorants avec qui j'ai eu le plaisir de travailler au bureau. Je pense à ceux qui m'ont montré le chemin, Eugenia et Jérémy; à Pierre, qui a commencé cette aventure au même temps que moi, et à Hilda et Safaa, qui doivent maintenant prendre le relais. Je remercie aussi les nombreux stagiaires et ingénieurs qui m'ont accompagné tout au long de ces cinq dernières années. Vous avez tous été un rayon de soleil. Je voudrais aussi remercier les futurs docteurs Aurélien, Gautier, Marion, Maureen, Erwan, Louis et Clément pour les moments amicaux que nous avons passés à table. Je vous souhaite tout le meilleur pour la suite. Quisiera dar también las gracias por los buenos momentos vividos a Gustavo, Miguel, Pablo, Henry, Kimi, Cristhyne y Remo, con quienes me une la nostalgia de una patria lejana y una lengua común. Finalement, j'exprime ma gratitude aux collègues avec qui j'ai pu assurer des enseignements tout au long de ces trois dernières années. Merci, spécialement, Orlane. C'était très agréable de préparer les différentes séances de cours avec toi.

Je tiens également à remercier mes professeurs et amis du master Calcul scientifique et modélisation. Je garde un excellent souvenir des enseignements suivis, qui m'ont permis de commencer cette thèse, ainsi que des nombreux moments conviviaux que nous avons passés.

Je voudrais aussi remercier Brice et Benoît d'être venus m'accompagner le jour de ma soutenance de thèse, mais surtout d'avoir été ma famille en France pendant ces cinq dernières années. Malgré la distance géographique qui nous sépare actuellement, je vous sens toujours très proches de mon cœur.

Por último, quisiera dar las gracias a mis amigos y a mi familia, a mis tíos, a mis primos y a mis padres, por su cariño y su apoyo constante a pesar de la distancia. Gracias, de verdad, por entender mis ausencias y por hacerme sentir que volver a Tenerife siempre valiera la pena.

Table of Contents

List of Figures

List of Tables

RÉSUMÉ EN FRANÇAIS

Modélisation et simulation numérique de croissance tumorale et réponse a la radiotherapie

Le cancer de la prostate est le deuxième type de cancer le plus fréquent et la cinquième cause de décès par cancer chez les hommes. On estime qu'en 2018, près de 1,3 million de nouveaux cas ont été diagnostiqués, faisant 359 000 décès dans le monde [1]. Bien que plusieurs options thérapeutiques existent, la radiothérapie externe (RTE) est devenue le standard clinique pour traiter le cancer localisé de la prostate. Typiquement, une dose totale comprise entre 74 et 80 Gy est prescrite. Pour limiter les effets secondaires, elle est délivrée en plusieurs fractions pendant 7 ou 8 semaines. Le contrôle local de la tumeur est atteint dans la plupart des cas. Cependant, il a été rapporté que 0-10 %, 10-20 % et 30-40 % des patients avec, respectivement, des tumeurs à risque faible, intermédiaire et élevé (selon la classification de D'Amico [2]) subissent une récidive biochimique au bout de 5 ans. Pour réduire ces pourcentages, des traitements hypofractionnés ont été récemment proposés [3–8]. Ils suggèrent d'augmenter la dose par fraction, réduisant ainsi le nombre de séances d'irradiation. Cependant, les connaissances de la réponse des patients à ces nouveaux schémas sont encore limitées.

Les modèles dose-effet [9–11], basés sur des courbes de probabilité de contrôle tumoral (TCP), ont été utilisés dans le passé pour prédire le risque de récidive. Cependant, ils ont une intégration limitée de l'hétérogénéité inter-patient. Des approches radiomiques, basées sur des biomarqueurs d'image, sont apparues ces dernières années comme des outils attrayants pour prédire la récidive tumorale et la survie [12–14]. Cependant, elles ont montré des performances limitées, elles sont généralement basées sur des méthodes d'apprentissage automatique complexes, ce qui complique l'interprétabilité, et elles ont besoin d'une grande quantité de données de population.

La modélisation mécaniste apparaît comme une approche alternative basée sur l'intégration des différents mécanismes radiobiologiques sous-jacents au comportement de la récidive biochimique. Grâce à la simulation *in silico*, elle permet de mieux comprendre la réponse des patients cancéreux à un certain schéma d'irradiation et leurs résultats sont facilement explicables. Les capacités prédictives des modèles mécanistes ont déjà été montrées dans d'autres contextes [15, 16].

De nombreux mécanismes radiobiologiques ont été considérés comme participant à la survie de la tumeur après radiothérapie et à l'éventuelle récidive. En particulier, ceux liés aux 5 R (réoxygénation, repeuplement, réparation de l'ADN, radiosensibilité et redistribution dans le cycle cellulaire) ont été minutieusement étudiés [17]. La modulation de la résistance tumorale aux rayonnements est liée, au moins, à l'hypoxie et à une angiogenèse anormale entraînant la réoxygénation du tissu [18–20], à un taux élevé de prolifération/repeuplement des cellules tumorales [21–23] et à une faible radiosensibilité intrinsèque des cellules tumorales [24–26], associée à une distribution prépondérante du cycle cellulaire dans la phase radiorésistante S [27]. La catastrophe mitotique [28], considérée comme le type principal de

mort cellulaire après irradiation, peut également jouer un rôle majeur dans le contrôle tumoral [29, 30].

Un grand nombre de modèles numérique mécanistes combinant certains de ces processus ont déjà été proposés dans la littérature [31–34]. En particulier, le modèle d'Espinoza *et al.* intègre un grand nombre des mécanismes radiobiologiques majeurs. Cependant, il n'a pas été testé, à notre connaissance, sur des coupes histopathologiques. De plus, les valeurs des paramètres du modèle restent incertaines, car elles peuvent varier considérablement dans la littérature. Également, bien que l'impact de différentes stratégies de radiothérapie ait été exploré [35], sa sortie de simulation représentant un contrôle clinique de la tumeur après des schémas d'irradiation de la prostate conventionnels et hypofractionnés n'a pas été clairement identifiée.

En outre, certains des mécanismes radiobiologiques susceptibles de jouer un rôle majeur dans le contrôle des tumeurs, comme la catastrophe mitotique et la distribution du cycle cellulaire permettant la simulation d'une radiosensibilité dépendant de la phase pour les cellules tumorales, n'ont pas été inclus. Ce problème est applicable à d'autres modèles de la littérature. À notre connaissance, aucun travail antérieur n'a intégré simultanément dans un seul modèle une oxygénation dynamique, la catastrophe mitotique et la réponse des cellules tumorales à l'irradiation dépendant de la phase du cycle cellulaire.

De plus, les modèles mécanistes de réponse tumorale contiennent généralement un grand nombre de paramètres difficiles à mesurer *in vivo* ou même *in vitro*, ce qui complique la calibration et la validation. Une analyse de sensibilité peut être effectuée pour évaluer l'impact de tous les paramètres d'un modèle et ensuite construire une version réduite en incluant uniquement les facteurs les plus importants. Plusieurs exemples peuvent être trouvés dans d'autres contextes biomédicaux [36–38]. Bien que la contribution indépendante de différents mécanismes radiobiologiques ait été évaluée pour certains cas à travers des courbes de TCP ou de densité tumorale [31, 32, 39], une étude exhaustive pour identifier précisément l'impact de chaque paramètre n'a pas encore été réalisée, à notre connaissance, pour aucun des modèles mécanistes de réponse tumorale de la littérature.

Les objectifs de cette thèse étaient donc :

1. d'adapter le modèle d'Espinoza *et al.*, afin qu'il puisse être initialisé avec des coupes histopathologiques de prostate
2. de simuler des schémas d'irradiation de prostate conventionnels et hypofractionnés en utilisant l'adaptation du modèle d'Espinoza *et al.*
3. de développer un modèle *in silico* original de croissance tumorale et de réponse à l'irradiation, intégrant les principaux mécanismes radiobiologiques de la littérature dans le contexte du cancer de la prostate
4. de réaliser une analyse de sensibilité exhaustive de ce modèle original complet
5. de proposer un modèle simplifié basé sur les résultats de l'analyse de sensibilité et équivalent en termes de TCP, de densité cellulaire tumorale et de prédiction de récidive biochimique
6. de prédire la récidive biochimique après radiothérapie en utilisant les sorties de simulation obtenues avec le modèle réduit et de comparer les résultats avec ceux d'une approche radiomique classique
7. de tester des schémas d'irradiation alternatifs personnalisés en utilisant le modèle réduit.

Dans un premier temps, le modèle d'Espinoza *et al.* a été adapté et implémenté dans le logiciel de simulation Netlogo [40]. Il a été initialisé avec des configurations réalistes obtenues à partir de

coupes histopathologiques de la prostate. Cette adaptation considérait 4 mécanismes radiobiologiques: (i) l'oxygénation statique, modélisée avec une équation de réaction-diffusion; (ii) la prolifération de cellules tumorales, basée sur un facteur de prolifération; (iii) la réponse à l'irradiation des cellules tumorales, dépendante de l'oxygène et considérant le modèle linéaire-quadratique (MLQ) [41–43], et (iv) la résorption des cellules mortes, donnée par une constante de résorption. Des schémas d'irradiation de la prostate conventionnels et hypofractionnés ont été simulés et les doses totales pour atteindre le contrôle tumoral *in silico* ont été étudiées.

Comme cette première approche présentait plusieurs faiblesses, un modèle mécaniste original de croissance tumorale et réponse à la RTE a été développé et implémenté en C++. Il intégrait 5 mécanismes radiobiologiques : (i) l'oxygénation dynamique, modélisée avec une équation de réaction-diffusion et incluant la mort hypoxique; (ii) la division des cellules tumorales, en considérant leur cycle cellulaire; (iii) l'angiogenèse gouvernée par la concentration de VEGF (*Vascular endothelial growth factor*), donnée par une équation de réaction-diffusion; (iv) la division des cellules saines et (v) la réponse à l'irradiation, dépendante de la phase du cycle cellulaire et de l'oxygène, basée sur le MLQ et incluant l'arrêt dans le cycle et la catastrophe mitotique. Une analyse de sensibilité exhaustive à l'aide de la méthode de *screening* de Morris a été réalisée. Les courbes TCP du modèle complet et de 15 versions simplifiées excluant certains mécanismes ont été comparées. Sur la base de ces résultats, une version réduite, équivalente en termes de densité cellulaire tumorale et de TCP, a été proposée.

Ce modèle réduit original a été utilisé pour prédire la récidive biochimique dans une cohorte de 76 patients atteints d'adénocarcinome prostatique localisé traités par RTE. À cet effet, des tissus numériques 2D représentant les individus de la cohorte ont été construits à partir de caractéristiques d'IRM multiparamétriques (IRMmp) pré-traitement. Ensuite, le protocole de radiothérapie administré à chaque patient a été simulé sur le tissu virtuel correspondant et l'évolution du nombre de cellules tumorales au cours des 8 semaines de traitement a été obtenue. Une régression logistique a été réalisée pour prédire la récidive biochimique directement à partir des caractéristiques des IRMmp pré-traitement ou du nombre *in silico* de cellules tumorales à la fin du traitement et les résultats ont été comparés.

Ce manuscrit est basé sur des articles rédigés en tant que premier auteur précédemment publiés dans des revues et des conférences internationales ou des travaux en préparation. Il est divisé en 4 parties et contient 6 chapitres structurés comme suit :

Partie I

— Le **chapitre 1** présente le contexte clinique de cette thèse ainsi qu'un état de l'art des différentes approches de modélisation de la réponse tumorale à l'irradiation. Tout d'abord, une brève description du cancer de la prostate et des options thérapeutiques les plus courantes est fournie. En particulier, les principes de la RTE sont expliqués. Deuxièmement, un état de l'art des différentes approches de prédiction de récidive biochimique après radiothérapie est fourni. Des modèles dose-effet et radiomiques sont présentés et leurs faiblesses sont expliquées. Ensuite, les principes de la modélisation mécaniste sont décrits et plusieurs exemples de modèles *in silico* de croissance tumorale et de réponse à l'irradiation de la littérature sont présentés. Les enjeux méthodologiques de ce type d'approche sont largement discutés. En particulier, les faiblesses dues au grand nombre de paramètres des modèles mécanistes et les bases des analyses de sensibilité sont expliquées.

— Le **chapitre 2** décrit les motivations et les objectifs de cette thèse.

Partie II

— Le **chapitre 3**, basé sur un article en préparation, décrit l'adaptation du modèle mécaniste de réponse tumorale à la radiothérapie d'Espinoza *et al.* Les résultats d'une analyse de sensibilité locale effectuée pour déterminer l'impact de chaque paramètre sur la mort des cellules tumorales sont rapportés. Une comparaison des résultats du modèle en termes d'hypoxie avec des données cliniques prostatiques de la littérature est présentée. Les résultats des simulations de différents protocoles d'irradiation de prostate (conventionnels et hypofractionnés) considérant 6 valeurs de radiosensibilités intrinsèques publiées sont rapportés. Les doses totales simulées pour atteindre le contrôle de la tumeur dans les rangs cliniques sont identifiées.

Partie III

— Le **chapitre 4**, basé sur un article de revue publié précédemment, présente tout d'abord un modèle original de croissance tumorale et réponse à l'irradiation intégrant les principaux mécanismes radiobiologiques de la littérature. Ensuite, les résultats de l'analyse de sensibilité réalisée sur des tissus numériques de prostate à l'aide de la méthode de *screening* de Morris sont rapportés. Des comparaisons des courbes TCP du modèle complet et de 15 versions simplifiées excluant certains mécanismes sont présentées. Sur la base des résultats de l'analyse de sensibilité et des courbes TCP, un modèle réduit de réponse tumorale est proposé. Enfin, une application potentielle du modèle dans un contexte clinique est décrite.

— Le **chapitre 5**, basé sur un article de conférence évalué par des pairs publié précédemment, explore l'utilisation du modèle mécaniste réduit de croissance tumorale et réponse à l'irradiation pour prédire la récidive biochimique dans le contexte du cancer de la prostate. Les résultats pour une cohorte de patients atteints d'adénocarcinome prostatique localisé ayant été traités par RTE sont présentés. Ils sont comparés aux prédictions de récidive directement obtenues à partir de caractéristiques d'IRMmp suivant une approche radiomique conventionnelle.

Partie IV

— Le **chapitre 6** comprend une discussion générale sur les principaux résultats et contributions de cette thèse. Ses principales faiblesses sont également expliquées et des suggestions de travaux futurs sont proposées.

Les principales contributions de cette thèse sont donc :

1. l'adaptation et la comparaison avec des données cliniques prostatiques d'un modèle existant de réponse tumorale à l'irradiation
2. le développement d'un modèle numérique original de croissance tumorale et réponse à la radiothérapie intégrant les principaux mécanismes radiobiologiques de la littérature
3. l'identification des paramètres et mécanismes radiobiologiques ayant l'impact le plus important sur la densité de cellules tumorales et la TCP
4. le développement d'un modèle mécaniste réduit intégrant uniquement les mécanismes radiobiologiques les plus importants
5. la génération de prédictions de récidive biochimique significativement meilleures en utilisant le modèle mécaniste réduit, par rapport à une approche radiomique conventionnelle, dans le contexte de la RTE du cancer de la prostate.

Cette thèse a été financée par la Région Bretagne et la FHU TECH-SAN.

Acronyms

— 3D conformal radiotherapy (3D-CRT)
— 4D transperineal ultrasound (4D-TPUS)
— Adaptive synthetic oversampling (ADASYN)
— Apparent diffusion coefficient (ADC)
— Androgen deprivation therapy (ADT)
— Area under the curve (AUC)
— Cone beam computed tomography (CBCT)
— Cluster of differentiation 31 (CD31)
— Clinical linear accelerator (CLINAC)
— Computed tomography (CT)
— Digital rectal examination (DRE)
— External beam radiation therapy (EBRT)
— Electromagnetic transponders (EMT)
— Edited nearest neighbour (ENN)
— Fluorodeoxyglucose (FDG)
— False positive rate (FPR)
— Hematoxylin-eosin-saffron (HES)
— High-intensity focused ultrasound (HIFU)
— Image-guided intensity-modulated radiotherapy (IG-IMRT)
— Institutional review board (IRB)
— Linear-quadratic model (LQM)
— Multi-formalism modeling and simulation library (M2SL)
— Multileaf collimator (MLC)
— Multi-parametric magnetic resonance imaging (mpMRI)
— Magnetic resonance imaging (MRI)
— Magnetic resonance dynamic contrast enhanced (MR-DCE)
— One-at-a-time (OAT)
— Oxygen enhancement ratio (OER)
— Partial differential equation (PDE)
— Positron emission tomography (PET)
— Prostate specific antigen (PSA)
— Receiver operating characteristic (ROC)
— Region of interest (ROI)
— Radical prostatectomy (RP)
— Relative sensitivity coefficient (RSC)

— Main effect index (SI)
— Synthetic minority oversampling technique (SMOTE)
— Stereotactic radiosurgery (SRS)
— Tumour angiogenesis factors (TAF)
— Tumour control probability (TCP)
— Tumour, node and metastasis (TNM)
— True positive rate (TPR)
— Treatment planning system (TPS)
— Total effect index (TSI)
— Union for International Cancer Control (UICC)
— Vascular endothelial growth factor (VEGF)
— Volumetric modulated arc therapy (VMAT)

INTRODUCTION

Prostate cancer ranks as the second most frequent type of cancer and the fifth leading cause of cancer death in men. It has been estimated that, in 2018, almost 1.3 million new cases were diagnosed, causing 359 000 fatalities, worldwide [1]. Although several therapeutic options exist, external beam radiotherapy (EBRT) has emerged as the clinical standard to treat localised prostate cancer. Typically, a total dose between 74 and 80 Gy is prescribed. To limit side-effects, it is delivered in several fractions during 7 or 8 weeks. Local tumour control is achieved in most of the cases. However, it has been reported that 0-10%, 10-20% and 30-40% of patients with, respectively, low, intermediate and high risk tumours (according to the D'Amico classification [2]) experience biochemical recurrence within 5 years. To reduce these percentages, hypofractionated treatments have been recently proposed [3–8]. They suggest increasing the dose per fraction, thus reducing the number of irradiation sessions. However, the knowledge of the response of patients to these new schedules is still limited.

Dose-effect models [9–11], based on tumour control probability (TCP) curves, have been used in the past to predict the risk of recurrence. However, they have limited integration of inter-patient heterogeneity. Radiomics approaches, based on image biomarkers, have emerged in recent years as appealing tools to predict tumour recurrence and survival [12–14]. However, they have shown limited performance, they are usually based on complex machine learning methods, which complicates interpretability, and they need a large amount of population data.

Mechanistic modelling appears as an alternative approach based on the integration of the different radiobiological mechanisms underlying the behaviour of biochemical recurrence. Through *in silico* simulation, it allows to better comprehend the response of cancer patients to a certain irradiation schedule and their results are easily explainable. The predictive capabilities of mechanistic models have already been shown in other contexts [15, 16].

Numerous radiobiological mechanisms have been considered to participate in tumour survival after radiotherapy and later recurrence. In particular, those related to the 5 R's (reoxygenation, repopulation, DNA repair, radiosensitivity and redistribution in the cell cycle) have been thoroughly studied [17]. Modulation of tumour radiation resistance is thought to be related, at least, to hypoxia and abnormal angiogenesis resulting in the reoxygenation of the tissue [18–20], a high rate of proliferation/repopulation of tumour cells [21–23] and a low intrinsic radiosensitivity of tumour cells [24–26], associated with a preponderant cell cycle distribution in the radioresistant phase S [27]. Mitotic catastrophe [28], considered to be the main type of cell death after irradiation, may also play a major role in tumour control [29, 30].

A large number of *in silico* mechanistic models combining some of these processes have already been proposed in the literature [31–34]. In particular, the model of Espinoza *et al.* integrates a great number of the major radiobiological mechanisms. However, it has not been tested, to our knowledge, on histopathological specimens. Moreover, the values of the model parameters remain uncertain, as they can widely vary in the literature. In addition, although the impact of different radiotherapy strategies has

been explored [35], its simulation endpoint representing clinical tumour control after conventional and hypofractionated prostate irradiation schedules has not been clearly identified.

Furthermore, some of the radiobiological mechanisms which may play a major role in tumour control, such as mitotic catastrophe and cell cycle distribution allowing the simulation of a phase-dependent radiosensitivity for tumour cells were not included. This issue is applicable to other models of the literature. To our knowledge, no previous work has simultaneously integrated dynamic oxygenation, mitotic catastrophe and cell-cycle-phase-dependent response of tumour cells to irradiation in a single comprehensive model.

Moreover, mechanistic models of tumour response usually contain a large number of parameters difficult to measure *in vivo* or even *in vitro*, which hampers calibration and validation. Sensitivity analysis can be performed to evaluate the impact of all the parameters of a model and subsequently build a reduced version including only the most relevant factors. Multiple examples can be found in other biomedical contexts [36–38]. Although the independent contribution of different radiobiological mechanisms has been evaluated for some cases through TCP or tumour density curves [31, 32, 39], a thorough study to precisely identify the impact of each parameter has not been performed yet, to our knowledge, for any of the mechanistic models of tumour response of the literature.

The objectives of this thesis were thus:

1. to adapt the model of Espinoza *et al.*, so that it can be initialised with prostate histopathological specimens
2. to simulate conventional and hypofractionated prostate irradiation schedules using the adaptation of the model of Espinoza *et al.*
3. to develop an original *in silico* model of tumour growth and response to irradiation, integrating the main radiobiological mechanisms of the literature in the context of prostate cancer
4. to perform an exhaustive sensitivity analysis of this original comprehensive model
5. to propose a simplified model based on the results of the sensitivity analysis and equivalent in terms of TCP, tumour cell density and prediction of biochemical recurrence
6. to predict biochemical recurrence after radiotherapy using simulation outputs obtained with the reduced model and to compare the results with those of a classical radiomics approach
7. to test personalised alternative irradiation schedules using the reduced model.

As a first step, the model of Espinoza *et al.* was adapted and implemented in the simulation software Netlogo [40]. It was initialised with realistic configurations obtained from prostate histopathological specimens. This adaptation considered 4 radiobiological mechanisms: (i) static oxygenation, modelled with a reaction-diffusion equation; (ii) proliferation of tumour cells, based on a proliferation factor; (iii) oxygen-dependent response to irradiation, considering the linear-quadratic model (LQM) [41–43], and (iv) resorption of dead cells, given by a resorption constant. Conventional and hypofractionated prostate irradiation schedules were simulated and *in silico* total doses to achieve tumour control studied.

Since this first approach presented several limitations, an original mechanistic *in silico* model of tumour response to EBRT was developed and implemented in C++ using the in-house simulation library M2SL [44]. It integrated 5 radiobiological mechanisms: (i) dynamic oxygenation, modelled with a reaction-diffusion equation and including hypoxic death; (ii) division of tumour cells, considering their cell-cycle;

(iii) angiogenesis driven by the VEGF (Vascular endothelial growth factor) concentration, given by a reaction-diffusion equation; (iv) division of healthy cells and (v) cell-cycle-phase-and-oxygen-dependent response to irradiation, based on the LQM and considering cycle arrest and mitotic catastrophe. A thorough sensitivity analysis using the Morris screening method, was performed. TCP curves of the comprehensive model and 15 simplified versions excluding certain mechanisms were compared. Based on these results, a reduced version, equivalent in terms of tumour cell density and TCP, was proposed.

This original reduced model was used to predict biochemical recurrence in a cohort of 76 patients with localised prostate adenocarcinoma having undergone EBRT. For this purpose, 2D digital tissues representing the individuals of the cohort were built from pre-treatment mpMRI features. Then, the radiotherapy protocol administered to each patient was simulated on the corresponding virtual tissue and the evolution of the number of tumour cells throughout the 8 weeks of treatment was obtained. Logistic regression was performed to predict biochemical recurrence directly from pre-treatment mpMRI features or from the *in silico* number of tumour cells at the end of the treatment and results were compared.

This manuscript is based on first-authored articles previously published on international journals and conferences or works in preparation for submission. It is divided in 4 parts and contains 6 chapters structured as follows:

Part I

— **Chapter 1** presents the clinical context of this thesis as well as a state of the art of the different approaches of modelling the tumour response to irradiation. Firstly, a brief description of prostate cancer and the most common therapeutic options is provided. In particular, the principles of EBRT are explained. Secondly, a state of the art of the different approaches of prediction of biochemical recurrence after radiotherapy is provided. Dose-effect and radiomics models are presented and their limitations are explained. Then, the principles of mechanistic modelling are described and several examples of *in silico* models of tumour growth and response to irradiation of the literature are presented. The methodological challenges of this kind of approach are widely discussed. In particular, limitations due to the large number of parameters of mechanistic models and the basis of sensitivity analysis are explained.

— **Chapter 2** describes the motivations and objectives of this thesis.

Part II

— **Chapter 3**, based on an article in preparation for submission, describes the adaptation of an existing mechanistic model of tumour response to radiotherapy. The results of a local sensitivity analysis performed to determine the impact of each parameter on tumour cell death are reported. A comparison of the outcomes of the model in terms of hypoxia with prostate clinical data from the literature is shown. The results of simulations of various prostate irradiation schedules (conventional and hypofractionated) considering 6 different published intrinsic radiosensitivity values are presented. Simulated total doses to achieve tumour control within the clinical ranges are identified.

Part III

— **Chapter 4**, based on a previously published journal article, presents firstly an original mechanistic *in silico* model of tumour growth and response to irradiation integrating the major radiobiological mechanisms of the literature. Then, the results of the sensitivity analysis performed on prostate

computational tissues using the Morris screening method are reported. Comparisons of TCP curves of the comprehensive model and 15 simplified versions excluding certain mechanisms are shown. Based on the results of the sensitivity analysis and the TCP curves, a reduced model of tumour response is proposed. Finally, a potential application of the model as a useful tool in a clinical context is described.

— **Chapter 5**, based on a previously published peer-reviewed conference paper, explores the use of the reduced mechanistic *in silico* model of tumour growth and response to irradiation to predict biochemical recurrence in the context of prostate cancer. Results for a cohort of localised prostate adenocarcinoma patients having undergone EBRT are presented. They are compared with recurrence predictions directly obtained from mpMRI features following a conventional radiomics approach.

Part IV

— **Chapter 6** includes a general discussion on the main results and contributions of this thesis. Its major limitations are also explained and suggestions about future work are offered.

The main contributions of this thesis are therefore:

1. the adaptation and comparison with prostate clinical data of an existing model of tumour response to irradiation
2. the development of an original mechanistic model of tumour growth and response to radiotherapy integrating the main radiobiological mechanisms of the literature
3. the identification of the radiobiological parameters and mechanisms having the most important impact on tumour cell density and TCP
4. the development of a reduced mechanistic model integrating only the most important radiobiological mechanisms
5. the generation of significantly better biochemical recurrence predictions using the reduced mechanistic model, compared to a conventional radiomics approach, in the context of prostate cancer EBRT.

This thesis was funded by the Brittany Region and FHU TECH-SAN.

Part I

Clinical context, state of the art and objectives

Chapter 1

Clinical context and state of the art

This chapter presents the clinical and methodological context of this thesis. Firstly, a brief description of prostate cancer and the available therapeutic options is provided. In particular, the principles and limitations of external beam radiation therapy are discussed. This is followed by a state of the art of the most important approaches of prediction of biochemical recurrence after radiotherapy, namely dose-effect, radiomics and mechanistic models. Their methodological challenges, especially those of mechanistic modelling, are widely discussed.

1.1 Prostate cancer

1.1.1 Prostate anatomy

The prostate is a gland of the male reproductive system situated in the pelvic cavity, in front of the rectum, below the bladder and surrounding the urethra, as shown in Fig. 1.1. In healthy adults, it has an average size around 4 cm × 3 cm and its weight ranges between 20 and 25 g. It is formed of both glandular and connective tissue and surrounded by an elastic, fibromuscular capsule. Its main function is the production of the prostatic fluid. This liquid contains several enzymes such as the prostate specific antigen (PSA) and represents about a third of the total volume of semen. Furthermore, prostate muscles ensure that the seminal fluid is forcefully pressed into the urethra and then expelled outwards during ejaculation.

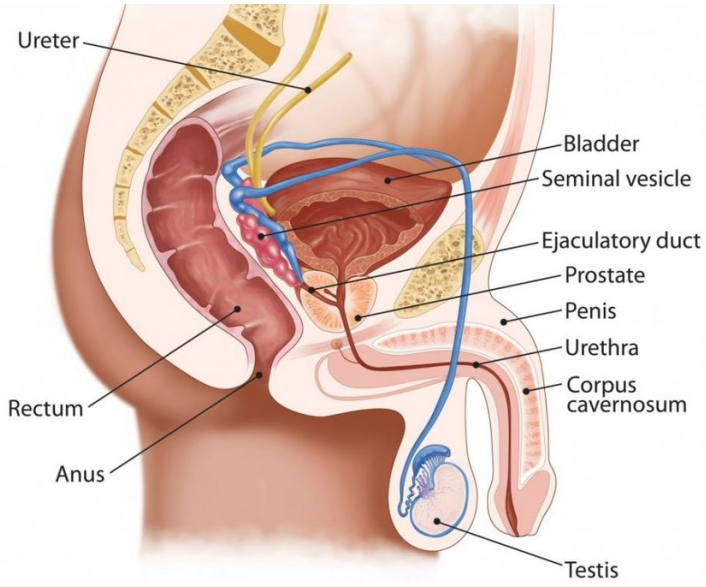

Figure 1.1 – Anatomy of the male reproductive system (source: www.bladderclinic.com.au)

1.1.2 Epidemiology

It has been estimated that, in 2018, almost 1.3 million new cases of prostate cancer were diagnosed, causing 359,000 deaths worldwide [1]. Prostate cancer ranks thus as the second most frequent type of cancer (13.5%) and the fifth leading cause of cancer death in men (6.5%). In France, prostate cancer is by far the most common type of cancer in men. It is estimated that circa 55,000 new cases are diagnosed every year, being the cause of, approximately, 8,000 annual deaths.

1.1.3 Diagnosis

Prostate cancer is typically first detected through digital rectal examination (DRE) or a blood test measuring the levels of PSA. DRE is the standard way to define texture, shape and size and of the

prostate. It is simple and complication-free, but subjective as it depends on the examiner. PSA has been traditionally used as a marker of prostate cancer. Most healthy men have PSA levels below 4 ng/ml. This concentration rises when prostate cancer develops.

However, DRE and PSA test have relatively low sensitivity, and they do not differentiate between aggressive and indolent disease. For these reasons, when an abnormal lump is found through DRE examination or when a blood test reveals high PSA levels, prostate biopsy may be performed. Definitive diagnosis is only confirmed after histopathological verification of adenocarcinoma.

1.1.4 Staging

The Gleason grading system allows to classify prostate tumours based on their microscopic appearance [45]. The following 5 patterns are defined:

- Pattern 1: the cancerous prostate closely resembles normal prostate tissue. The glands are small, well-formed, and closely packed.
- Pattern 2: the tissue still has well-formed glands. However, they are larger and have more tissue between them, implying that the stroma has increased.
- Pattern 3: the tissue still has recognizable glands, but the cells are darker. At high magnification, some of these cells have left the glands and are beginning to invade the surrounding tissue or having an infiltrative pattern.
- Pattern 4: the tissue has few recognizable glands. Many cells are invading the surrounding tissue in neoplastic clumps.
- Pattern 5: the tissue does not have any or only a few recognizable glands. There are often just sheets of cells throughout the surrounding tissue.

The Gleason score is defined as the sum of the two most frequent patterns observed during the histopathological analysis.

In the early stage, the tumour is located within the prostate. However, as the disease progresses, it can expand to neighbouring organs and tissues as well as more distant locations, such as the lymph nodes or the the bones. The process by which cancer cells spread to other parts of the body is called metastasis. Tumour extension is usually expressed as being at a certain T stage using the tumour, node and metastasis (TNM) classification system published by the Union for International Cancer Control (UICC) [46]. It defines four T stages with various subcategories indicating tumour size and location:

- T1: the tumour is too small to be detected on a scan or felt through DRE:
  - T1a: the tumour is found in less than 5% of the resected prostate tissue
  - T1b: the tumour is found in more than 5% of the resected prostate tissue
  - T1c: the tumour is found in a needle biopsy performed due to an elevated PSA level
- T2: the tumour can be felt through DRE but it is still confined to the prostate:
  - T2a: the tumour is found in only half or less than half of one of the prostate lobes
  - T2b: the tumour is found in more than half of one lobe, but not in both
  - T2c: the tumour is found in both lobes
- T3: the tumour has spread throughout the prostate capsule
  - T3a: the tumour has spread through the capsule but not to the seminal vesicles
  - T3b: the tumour has invaded one or both seminal vesicles

— T4: the tumour has invaded other nearby structures, such as the rectum, the bladder or the pelvic wall

Based on the Gleason score, the T stage and the PSA level, the D'Amico classification [2] assigns prostate cancer patients to low, intermediate and high risk categories as follows:

— Low risk: T1 to T2a stages, Gleason score ≤ 6 and PSA < 10 ng/ml.
— Intermediate risk: T2b stage or Gleason score $= 7$ or 10 ng/ml $\leq$ PSA ≤ 20 ng/ml.
— High risk: T2c to T4 stages or Gleason score ≥ 8 or PSA > 20 ng/ml.

1.2 Therapeutic options

Different therapeutic options for localised prostate cancer exist. Depending on the age of the patient, his life expectancy and the aggressiveness of the cancer (determined as explained in the previous section), the most appropriate treatment or combination of them is chosen considering the therapeutic objective. This may include suppressing the tumour or metastases, reducing the risk of recurrence or slowing the tumour progression [47].

The main therapeutic options in the context of prostate cancer, according to their frequency of prescription, are:

— **Radical prostatectomy** (RP): it is a surgical treatment consisting in the total removal of the prostate gland and the seminal vesicles. It may be accompanied by lymph node dissection. It is one of the standard treatments for localised prostate cancers with low and intermediate risk. It can also be proposed in certain cases of localised high-risk, locally advanced cancers with lymph node involvement. Radiation and/or hormonal therapy may be prescribed as supplement. The most common side effects of radical prostatectomy are urinary incontinence, related to impaired functioning of the bladder and sphincter muscles, and erectile dysfunction. This treatment also implies a definite impossibility to ejaculate.
— **Radiotherapy**: it consists in irradiating cancer cells in order to prevent them from multiplying. Radiation doses can be administrated in two ways:
  — External: The source of radiation is located outside the body. It is delivered in the form of photons (X-rays from linear accelerator machines), electrons or, more rarely, other particles such as protons. It is one of the reference treatments for localised cancers with low and intermediate risk. Coupled with hormonal therapy, it is the recommended therapeutic option for localised high-risk cancers. It can also complement radical prostatectomy to reduce the risk of recurrence. Irradiation of healthy tissues adjacent to the prostate can cause a variety of side effects, including difficult or painful urination, diarrhea, fatigue, rectal bleeding or sexual dysfunction.
  — Brachytherapy: The source of radiation is located inside the body. Radioactive seeds are implanted within the prostate gland. These sources emit radiation that destroys the surrounding malignant cells. Since the gradient of dose drops sharply away from the radioactive seeds, brachytherapy is indicated for low-risk localised cancers. The most frequent side effects include difficult or painful urination, fatigue, rectal irritation or sexual dysfunction.
— **Hormonal therapy**, also called androgen deprivation therapy (ADT): it aims to reduce the levels

of the male hormones (mainly, testosterone and dihydrotestosterone) that stimulate prostate cancer cells to divide. Lowering androgen levels or preventing them from getting into prostate cancer cells often makes prostate cancers shrink or delay their growth. However, hormonal therapy alone is not curative. Combined with radiation therapy, it is the gold standard for high-risk localised prostate tumours. It is also used in case of metastatic cancers. The most common side effects of hormonal therapy are hot flushes, erectile dysfunction, changes in physical appearance and osteoporosis.

- **Deferred therapy**: in some cases, treatment of localised prostate cancer may be deferred or even avoided to prevent toxicity. There are two distinct strategies for conservative management that aim to reduce overtreatment:
  - Active surveillance: the surveillance of cancer evolution is carried out through frequent DRE, blood tests to measure the PSA levels, biopsies and magnetic resonance imaging (MRI) scans. It is prescribed to patients with clinically confined, very-low-risk tumours.
  - Watchful waiting: it involves fewer tests than active surveillance, so the side effects of repeated tests or biopsies are also avoided. It is recommended when cancer progresses slowly or for older men with a high incidence of comorbidities and other causes of mortality.
- **High-intensity focused ultrasound** (HIFU): it consists in delivering focused ultrasound waves to a focal point in order to kill tumour cells through heating and cavitation. This technique is advised for patients aged over 70 years with low-risk tumours. It is mostly used in the case of local recurrence following radiotherapy.

This thesis focus on external beam radiotherapy (EBRT) for the treatment of prostate cancer. This therapeutic option is detailed in the following section.

1.2.1 External beam radiation therapy

More than two thirds of the patients diagnosed with localised prostate cancer are treated with EBRT [30], often combined with a concomitant treatment (e.g., surgery or hormonal therapy). During EBRT, ionising rays charged with high energy photons are delivered to the tumour, aiming to maximise local control while sparing neighbouring organs (mainly the rectum and the bladder). In order to allow healthy tissues to recover, the radiation dose is fractionated and delivered over several weeks from Monday to Friday.

Prior to the beginning of treatment, the radiotherapy team plans the optimal radiation scheme, in terms of total dose, fractionation and angles of the beams. This process starts by acquiring a computed tomography (CT) scan of the the pelvic region. The different structures observed on the CT scan (prostate, seminal vesicles, bladder and rectum) are then delineated by an expert. This information is imported to a treatment planning system (TPS) to generate the irradiation scheme. A 3D map relating every point of the CT with a prescribed level of dose is obtained. During the treatment, the patient is placed on a table below the linear particle accelerator delivering the ionising rays (Fig. 1.2).

Over the last decades, improvements in imaging and computing have led to a number of technical advances (Fig. 1.3). They have allowed more precise and conformal delivery of doses of radiation to the prostate, thereby improving the therapeutic ratio.

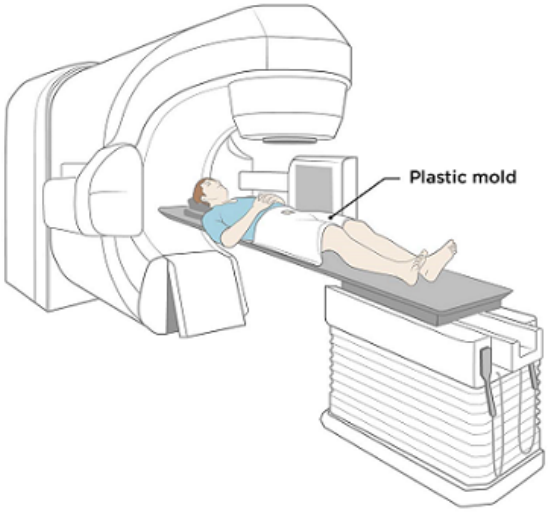

Figure 1.2 – Patient positioned during the irradiation session (source: www.mskcc.org)

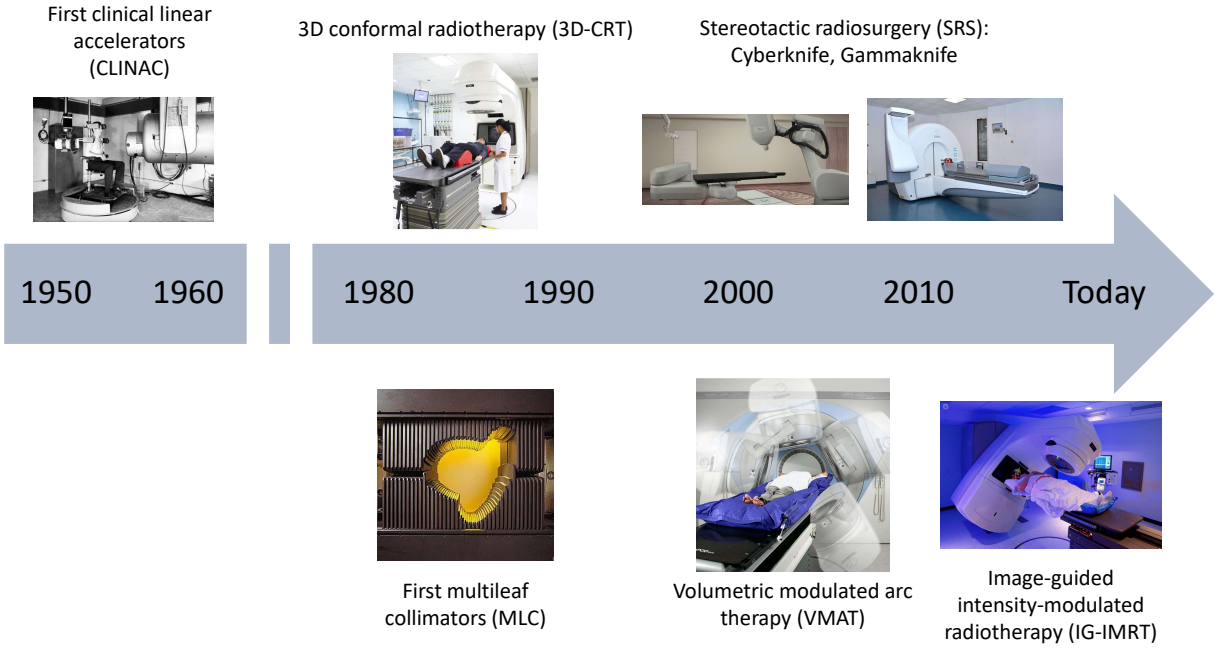

Figure 1.3 – Evolution of EBRT

Image-guided intensity-modulated radiotherapy

At the present time, image-guided intensity-modulated radiotherapy (IG-IMRT) is considered the gold standard for EBRT. It has replaced 3D conformal radiotherapy (3D-CRT) thanks to its high conformity, which facilitates dose escalation and improves local control without significantly increasing the risk of

toxicity [48, 49]. A comparison of treatment plannings using 3D-CRT and IG-IMRT is shown in Fig. 1.4.

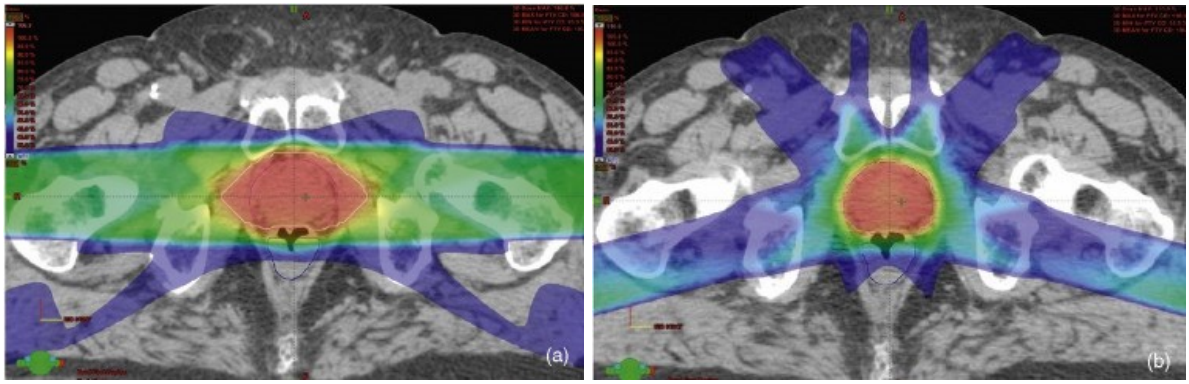

(a) (b)

Figure 1.4 – Dose distribution of a prostate cancer patient using (a) 3D-CRT and (b) IG-IMRT [50]. Lowest dose dose is represented in blue and highest dose, in red.

In the case of intensity-modulated radiotherapy, the fluence (amount of photons per surface unit) is not homogeneous but adjusted with a multileaf collimator by continuously adapting the beams to the shape of the target volume [51]. This allows to deliver more conformal dose distributions, fitting complex structures.

The benefits of intensity-modulated radiotherapy can only be realised if the target and healthy tissues are given exactly the radiation dose prescribed in the treatment plan. Geometric differences between the two distributions can compromise tumor control or increase the risk of complications.

Different anatomical references, such as skins markers, can be used to reproduce the patient positioning in the irradiation field throughout the different irradiation sessions. However, since the patient may experience anatomical changes, such as weight loss, the effectiveness of these markers is limited and may lead to setup errors [52].

Portal imaging systems were developed with the introduction of linear accelerators [53]. Using a digitally-reconstructed radiograph based on the planning CT, the patient bone structures could be aligned throughout the irradiation sessions. However, repositioning the patient according to the bone structures did not completely solve the problem of geometric uncertainties. Indeed, between two irradiation fractions or even during a session, anatomical variations (displacements or deformations of the tumour or the healthy tissues) can occur in a fixed bone reference system.

This need to precisely locate the target and the organs at risk has led to the development of imaging devices integrated in the linear accelerators and allowing the visualization of the soft tissues [54]. Cone beam computed tomography (CBCT) is the most frequently used imaging modality for this purpose. An X-ray source and a 2D detector are integrated in every modern linear accelerator. This system rotates around the patient and acquires a large number of 2D projections, allowing to reconstruct a 3D image that can be compared with the planning CT. In the recent years, alternative techniques using non-ionising radiation modalities, such as electromagnetic transponders (EMT) and 4D transperineal ultrasound (4D-TPUS), have been proposed [55].

Conventional fractionations

In the context of prostate cancer, an irradiation total dose between 74 and 80 Gy delivered at 2 Gy fractions has been typically prescribed [56–58]. The benefits of these schedules, in terms of tumour control and reduced toxicity, have been clearly shown in the past. However, it has been reported that about 0-10%, 10-20% and 30-40% of patients with respectively, low, intermediate and high-risk tumours (according to the D'Amico classification) suffer biochemical recurrence within the 5 years following the end of irradiation [2]. It is thus crucial to identify predictors of recurrence to adapt treatments for patients with the highest rates of biochemical failure. Furthermore, this conventional fractionation presents several issues concerning both patient access and convenience, as well as resource utilization during the 8 weeks of treatment.

Hypofractionated treatments

In recent years, moderate hypofractionated schedules (consisting in increasing the dose per fraction up to 3.4 Gy, thus reducing the number of irradiation sessions) have been proposed and tested in randomised clinical trials [3, 5–8]. Results suggest that hypofractionated radiotherapy is non-inferior to conventional fractionation in terms of freedom from biochemical or clinical failure and is not associated with increased toxicity. It may be thus recommended as a new standard for localised prostate cancer. Nevertheless, numerous uncertainties about the dose equivalences, in terms of both local tumour control and toxicity, still exist.

1.3 Models of tumour response: state of the art

1.3.1 Dose-effect approaches

First data-based approaches of modelling the tumour response to irradiation consisted in exploring the dose-effect relationship, which states that the higher the dose, the higher the tumour control probability (TCP) [9, 59–62]. These TCP curves are believed to have a sigmoid shape (Fig. 1.5). They may be fitted empirically performing a regression analysis [10, 11, 63] or derived from a model of tumour control using the linear-quadratic (LQM) formalism of cell survival [64–66].

Although TCP curves have been generated from population data for different risk groups [67, 68] and some TCP models have included inter-patient variations in terms of intrinsic radiosensitivity of tumour cells [66, 69, 70], this kind of approach has limited integration of inter-patient heterogeneity, which may be deduced from imaging parameters.

1.3.2 Radiomics approaches

The qualitative study of prostate MRI scans has typically played a crucial role at the pre-treatment staging step. In contrast, their quantitative analysis, in particular, the association of MRI features with biochemical recurrence, has not been fully explored in clinical practice yet. The only MRI-derived parameters whose impact on survival has been clearly established are T-stage, tumour volume, extracapsular extension, seminal vesicle invasion and volume of malignant spectroscopic MRI metabolism [71–74].

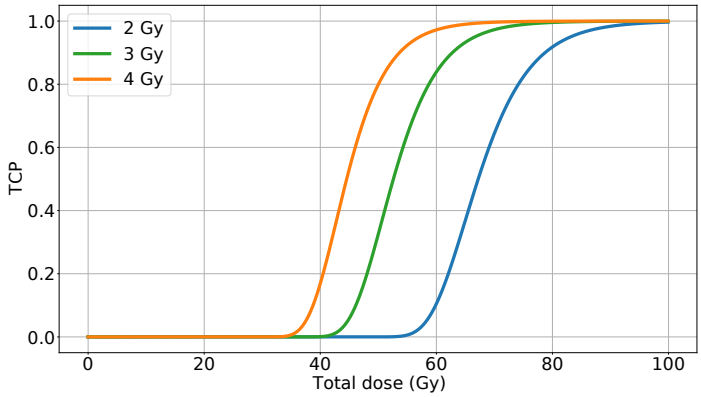

Figure 1.5 – Example of TCP curves for different frationations

Other imaging parameters such as the Haralick textural features [75], characterizing the spatial variations of signal intensity in an image, may also provide useful information about underlying pathophysiological processes. Radiomics approaches [76, 77], based on these imaging biomarkers, have emerged over the last few years as appealing tools to discriminate prostate tumour from healthy tissue [78], to assess the Gleason score [79, 80] or to predict tumour recurrence and survival in the context of prostate cancer EBRT [12, 13].

Nevertheless, the performance of these radiomics approaches is still limited in terms of prediction scores (e. g. AUC, C-index). Furthermore, they require a large amount of population data in order to be statistically significant and they are usually based on complex machine learning methods, which raises the question of interpretability.

In addition, radiomics-based studies are frequently confronted with the class imbalanced problem, i.e. nearly every individual of the cohort belongs to the majority class and only a few of them constitute the complimentary minority class. This phenomenon is particularly evident in the context of the present work, as the vast majority of the prostate cancer patients treated with EBRT do not experience biochemical recurrence. It must be noted that training a classifier on such highly imbalanced data can be misleading, since the minority class has a minimal effect on overall accuracy. To cope with this issue, several methods consisting in artificially oversampling the minority class (such as SMOTE, Borderline SMOTE, SMOTE+ENN and ADASYN) have been proposed [81]. In depth, the SMOTE technique produces new minority observations based on weighted average of the k-nearest neighbours of the same class. However, these artificial minority class examples may be produced too deeply into the majority class space. Inducing a classifier under such a situation can lead to overfitting. To deal with this issue, the Wilson Edited Nearest Neighbour Rule (ENN) [82] can be used to remove noisy SMOTE examples while leaving the original data unchanged.

1.3.3 Mechanistic modelling approaches

As opposed to the data-driven techniques described in the previous sections, mechanistic modelling appears as a groundbreaking approach based on the integration of the different biological processes underlying the behavior of a given clinical endpoint. Numerous radiobiological mechanisms have been considered to participate in tumour survival after radiotherapy and later recurrence. In particular, those related to the 5 R's (reoxygenation, repopulation, DNA repair, radiosensitivity and redistribution in the cell cycle) have been thoroughly studied [17]. Modulation of tumour radiation resistance is thought to be related, at least, to hypoxia and abnormal angiogenesis resulting in the reoxygenation of the tissue [18–20], a high rate of proliferation/repopulation of tumour cells [21–23] and a low intrinsic radiosensitivity of tumour cells [24–26], associated with a preponderant cell cycle distribution (Fig. 1.6) in the radioresistant phase of synthesis (S) [27]. Mitotic catastrophe [28], considered to be the main type of cell death after irradiation, and cycle arrest of irradiated cells at checkpoints between phases G1/S and G2/M may also play a major role in tumour control [29, 30].

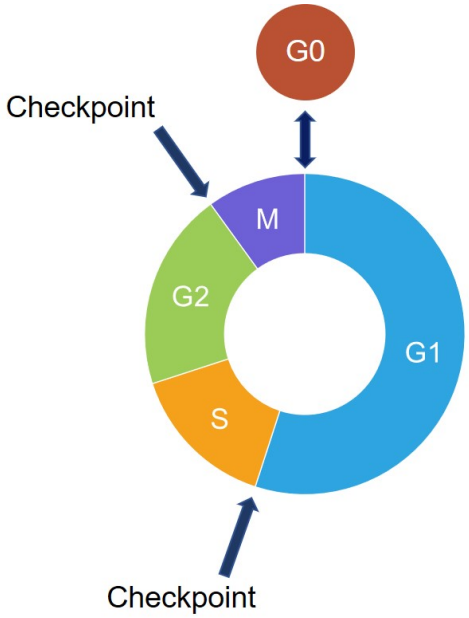

Figure 1.6 – Cell cycle composed of phases Gap 1 (G1), in blue; synthesis (S), in orange; Gap 2 (G2), in green; mitosis (M), in purple, and a quiescent phase Gap 0 (G0), in red. Two checkpoints where irradiated cells may be arrested exist between phases G1/S and G2/M.

Mechanistic *in silico* modelling [83, 84] emerges as a powerful tool to integrate all these radiobiological mechanisms and predict their behaviour on hypothetical scenarios. These computational models make it possible to create, at a limited cost, infinite virtual tumours with different vascular architectures on which various irradiation schedules can be simulated. A panoply of mechanistic *in silico* models of tumour response to radiotherapy exist in the literature. For the vast majority of them, the response to irradiation is based upon the widely-used LQ formalism [41–43]. According to their spatial scale, mechanistic models can be classified into 3 categories: microscopic, macroscopic and hybrid or multiscale.

Microscopic models [31, 39, 85] consider the stochastic behaviour of individual cells and the interactions between them. They can reflect cell heterogeneity but may not reproduce a realistic tumour microenvironment and the link to the image is not clear. Borkenstein *et al.* [85] developed a single-cell-based computational model that integrated tumour proliferation governed by the cell cycle, oxygenation and radiation response. It also included angiogenesis, considering the diffusion of tumour angiogenesis factors (TAF) emitted by hypoxic cells. Harting *et al.* [39] went further from Borkenstein *et al.* and proposed a more detailed description of the oxygen supply and angiogenesis. Paul-Gilloteaux *et al.* [31] developed a 2D and 3D cellular automaton that was validated on human prostate tumours transplanted in mice and then used to generate TCP curves for different radiotherapy protocols. It introduced mitotic catastrophe instead of instantaneous apoptosis as the main type of cell death after irradiation.

Macroscopic models [16, 86–89], in contrast, describe spatiotemporal changes in tumour cell density using differential equations at the tissue scale, which makes them susceptible to be validated with clinical data. However, they have limited integration of cell heterogeneity. Powathil *et al.* [86] and Rockne *et al.* [88] each developed an *in silico* model which included proliferation of tumour cells and their response to irradiation. Kohandel *et al.* [87] proposed another computational model that incorporated hypoxia and angiogenesis. Belfatto *et al.* [89] developed an *in silico* model based on Gompertzian growth and fitted with uterine cervical cancer CBCT scans. It included oxygenation and a response to irradiation that considered both its instantaneous effect and its delayed cell killing capability, which may be associated with mitotic catastrophe.

Hybrid or multiscale models arise to combine the advantages of the 2 previous approaches in a single framework. Numerous multiscale *in silico* models of tumour response to radiotherapy already exist in the literature. Titz *et al.* [33] developed a model of tumour growth and response to radiation that incorporated the cell cycle distribution. This allowed to consider phase-dependent radiosensitivity. Espinoza *et al.* [32] proposed a voxel-based multiscale model to simulate the radiation response of hypoxic tumours. Pre-calculated oxygen histograms for each voxel were used to simulate hypoxic-induced angiogenesis and oxygen-dependent response to irradiation. Apeke *et al.* [34] developed another *in silico* model considering cell cycle distribution at a mesoscopic scale. Realistic static oxygenation maps were obtained from FDG PET images.

Overall, a large number of *in silico* mechanistic models combining some of the most important biological processes characterizing cancer and the response to radiotherapy have already been proposed in the literature (Table 1.1). However, some of these mechanisms, which may play a major role in tumour control, have never been included in a single comprehensive model. In particular, no work of the literature has simultaneously integrated, to our knowledge, dynamic oxygenation, mitotic catastrophe and cell cycle distribution allowing the simulation of a phase-dependent radiosensitivity for tumour cells.

Several issues are intrinsic to multiscale modelling. Firstly, multiscale models integrate complex radiobiological mechanisms occurring at different spatial and temporal scales (from cell to tissue and from milliseconds to months, respectively). This constitutes a serious challenge from a mathematical and computational point of view. Simulations must have adapted time-steps and spatial resolutions in order to capture changes while limiting redundant iterations. They must be synchronised at a reasonable frequency to be able to reflect the numerous interactions existing among them. Computational libraries like M2SL (Multi-formalism Modeling and Simulation Library) [44] have been developed to facilitate the integration

Table 1.1 – Mechanistic *in silico* models of tumour response from the literature

Model	Spatial scale	Site	Oxygenation	Division of tumour cells	Angiogenesis	Division of healthy cells	Response to irradiation
Borkenstein *et al.* [85]	Micro.	-	Step function of O_2 based on distance to endothelial cell	Cell cycle	Step function of TAF based on distance to hypoxic cell and proliferation threshold	Resorption factor	- LQM - O_2 dependent - Mitotic death
Harting *et al.* [39]	Micro.	-	O_2 profile based on distance to endothelial cell	Cell cycle	TAF profile based on distance to hypoxic cell and proliferation threshold	Proliferation factor	- LQM - O_2 dependent - Instantaneous death
Paul-Gilloteaux *et al.* [31]	Micro.	Prostate	Static O_2 profile based on distance to endothelial cell	Cell cycle	-	-	- LQM - O_2 dependent - Mitotic death - Cycle arrest - Increased permeability of endothelial cells
Powathil *et al.* [86]	Macro.	Brain	-	Reaction-diffusion equation	-	-	- LQM - Delayed death
Kohandel *et al.* [87]	Macro.	-	Reaction-diffusion equation	Reaction-diffusion equation	Reaction-diffusion equation	-	- Differential equation - O_2 dependent - Delayed death
Rockne *et al.* [88]	Macro.	Brain	-	Reaction-diffusion equation	-	-	- LQM - Instantaneous death
Belfatto *et al.* [89, 90]	Macro.	Cervix	Differential equation	Differential equation	-	Resorption differential equation	- LQM - O_2 dependent - Delayed death
Espinoza *et al.* [32, 91]	Hybrid	Head and neck	Precalculated O_2 histogram based on reaction-diffusion equation	Proliferation factor	Proliferation factor of endothelial cells	Resorption factor	- LQM - O_2 dependent - Instantaneous death
Apeke *et al.* [34]	Hybrid	Rectum	Static O_2 map	Cell cycle	-	-	- LQM - O_2 dependent - Instantaneous death
Titz *et al.* [33, 92]	Hybrid	Head and neck	Static O_2 map	Cell cycle	Proliferation factor of endothelial cells proportional to O_2 levels	-	- LQM - O_2 dependent - Delayed death

of different multiscale processes in the modelling task.

Secondly, hybrid models may contain a large number of parameters. Due to ethical or technical reasons, some of them are complicated to measure *in vivo* or even *in vitro*, which hampers model calibration and validation.

1.4 Sensitivity analysis

As stated in the previous section, mechanistic models may integrate a large number of parameters. In the context of cancer and response to radiotherapy, some of them are difficult to measure *in vivo* or even *in vitro*, which complicates model calibration and validation. Although the independent contribution of different radiobiological mechanisms has been evaluated for some models through TCP or tumour density curves [31, 32, 39], a thorough study to precisely identify the impact of each parameter has not been performed yet, to our knowledge, for any of the mechanistic models of the literature.

Sensitivity analysis can be used to study the impact of all the parameters of a model on a given output, identify the most relevant ones and determine which ones could be negligible [93, 94]. Multiple examples of sensitivity analysis allowing subsequent parameter identification and model dimension reduction can be found in the biomedical literature [36–38].

Sensitivity analysis can be defined as the measurement of the effect that variations in the parameters $\boldsymbol{x} = [x_1, x_2, ...x_k, ...x_{K-1}, x_K]$ of a model $f(\boldsymbol{x})$ cause on its outputs $\boldsymbol{y} = [y_1, y_2, ...y_l, ...y_{L-1}, y_L]$.

Thus, they allow to determine which parameters of a model have the highest impact on a given output, so that subsequent estimation or observation focus on these most important factors. Morevover, they help identify which parameters of a model have little effect and can be thus replaced with a simpler definition.

Sensitivity analysis methods consist of the following four steps:

— Definition of parameter ranges: intervals of possible values for every parameter x_k of the model are defined from the literature or empirical observation.

— Generation of value sets within the parameter ranges: it can be performed following a simple plan (e. g., taking minimum, mean and maximum value combinations from the previously defined intervals) or using more complex techniques

— Computation of model outputs: the model is evaluated for each set of parameter values

— Computation of sensitivity indices: multiple sensitivity indices allow to quantify or qualify the impact of parameters on a given output

Existing sensitivity analysis methods can be divided into three groups: local, global and screening methods.

1.4.1 Local sensitivity analysis

Local methods are the most simple form of sensitivity analysis. They allow to asses the impact of variations of parameters in a small region of their space. A common approach consist in selecting a working point $\boldsymbol{x}^{(0)} = [x_1^{(0)}, x_2^{(0)}, ...x_k^{(0)}, ...x_{K-1}^{(0)}, x_K^{(0)}]$ and evaluating the model at $\boldsymbol{x}^{(0)}$ and $\boldsymbol{x}^{(i)} = [x_1^{(0)}, x_2^{(0)}, ...x_k^{(0)} + \delta, ...x_{K-1}^{(0)}, x_K^{(0)}]$, where δ is a certain perturbation of parameter x_k and $i = 1, ..., N$, with N, the number of variations. From $\boldsymbol{y}^{(0)} = f(\boldsymbol{x}^{(0)})$ and $\boldsymbol{y}^{(i)} = f(\boldsymbol{x}^{(i)})$, the partial derivatives $\frac{\partial \boldsymbol{y}}{\partial x_k}$ can be estimated,

normalised and compared.

Local sensitivity analysis may be useful given their simplicity and their reduced number of evaluations of the model. However, the parameter space is not fully explored, as they do not consider simultaneous variations of factors. Consequently, these one-at-a-time (OAT) approaches cannot detect interactions between parameters. Furthermore, they do not allow to identify non-linear effects.

1.4.2 Global sensitivity analysis

As opposed to local approaches, global sensitivity analysis explore variations of parameters in a large region of interest. The most popular family are variance-based methods. They allow to quantify which part of the variability of $\boldsymbol{y}$ can be attributed to the variability of the parameter x_k by means of different measures, such as the first order or main effect, $SI(x_k)$, and the total effect, $TSI(x_k)$, indices proposed by Sobol [95]. $SI(x_k)$ (1.1) quantifies the amount of variability on the outputs caused only by parameter x_k. $TSI(x_k)$ (1.2) measures the main effect of x_k as well as the impact of its interactions with other parameters.

$$SI(x_k) = \frac{\sigma^2\left[E(\boldsymbol{y}|x_k)\right]}{\sigma^2(\boldsymbol{y})} \tag{1.1}$$

$$TSI(x_k) = \frac{E\left[\sigma^2(\boldsymbol{y}|x_j, j \neq k)\right]}{\sigma^2(\boldsymbol{y})}. \tag{1.2}$$

The values of both indices belong to $[0, 1]$ and, by definition, $SI(x_k) \leq TSI(x_k)$.

$SI(x_k)$ and $TSI(x_k)$ are highly descriptive. However, they are computationally expensive to calculate as a great number of evaluations of the model are required.

1.4.3 Screening methods

In contrast to global sensitivity approaches, screening methods do not quantify the sensitivity of the different uncertain factors. Instead, they provide a qualitative view of the hierarchy of the parameters of a model with a reduced computational cost. For this reason, they can be used prior to any global sensitivity analysis or extensive parameter estimation process.

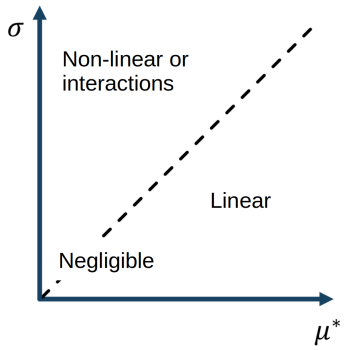

Figure 1.7 – μ^* vs. σ plane where the three regions of negligible effect, linear effect and non-linear effect or interactions can be identified

The most common screening technique is the Morris elementary effects method [96]. A full description of this approach can be found in section 4.2.3. In brief, the Morris method consists in calculating the mean μ^* and the standard deviation σ of the absolute values [97] of the elementary effects of the parameters of a model. Factors with low μ^* and σ can be considered negligible, those with high μ^* and low σ exert a linear effect on the model output and those with high μ^* and σ have either a non-linear effect or an important interaction with other factors.

The Morris method can thus rapidly identify linear relations between the parameters and the outputs of a model. However, it cannot distinguish between non-linear relations and parameter interactions.

Chapter 2

Motivations and objectives

In this chapter, the motivations and objectives of this work are described. In addition, an overview of the structure of this thesis is presented.

2.1 Motivations

As explained in the previous chapter, it is crucial to identify predictors of recurrence for prostate cancer patients treated with EBRT, in order to adapt the irradiation schedule for individuals with a high risk of biochemical failure. Dose-effect models [9–11], based on TCP curves, have been used in the past to predict recurrence. However, they have limited integration of inter-patient heterogeneity. Radiomics approaches, based on image biomarkers, have emerged in recent years as appealing tools to predict tumour recurrence and survival [12–14]. However, they have shown, limited performance, they are usually based on complex machine learning methods, which complicates interpretability, and they need a large amount of population data.

Mechanistic modelling appears as an alternative approach based on the integration of the different biological mechanisms underlying the behaviour of biochemical recurrence. Through *in silico* simulation, it allows to better comprehend the response of cancer patients to a certain irradiation schedule and its results are easily explainable. A large number of *in silico* mechanistic models combining some of the most important biological processes characterizing cancer and the response to EBRT have already been proposed in the literature [31–34, 39, 85–88, 90].

In particular, the model of Espinoza *et al.* [32, 91] integrates a great number of the major radiobiological mechanisms. However, it has not been tested, to our knowledge, on histopathological specimens. Moreover, the values of the model parameters remain uncertain, as they can widely vary in the literature. In addition, although the impact of different radiotherapy strategies has been explored [35], its simulation endpoint representing a clinical tumour control after prostate conventional and hypofractionated irradiation schedules has not been clearly identified.

Furthermore, some of the radiobiological mechanisms which may play a major role in tumour control, such as mitotic catastrophe and cell cycle distribution allowing the simulation of a phase-dependent radiosensitivity for tumour cells were not included. This issue is applicable to other models of the literature. To our knowledge, no previous work has simultaneously integrated dynamic oxygenation, mitotic catastrophe and cell-cycle-phase-dependent response of tumour cells to irradiation in a single comprehensive model.

Moreover, although the independent contribution of different radiobiological mechanisms has been evaluated for some models through TCP or tumour density curves [31, 32, 39], a thorough study to precisely identify the impact of each parameter has not been performed yet, to our knowledge, for any of the mechanistic models of the literature.

2.2 Objectives

The objectives of this work were therefore

1. to adapt the model of Espinoza *et al.* so that it can be initialised with prostate histopathological specimens
2. to simulate conventional and hypofractionated prostate irradiation schedules using the adaptation of the model of Espinoza *et al.*

3. to develop an original *in silico* model of tumour growth and response to irradiation, integrating the main radiobiological mechanisms of the literature in the context of prostate cancer
4. to perform an exhaustive sensitivity analysis of this original comprehensive model
5. to propose a simplified model based on the results of the sensitivity analysis and equivalent in terms of TCP, tumour cell density and prediction of biochemical recurrence
6. to predict biochemical recurrence after radiotherapy using simulation outputs obtained with the reduced model and to compare the results with those of a classical radiomics approach
7. to test personalised alternative irradiation schedules using the reduced model.

An overview of the thesis structure is depicted in Fig. 2.1.

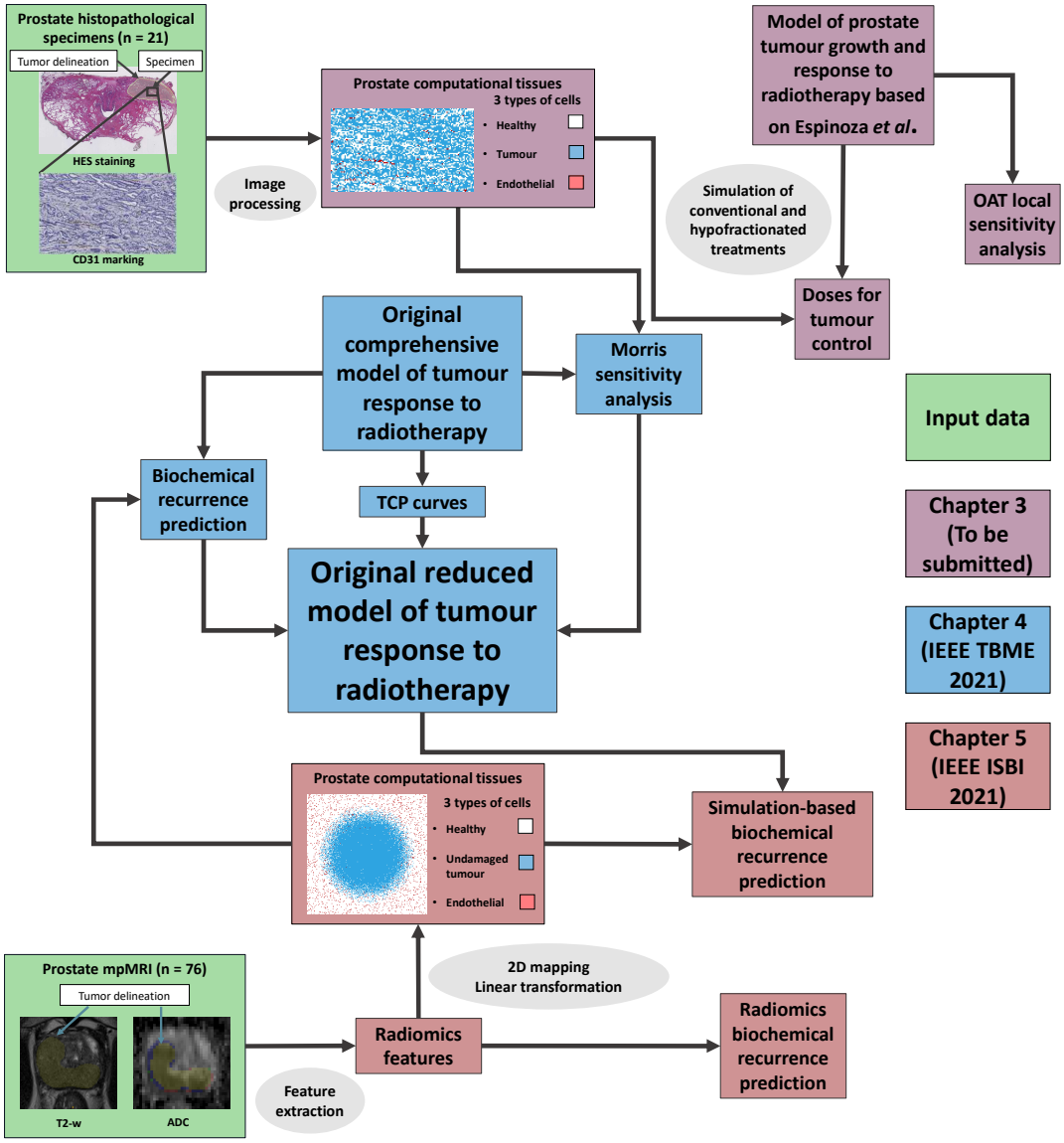

Figure 2.1 – Overview of the thesis structure. In chapter 3, from prostate histopathological specimens, computational tissues are built and used to initialise simulations of conventional and hypofractionated treatments using a model of tumour growth and response to EBRT based on Espinoza *et al.* A local sensitivity analysis of this model is performed. In chapter 4, an original comprehensive model of tumour response to radiotherapy is developed. A Morris sensitivity analysis using the histology-based computational tissues is performed. Based on its results, a reduced version equivalent in terms of TCP and biochemical recurrence prediction is obtained. In chapter 5, from prostate pre-treatment mpMRI, radiomics features are extracted. Firstly, they are employed to predict biochemical recurrence following a classical radiomics approach. Secondly, they are used to build analogous computational tissues on which the prescribed treatments are simulated with the reduced model of tumour response to radiotherapy. Biochemical recurrence is then predicted using the simulation outputs.

Part II

Adapting an existing *in silico* model of tumour response

Chapter 3

Adapting an existing in silico model of tumour response to simulate hypofractionated treatments in the context of prostate cancer

---

In this chapter, an existing computational model of tumour response to radiotherapy is adapted so that it can be initialised with prostate histopathological specimens. It is implemented in the programmable modelling environment Netlogo. A local sensitivity analysis is performed to determine the impact of each parameter of the model on tumour cell death. The different radiobiological mechanisms implemented in the model are compared with prostate clinical data from the literature. The response to various irradiation protocols (conventional and hypofractionated) considering 6 different published values of α and β, are simulated. Total doses to achieve tumour control close to clinical values are identified.

The content of this chapter will be submitted for publication.

C. Sosa-Marrero, V. Aubert, N. Rioux-Leclercq, R. Mathieu, A. Fautrel, F. Paris, O. Acosta and R. de Crevoisier. «Simulation of moderate hypofractionated irradiation schedules on prostate histopathological specimens». (To be submitted)

3.1 Introduction

As previously explained, prostate cancer can be treated with EBRT at a standard fractionation of 2Gy/fraction, with a total dose ranging from 74 Gy to 80 Gy. Moderate hypofractionation protocols (up to 3.4 Gy/fraction) have been tested [3–8] and recently considered as a full option to irradiate localised prostate cancer [56]. However, the critical issue of finding the optimal total dose in terms of maximum tumour control and reduced toxicity remains.

The tumour response to irradiation may appear highly complex due to the wide range of parameters and mechanisms impacting on tumour cell survival, such as the oxygenation of the tissue [18–20], the proliferation of tumour cells [21, 23], the intrinsic radiosensitivity, given by the parameter α of the LQM [41], and the response to fractionation, that can be expressed with the ratio α/β. Computational modelling emerges as an appealing tool to include all these mechanisms and parameters [31–34, 90].

The model of Espinoza *et al.* [32] integrates most of the major radiobiological mechanisms of the literature, namely (i) oxygenation, (ii) proliferation of tumour cells, (iii) hypoxia-induced angiogenesis, (iv) oxygen-dependent cell survival after irradiation and (v) resorption of dead cells. In addition, it proposes a multiscale approach in which each voxel contains a fraction of tumour, capillary, normal and dead cells. This allows, at the same time, to consider heterogeneity at the microscopic level and to integrate clinical data at the macroscopic scale. Nevertheless, the model of Espinoza *et al.* has not been tested, to our knowledge, on histopathological specimens. Moreover, the values of the model parameters (in particular, α and β) remain uncertain, as they can widely vary in the literature [98–102]. Finally, although the impact of different radiotherapy strategies has been explored [35], its simulation endpoint representing a clinical tumour control has not been clearly identified in the context of prostate cancer.

The main purpose of this work was therefore to use the model of Espinoza *et al.* on histopathological specimens to simulate the response of prostate tumours to conventional and moderate hypofractionated radiotherapy and to compare the results with clinical data from the literature. The secondary objectives were to perform a local sensitivity analysis assessing the impact of the model parameters on tumour response and to compare the outcome of the model with published prostate *in vivo* pO_2 data.

3.2 Material and methods

3.2.1 Workflow of the study

The workflow of the study is depicted Fig. 3.1 and can be divided in 3 steps:

1. Generation of a computational model of tumour growth and response to radiotherapy based on the works of Espinoza *et al* [32]. and using prostate histopathological specimens
2. Local sensitivity analysis assessing the impact of every parameter of the *in silico* model on tumour cell survival
3. Comparison of the model with prostate clinical data from the literature, in terms of both pO_2 and recurrence after conventional and moderate hypofractionated schedules

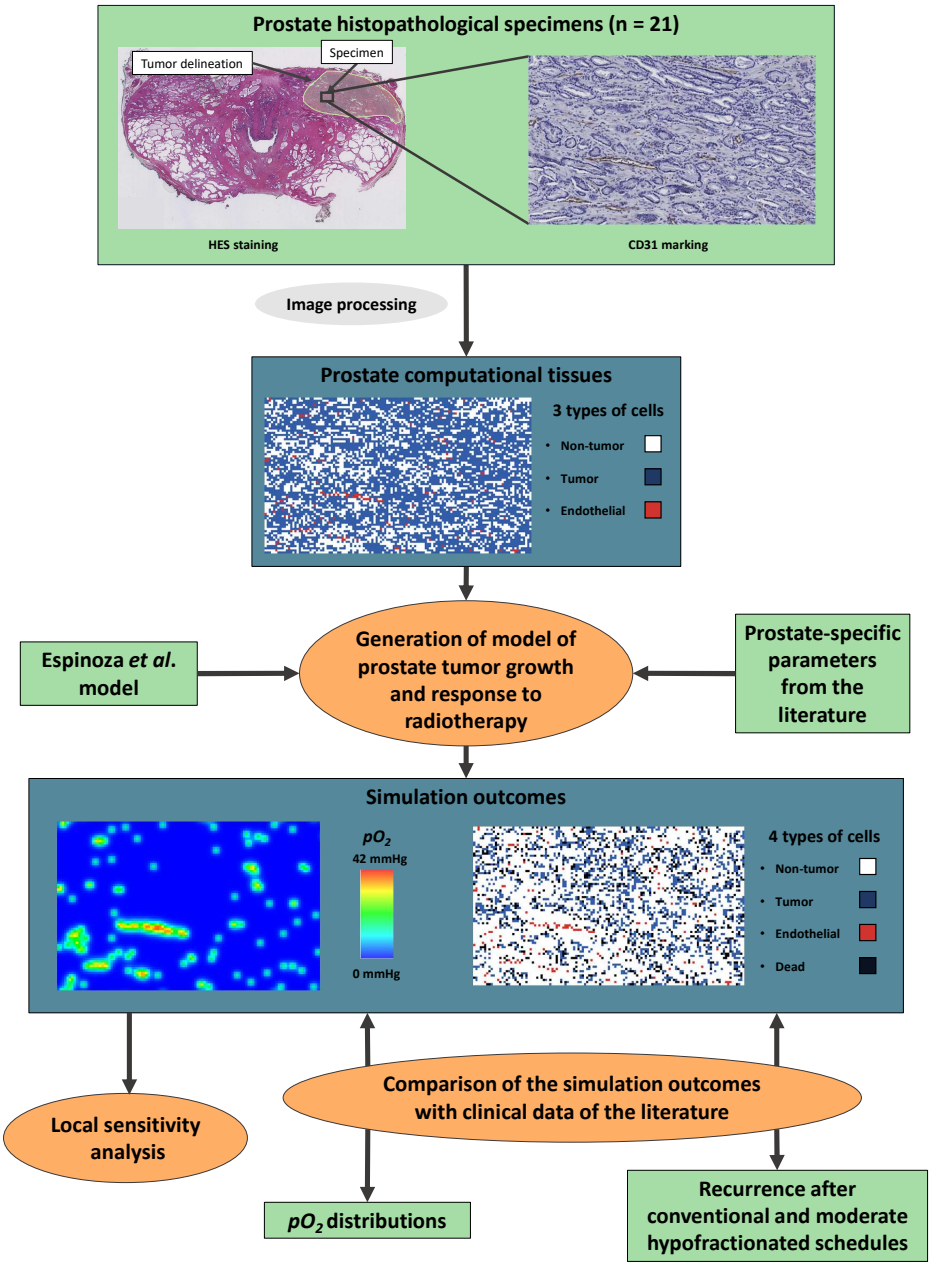

Figure 3.1 – Workflow of the study. It can be divided in 3 steps (in orange): generation of a model of prostate tumour growth and response to radiotherapy based on histopathological specimens, the works of Espinoza *et al.* and prostate-specific parameter values from the literature; local sensitivity analysis assessing the impact of the model parameters on tumour cell survival and comparison of the simulation outcomes with prostate clinical data of the literature (pO_2 distributions and recurrence after conventional and moderate hypofractionated schedules).

3.2.2 Histopathological delineation, image processing and generation of computational tissues

Histopathological specimens were used to create realistic computational prostate tissues. They were extracted from 7 patients with localised prostate cancer treated with radical prostatectomy. Each sample was then sliced by an expert pathologist according to the Stanford protocol. The resulting histology blocks were embedded in paraffin. Slices were obtained every 0.5 mm using a microtome and a hematoxylin-eosin-saffron (HES) staining was performed. All the slices were then digitised. A senior uropathologist manually delineated all tumour foci on the HES axial images and assigned Gleason scores to each focus. Blood vessels were marked by CD31 antibodies. Three slices with tumour foci were then selected per patient (a total of 21 analysed slices). The surface of each slice was approximately 2000 μm $\times$ 1200 μm. The Gleason score distribution was the following: Gleason 7 (3+4) (n=8, 38%), Gleason 7 (4+3) (n=5, 24%) and Gleason 8 (n=8, 38%). Images were processed with CellProfiler, a free, open-source software for quantitative analysis of biological images [103]. A semi-automatic method to extract the position of endothelial cells and tumour foci was used. The distribution of endothelial cells was extracted from the CD31 marking, using a threshold on the hue component of the images. The number and position of tumour cells were extracted from the manual delineation of the uropathologist combined with a threshold on the blue component of the CD31 images (a high blue value indicating a high density of tumour cells). The remaining cells extracted from every slice (lymphocytes, fibroblasts, non-tumour glandular cells...) were considered to form a third category of non-tumour cells. This information was then used to create 21 virtual tissues for our computational model developed on the Netlogo software [40], a free multi-agent programmable modelling environment. Each pixel of the 2D virtual tissues corresponded to a tumour, non-tumour or endothelial cell (approximately 20 μm $\times$ 20 μm).

3.2.3 Description of the model of tumour response to radiotherapy

The model developed in this work was based on the approach proposed by Espinoza *et al.* [32, 91]. We adapted their model so that it could be apply to prostate histopathological specimens as support for simulations. Our version integrated the following radiobiological mechanisms: (i) oxygenation, (ii) proliferation of tumour cells, (iii) oxygen-dependent response to irradiation and (iv) resorption of dead cells.

Oxygenation

The distribution of oxygen in the model was based on a reaction-diffusion equation (3.1)

$$\frac{\partial u(\boldsymbol{x},t)}{\partial t} = D\Delta u(\boldsymbol{x},t) - r(u(\boldsymbol{x},t)), \tag{3.1}$$

where $u(\boldsymbol{x},t)$ is the oxygen concentration; D, the diffusion coefficient and, $r(u(\boldsymbol{x},t))$, the oxygen consumption modeled by a Michaelis-Menten equation (3.2)

$$r(u(\boldsymbol{x},t)) = V_{max}\frac{u(\boldsymbol{x},t)}{u(\boldsymbol{x},t)+K_M}, \tag{3.2}$$

with V_{max}, the maximum oxygen consumption rate and K_M, the Michaelis constant. The diffusion was considered isotropic and homogeneous. The correspondence between the oxygen concentration and the partial pressure of oxygen, $pO_2(\boldsymbol{x}, t)$, could be established using the Henry's law (3.3)

$$pO_2(\boldsymbol{x}, t) = K_H u(\boldsymbol{x}, t), \tag{3.3}$$

where K_H is the Henry's constant. The pO_2 of endothelial cells was fixed at a constant pO_2^{cap} .

Proliferation of tumour cells

The proliferation of tumour cells was considered by multiplying, at every iteration of the simulation, the number of tumour cells by a proliferation factor PF, given by (3.4)

$$PF = 2^{\frac{\Delta t}{t_p}}, \tag{3.4}$$

where t_p is the tumour cell proliferation time and Δt, the simulation timestep. New tumour cells were randomly placed adjacent to the existing ones, replacing non-tumour cells.

Oxygen-dependent response to irradiation

We considered only the response to irradiation of tumour cells. Endothelial and non-tumour cells were supposed completely radioresistant. The survival fraction SF of tumour cells after irradiation was calculated using the LQM, including the OER as a factor to modulate the SF according to the pO_2. The fate of each tumour cell was determined after every irradiation by (3.5)

$$SF = \exp\left(-\frac{\alpha}{m}\, d\, OER(pO_2) - \frac{\beta}{m^2}\, d^2\, OER^2(pO_2)\right), \tag{3.5}$$

where α and β are the intrinsic radiosensitivity parameters of the LQM in normoxic conditions; m, the maximum value of OER, and d, the dose per fraction. The OER is given by (3.6)

$$OER(pO_2) = \frac{m\, pO_2 + k}{pO_2 + k}, \tag{3.6}$$

where, k is the oxygen partial tension such that $OER = (m+1)/2$. After every irradiation, the SF of every tumour cell was computed. Next, it was compared with a random number $n \in]0, 1]$. If $n \leq SF$, then the tumour cell in question was considered to survive. Otherwise, it was supposed to be killed by irradiation.

Resorption of dead cells

Dead cells were resorbed after a certain time. The number of dead cells in the tissue was multiplied at every iteration of the simulation by $(1 - RF)$, where RF is the resorption fraction of dead cells calculated with (3.7)

$$RF = 1 - 2^{\frac{-\Delta t}{t_r}}, \tag{3.7}$$

where t_r is the dead cell resorption time. After resorption, new non-tumour cells randomly replaced dead cells.

3.2.4 Local sensitivity analysis

A local sensitivity analysis was performed to assess the effect of the 10 parameters of the model on tumour cell survival. The impact of the variation of a single parameter x_k at a time on the number of remaining tumour cells after irradiation, N_{tum}, was quantified by means of the relative sensitivity coefficient (RSC_k) (3.8)

$$RSC_k = \frac{RSC_k^{max} + RSC_k^{min}}{2}, \tag{3.8}$$

with RSC_k^{max} and RSC_k^{min} given by (3.9) and (3.10)

$$RSC_k^{max} = \frac{(N_{tum}(\boldsymbol{x_k^{max}}) - N_{tum}(\boldsymbol{x^{mean}}))\, x_k^{mean}}{(x_k^{max} - x_k^{mean}) N_{tum}(\boldsymbol{x^{mean}})}, \tag{3.9}$$

$$RSC_k^{min} = \frac{\left(N_{tum}(\boldsymbol{x^{mean}}) - N_{tum}(\boldsymbol{x_k^{min}})\right) x_k^{mean}}{(x_k^{mean} - x_k^{min}) N_{tum}(\boldsymbol{x^{mean}})}, \tag{3.10}$$

where x_k^{min}, x_k^{mean} and x_k^{max} correspond, respectively, to the minimal, mean and maximal values of the tested parameter x_k reported in the literature and N_{tum}, to the number of tumour cells after simulation considering $\boldsymbol{x_k^{min}} = [x_1^{mean}, ..., x_k^{min}, ..., x_{10}^{mean}]$, $\boldsymbol{x^{mean}} = [x_1^{mean}, ..., x_{10}^{mean}]$ or $\boldsymbol{x_k^{max}} = [x_1^{mean}, ..., x_k^{max}, ..., x_{10}^{mean}]$.

An RSC_k close to 0 indicates that a variation of the parameter x_k has a negligible impact on the number of tumour cells after irradiation. A positive RSC_k suggests that an increase of the parameter results in a greater value of the endpoint. In contrast, a negative RSC_k implies that augmenting x_k causes a decrease of the remaining number of tumour cells.

The analysis was carried out on a single virtual tissue containing 70% of tumour cells, randomly distributed. For every simulation, a sequence of 10 days of tumour growth followed by 5 fractions of 2 Gy each (total dose of 10 Gy), delivered every 24 hours was considered. Due to the stochastic component of the model, 5 repetitions were performed for each combination of parameters (corresponding to a total of 105 simulations). The values of the 10 parameters used in the sensitivity analysis are shown in Table 3.1.

3.2.5 Comparison of the simulation outputs with pO_2 *in vivo* data

In order to study the realism of our model, the outcome of our oxygenation mechanism was compared with the results of two experiments of the literature in which prostate *in vivo* pO_2 was measured using Eppendorf microelectrodes: Movsas *et al.* [119] (6040 measurements from 59 patients) and Parker *et al.* [120] (2500 measurements from 55 patients). We studied the mean pO_2 values reported in the *in vivo* studies and the one obtained after simulations on our 21 virtual tissues, and the corresponding distributions.

Table 3.1 – Model parameter values used for the local sensitivity analysis and the comparisons with clinical data. Stars indicate prostate cancer data.

	Local sensitivity analysis				**Comparisons with clinical data**	
Parameter (unit)	x^{min}	x^{mean}	x^{max}	**Sources**	**Chosen values**	**Sources**
d_{vasc} (%)	0.3	4.2	8	Our histopathological specimens*	Tissue dependent	Our histopathological specimens*
pO_2^{cap} (mmHg)	12	42	72	[104]	42	[104]
D (mm^2/s)	$1.46 \cdot 10^{-9}$	$1.835\ 10^{-9}$	$2.21\ 10^{-9}$	[105–107]	$1.8\ 10^{-9}$	[107]
V_{max} mmHg/s)	8.3	15.2	22.1	[108–110]*	15	[110]*
K_M (mmHg)	0.17	3.035	5.9	[111, 112]	3	[111, 112]
α (Gy^{-1})	0.02	0.13	0.26	[98, 113]*	0.032, 0.036, 0.041, 0.15 0.25, 0.26	[98–102]*
β (Gy^{-2})	0.0012	0.0506	0.1	[98, 114, 115]*	0.0229, 0.024, 0.026, 0.0293, 0.048, 0.06	[98–102]*
m	2.7	3	3.3	[116, 117]	3	[116, 117]
k (mmHg)	-	-	-	NA	3	[32]
t_p (h)	122.4	565.2	1008	[99, 113, 118]*	1008	[113, 118]*
t_r (h)	36	234	432	[39]	234	[39]

3.2.6 Comparison of the simulation outputs with conventional and moderate hypofractionated clinical data

In order to assess the impact of moderate hypofractionated schedules and to identify plausible radiosensitivity parameters, we simulated different fractionations, considering several prostate published values of α and β on our virtual tissues. Three fractionations were tested, 2, 2.5 and 3 Gy/fraction at 24h intervals. Six pairs of α and β from the literature (Valdagni *et al.* [98], Walsh *et al.* [99], Wang *et al.* [100], Miralbell *et al.* [101] and Brenner *et al.* [102]) were taken for each irradiation protocol. Values considered for the other parameters are presented on the right columns of Table 3.1. The experiment was conducted on the 21 virtual tissues. Five repetitions were performed per slice for each combination of fractionation and α/β ratio (a total of 1890 simulations). We identified the total dose, at each fractionation and for each α/β ratio, to eliminate 50%, 80%, 90%, 95%, 99% and 99.9% of tumour cells. Results were compared with the clinical ranges of total doses reported in the literature [3–8], i.e. between 74 and 80 Gy, 70 and 72 Gy and 57 and 62 Gy, for a 2, 2.5 and 3 Gy fractionation, respectively.

3.3 Results

3.3.1 Characteristics of the histopathological specimens

Each of our 21 virtual tissues was characterised by a tumour and an endothelial cell density. The tumour cell density ranged from 45 to 85% with a mean value of 67% ±10.8. The endothelial cell density had a minimal, mean and maximal value of 0.3, 2 ±1.8 and 8%, respectively.

3.3.2 Local sensitivity analysis

Fig. 3.2 shows the results of the local sensitivity analysis. RSC for the 10 parameters of the model are presented. They ranged from –1.31 to 0.79. The vascular density, d_{vasc}; α and the pO_2 value of endothelial cells, pO_2^{cap}, had the greatest impact on tumour cell survival. For these three parameters, an RSC lower than -1 was obtained. The oxygen diffusion coefficient, D; β, the oxygen consumption parameter, K_M, and the proliferation time of tumour cells, t_p, had an RSC between -0.9 and 0.2, which suggested a moderate impact. Lower tumour cell survival was obtained when these parameters were increased. In contrast, the oxygenation parameters V_{max} and m had positive values. An augmentation of these factors resulted in higher tumour cell survival to radiotherapy. The resorption time of dead cells, t_p presented a very limited effect on tumour cell response to irradiation.

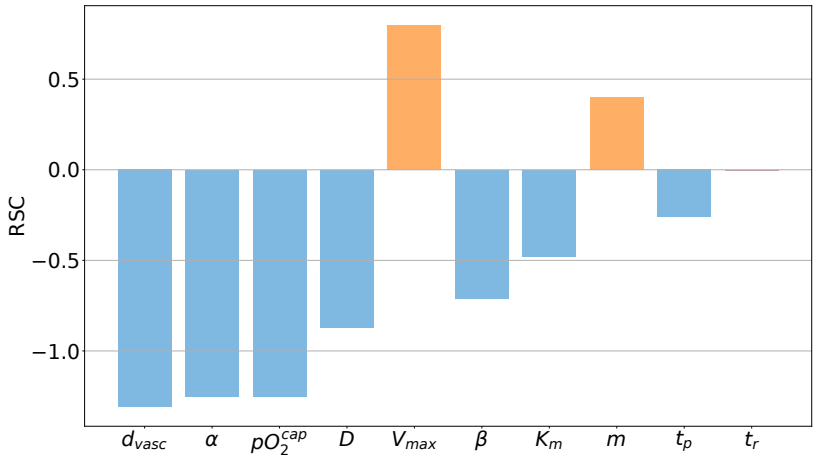

Figure 3.2 – Local sensitivity analysis results. RSC_k of the 10 parameters of the model in descending order of importance. Blue bars indicate that an augmentation of the parameter increases the elimination of tumour cells by irradiation. In contrast, orange bars are used when an increase of the parameter reduces the elimination of tumour cells.

3.3.3 Comparison of the simulation outputs with pO_2 *in vivo* data

The mean pO_2 obtained in each virtual tissue after simulation ranged from 0.5 to 16 mmHg, with a mean value of 3.7±4.0 mmHg over the 21 virtual tissues. This result was in line with pO_2 *in vivo* data from the literature. Mean values of 2.4 [119] and 4.5 [120] mmHg have been reported on prostate tumour. For the sake of comparison, a mean pO_2 of 30 mmHg has been observed in normal muscle [119]. Mean pO_2 obtained after simulation was linearly correlated with endothelial cell density ($R^2 = 0.996$). Fig. 3.3 presents the distributions of pO_2 values observed *in vivo* [119] and obtained after simulation with our computational model on the 21 virtual tissues.

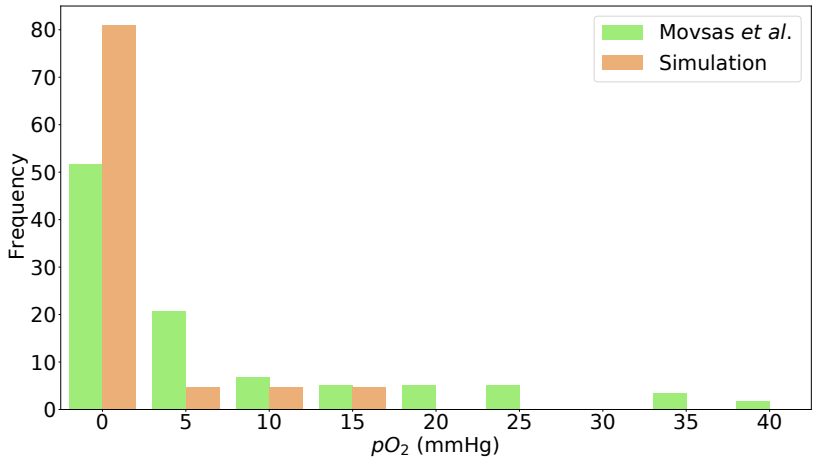

Figure 3.3 – Distribution of pO_2 in prostate tumour either reported from *in vivo* data or simulated with our model on the 21 virtual tissues. *In vivo* values from Movsas *et al.* [119] are represented in green and simulated values, in orange.

3.3.4 Comparison of the simulation outputs with conventional and moderate hypofractionated clinical data

Fig. 3.4 presents the total doses needed to eliminate of 50, 80, 90, 95, 99 and 99.9% of tumour cells considering the different values of the α and β parameters from the literature and 2, 2.5 and 3 Gy fractionations. Total doses within the clinical ranges were identified when taking the α and β values proposed by Miralbell *et al.* [101] ($\alpha = 0.041$ Gy^{-1} and $\beta = 0.0293$ Gy^{-2}) and eliminating 80% of tumour cells, when considering the α and β values suggested by Wang *et al.* [100] ($\alpha = 0.15$ Gy^{-1} and $\beta = 0.048$ Gy^{-2}) and eliminating 99% of tumour cells, and when using the α and β values reported by Valdagni *et al.* [98] and Walsh *et al.* [99] ($\alpha = 0.26$ Gy^{-1} and $\beta = 0.026$ Gy^{-2}, and $\alpha = 0.25$ Gy^{-1} and $\beta = 0.0625$ Gy^{-2}, respectively) and eliminating 99.9% of tumour cells.

3.4 Discussion

In this work, we adapted an existing computational model of tumour growth and response to radiotherapy. Prostate histopathological images were used to initialise simulations of tissue oxygenation, proliferation of tumour cells, oxygen-dependent response to irradiation and resorption of dead cells. We determined the impact of each parameter of the model. We compared the outcomes of our model with prostate clinical data from the literature, in terms of both pO_2 and response to various irradiation protocols (conventional and hypofractionated).

We chose the model of Espinoza *et al.* [32, 91] since its spatial scale was appropriate for our purposes. Furthermore, it integrated the most relevant biological mechanisms (oxygenation, tumour growth, response to irradiation based on the LQM and including the oxygen enhancement ratio, and resorption of dead cells). The use of prostate histopathological specimens as support for simulations and the choice

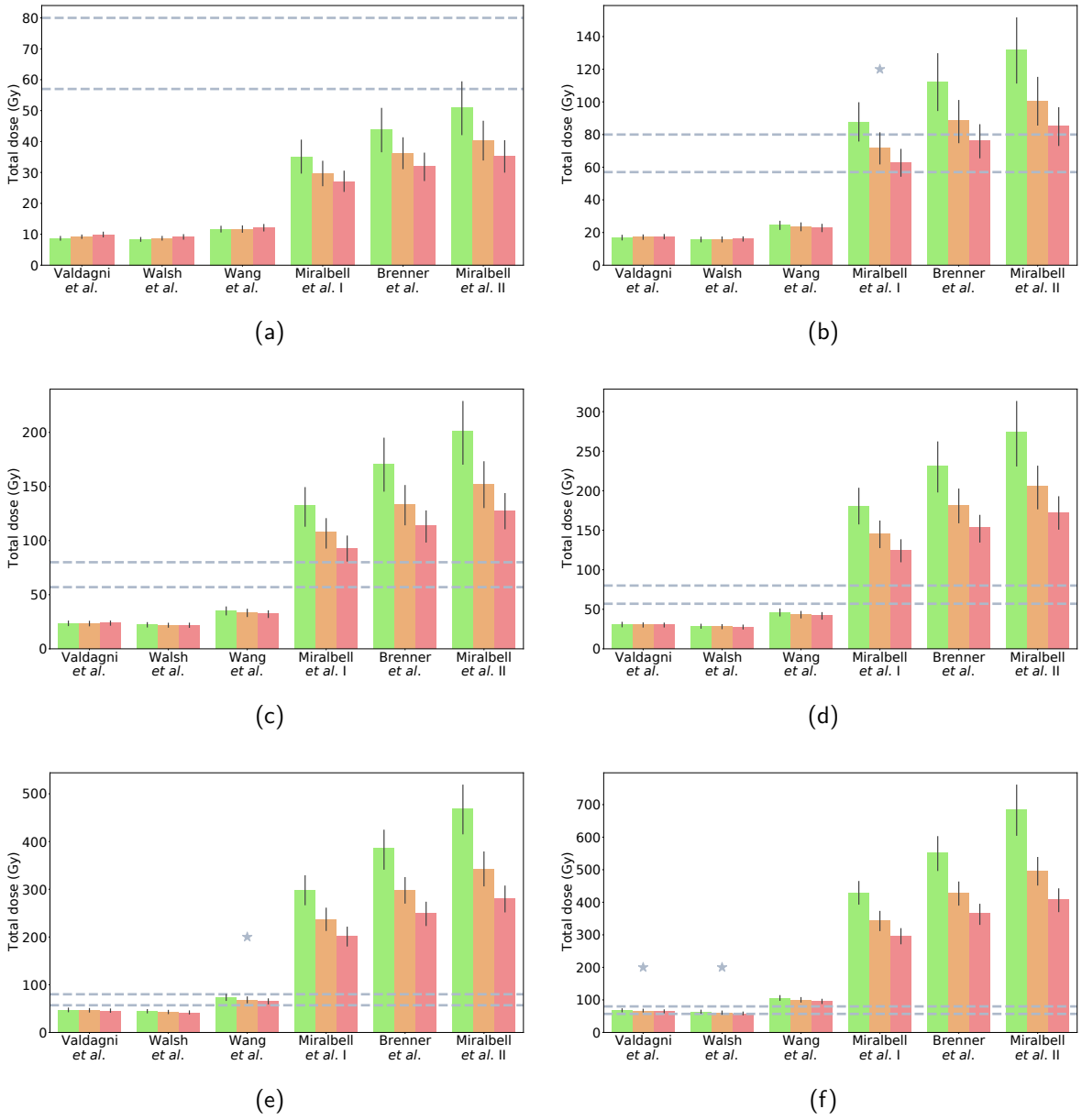

Figure 3.4 – Total doses for elimination of (a) 50, (b) 80, (c) 90, (d) 95, (e) 99 and (f) 99.9 % of tumour cells considering different published values of the α and β parameters (Valdagni *et al.* [98], Walsh *et al.* [99], Wang *et al.* [100], Miralbell *et al.* [101] and Brenner *et al.* [102]) and 2 (green), 2.5 (orange) and 3 (red) Gy fractionations. Dotted lines indicate the interval of the usual prostate clinical total dose. Simulated total doses within the clinical ranges are marked with a star. Error bars represent the heterogeneity among the 21 virtual tissues.

of the Netlogo software to implement the model imposed a 2D architecture.

Vascular density, observed on the histopathological specimens, the intrinsic radiosensitivity factor, α, and the constant pO_2 value of endothelial cells, pO_2^{cap}, were identified as the parameters of the model hav-

ing the most important effect on tumour cell survival. It can be deduced that tissues with a great number of endothelial cells supplying high levels of O_2 were well-oxygenated and therefore less radioresistant. It can also be assumed that a high value of the intrinsic radiosentivity parameter α facilitated tumour cell death due to irradiation. In contrast, the augmentation V_{max} and m resulted in an increased tumour cell survival. Indeed, raising these parameters provoked a higher oxygen consumption. Consequently, oxygenation levels were lower and cells were, thus, less radiosensitive.

Results of our computational model were compared with prostate *in vivo* data from the literature. Previous studies have reported that prostate tumours are hypoxic, with a mean pO_2 between 3 and 4.5 mmHg [119, 120]. *In silico* results belonged to this interval observed experimentally. A great heterogeneity over the 21 studied tissues was observed. A linear dependence of mean pO_2 on vascular density was reported. In Fig. 3.3, it can be observed our model slightly overestimated and underestimated the number of pO_2 values in the 0 - 5 and 5 - 10 mmHg intervals, respectively. This may be explained by the fact that, in our computational model, the pO_2 of endothelial cells was fixed at 42 mmHg whatever the size of the vessels. However, we could expect to have a higher pO_2 value for large capillaries, which would result in a slightly better oxygenation of the tissue in question.

Some computational models [31, 32] assume that local tumour control is achieved only if all clonogenic cells are sterilised by radiation. However, this consideration might prove to be too strict, as the immune system may be capable of destroying small clusters of tumour cells remaining after irradiation [121]. In Fig. 3.4, we supposed that different percentages of elimination of tumour cells suffice to avoid recurrence.

This work presents several limitations that will be tackled in the future. Firstly, some biological mechanisms which may also play an important role in tumour cell elimination were not included in our model. At the microscopic scale, hypoxia is recognised as inducing angiogenesis [122]. The dynamic evolution of the vascular system could impact the oxygenation and, consequently, the radiosensitivity of the whole tissue during simulation. The results of the local sensitivity analysis confirmed this idea. Indeed, vascular density is the parameter with the greatest influence on tumour elimination. Furthermore, the cell cycle distribution also has an impact on the response to irradiation. The model proposed by Titz *et al.* [92] suggests a way that we are exploring to include this mechanism in the next version of our model. The integration of mitotic catastrophe [28], instead of instantaneous apoptosis, as the main type of cell death after irradiation in the model may also affect the response of the virtual tissues to radiotherapy.

In addition, especially due to limitations of the simulation software Netlogo, our model only considered 2D computational tissues. Espinoza *et al.* [91] observed that 2D and 3D vascular architectures produce similar oxygenation. However, the other biological mechanisms of the model, like the proliferation of tumour cells, may behave differently in 2D and 3D simulation environments. A 3D version of the model will be developed in the future in a more efficient programming language allowing faster simulations.

Furthermore, the RSC calculated in our local sensitivity analysis provided a preliminary view of the impact of each factor of the model. However, these results must be taken cautiously since this one-at-a-time approach cannot detect interactions between parameters. A more robust analysis using, for example, the Morris [96] or Sobol [95] methods will be performed in the future.

Finally, prostate tumours show high heterogeneity among patients, regions of a same patient (some patients have several tumour foci) and even cells at the microscopic scale. This fact may significantly affect the response to radiotherapy. Our model can simulate heterogeneity at the microscopic scale (in

particular, in terms of vascular architecture) and can be calibrated to consider patient heterogeneity on radiosensitivity. A version of the model that will integrate a more macroscopic approach, especially using imagery (MRI and CT, corresponding to our histopathological specimens), to improve realism of our simulation will be developed in the future.

3.5 Conclusion

We were able to adapt an existing computational model of tumour growth and response to radiotherapy to be initialised with prostate histopathological specimens. A local sensitivity analysis showed that the vascular density and the intrinsic radiosensitivity parameter α had the most important effect on tumour cell death. The different biological mechanisms implemented in the model were compared with prostate *in vivo* data of the literature. The response to various irradiation protocols (conventional and hypofractionated) considering different radiosensitivities, given by α and β, were simulated. *In silico* total doses to achieve tumour control (defined as the elimination of 99.9% of tumour cells) within the clinical ranges were obtained when taking $\alpha = 0.15$ Gy^{-1}, $\beta = 0.048$ Gy^{-2} and, consequently, $\alpha/\beta = 3.1$ Gy. In the future, the model will be improved by expanding it to the macroscopic level and adding other biological mechanisms and parameters, such as angiogenesis, cell cycle and mitotic catastrophe.

In this chapter, the model of tumour response proposed by Espinoza *et al.* was adapted so that it could be used on prostate histopathological specimens. The performed local sensitivity analysis showed that the vascular density and the intrinsic radiosensitivity parameter α had the most important effects on the number of tumour cells after irradiation. Oxygen distributions obtained after simulation were in line with clinical data from the literature. Total doses to achieve tumour control in agreement with randomised trials of conventional and hypofractionated prostate irradiation schedules were identified.

Nevertheless, this work presents several limitations, mainly due to the implementation of the model in the simulation software Netlogo. Some radiobiological mechanisms which may play a major role in tumour control, such as the cell cycle distribution, mitotic catastrophe or angiogenesis resulting in the reoxygenation of the tissue, were not integrated. In addition, only a 2D configuration could be considered. Furthermore, the OAT local sensitivity analysis performed in this chapter did not fully explore the parameter space and appeared insufficient to detect interactions and non-linear effects.

In the next chapter, an original comprehensive model integrating every major radiobiological mechanism of the literature, considering both 2D and 3D configurations and implemented in C++ will be proposed. In addition, a thorough sensitivity analysis using the Morris screening method will be performed.

Part III

Developing an original *in silico* model of tumour response to predict biochemical recurrence

Chapter 4

Towards a reduced in silico model predicting biochemical recurrence after radiotherapy in prostate cancer

---

In this chapter, a reduced *in silico* mechanistic model of tumour response predicting biochemical recurrence after radiotherapy in prostate cancer is developed and implemented in C++. Firstly, an original comprehensive model integrating the main radiobiological of the literature is presented. Then, the results of an exhaustive sensitivity analysis performed on 21 prostate computational tissues using the Morris screening method are reported. TCP curves of the comprehensive model and 15 simplified versions excluding certain mechanisms are compared. Based on the results of the sensitivity analysis and the TCP curves, a reduced model of tumour response is proposed. Finally, a potential application of the model as a useful tool in a clinical context is described. Logistic regression is performed to predict biochemical recurrence after radiotherapy on 76 localised prostate cancer patients considering an output of the comprehensive and the reduced models. Results are compared with those of a classical radiomics approach.

The content of this chapter has been published in the international journal IEEE Transactions on Biomedical Engineering.

C. Sosa-Marrero, R. de Crevoisier, A. Hernández, P. Fontaine, N. Rioux-Leclercq, R. Mathieu, A. Fautrel, F. Paris and O. Acosta. «Towards a reduced *in silico* model predicting biochemical recurrence after radiotherapy in prostate cancer», *IEEE Trans. Biomed. Eng.*, **68**, pp. 2718-2729, 2021.

Preliminary versions of the work were presented at international conferences, in the form of peer-reviewed 4-page paper at IEEE ISBI 2019 and abstract at ESTRO 38.

C. Sosa-Marrero, O. Acosta, M. Castro, A. Hernández, N. Rioux-Leclercq, F. Paris and R. de Crevoisier, «Sensitivity analysis of an *in silico* model of tumour growth and radiation response», in *IEEE ISBI 2019*, pp. 1497-1500, 2019. (Oral communication)

C. Sosa-Marrero, O. Acosta, M. Castro, A. Hernández, N. Rioux-Leclerq, F. Paris and R. de Crevoisier, «Sensitivity analysis of an *in silico* model of tumour growth and response to radiotherapy», *Radiother. Oncol.* **133**. S527-S528., 2019. (In ESTRO 38 as poster)

4.1 Introduction

A large number of *in silico* models integrating some of the radiobiological mechanisms characterising cancer and the response to radiotherapy (in particular, those related to the 5 R's) have already been proposed. However, no work of the literature has simultaneously included, to our knowledge, dynamic oxygenation, mitotic catastrophe and cell cycle distribution allowing the simulation of a phase-dependent radiosensitivity for tumour cells. Moreover, although the independent contribution of different radiobiological mechanisms has been evaluated for some of the models through TCP or tumour density curves [31, 32, 39], an exhaustive sensitivity analysis to precisely identify the impact of each radiobiological parameter has not been performed yet.

The objectives of this work were thus to develop an original comprehensive *in silico* model of tumour response to radiotherapy integrating the major radiobiological mechanisms, to perform a thorough sensitivity analysis of the model in order to reduce the number of parameters and propose a more compact version equivalent in terms of TCP and tumour cell density and, finally, to demonstrate its clinical usefulness in the prediction of biochemical recurrence after prostate cancer radiotherapy.

4.2 Material and methods

4.2.1 Description of the model of tumour response to radiotherapy

General description

The developed *in silico* model of tumour response to radiotherapy considered either a 2D or a 3D prostate computational tissue (Fig. 4.4) where each pixel (20 μm $\times$ 20 μm) or voxel (20 μm $\times$ 20 μm $\times$ 20 μm) corresponded to a cell of one of the following 6 types: healthy (fibroblasts, macrophages, epithelial, smooth muscle, etc.), undamaged or lethally damaged tumour, pre-existing or neo-created endothelial and dead.

The model integrated the following radiobiological mechanisms, happening at different temporal and spatial scales: (i) oxygenation of the tissue, (ii) division of tumour cells, (iii) angiogenesis, (iv) division of healthy cells and (v) response to irradiation. A functional diagram of the model is presented in Fig. 4.1.

Oxygenation (Reoxygenation)

Oxygenation of the tissue was modeled, as in [91], using the reaction-diffusion equation (4.1)

$$\frac{\partial u(\boldsymbol{x},t)}{\partial t} = D^{O_2}\Delta u(\boldsymbol{x},t) - r(u(\boldsymbol{x},t)), \tag{4.1}$$

where $u(\boldsymbol{x},t)$ is the oxygen concentration; D^{O_2}, the oxygen diffusion coefficient and $r(u(\boldsymbol{x},t))$, the oxygen consumption, calculated, for healthy and tumour cells, with the Michaelis-Menten equation (4.2)

$$r(u(\boldsymbol{x},t)) = V_{max}^{O_2}\frac{u(\boldsymbol{x},t)}{u(\boldsymbol{x},t) + K_M^{O_2}} \tag{4.2}$$

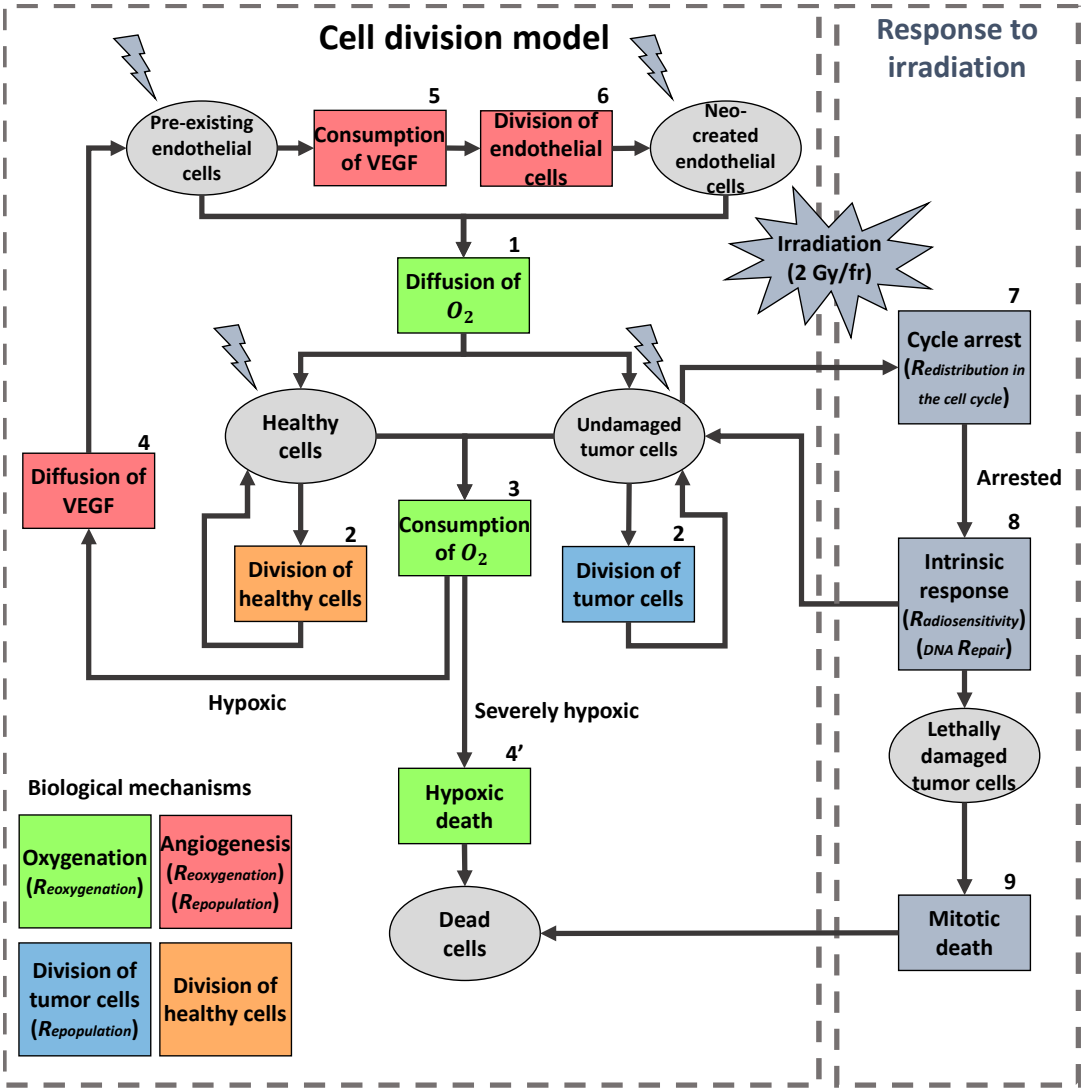

Figure 4.1 – Functional diagram of the model. The different types of simulated cells are represented with a gray ellipse. The different mechanisms are represented with a rectangle. The same color code as in Table 4.1 is used. Correspondences to the 5 R's are indicated in italics. Endothelial cells diffuse O_2 (1). Healthy and tumour cells divide (2) and consume O_2 (3). As a result, they may become hypoxic, in which case they diffuse VEGF (vascular endothelial growth factor) (4), or, if the O_2 levels are extremely low, severely hypoxic, which provokes their death (4'). VEGF is consumed by endothelial cells (5), resulting in their division (6). Tumour cells irradiated with a dose of 2 Gy per fraction are arrested (7). According to their intrinsic response to radiation (8), if their DNA can be repaired, they resume their division. If the damage caused by irradiation is lethal, they die at the next mitosis (mitotic death) (9).

where $V_{max}^{O_2}$ is the maximum oxygen consumption ratio and $K_M^{O_2}$, the Michaelis constant. Dead cells were considered to consume no oxygen.

Henry's law states that, at a constant temperature, the amount of gas dissolved in a liquid is propor-

tional to the partial pressure that the gas applies to the liquid (4.3),

$$p = K_H u, \tag{4.3}$$

with p, the partial pressure and K_H, the Henry's constant that depends on the gas, the liquid and the temperature. Using this relationship and redefining $K_M^{O_2}$ as $K_M^{O_2} := K_M^{O_2} K_H$ and $V_{max}^{O_2}$ as $V_{max}^{O_2} := V_{max}^{O_2} K_H$, the oxygenation of the tissue could be expressed as a function of the partial pressure of oxygen (4.4) [91]

$$\frac{\partial pO_2(\boldsymbol{x},t)}{\partial t} = D^{O_2} \Delta pO_2(\boldsymbol{x},t) - r(pO_2(\boldsymbol{x},t)), \tag{4.4}$$

with $r(pO_2(\boldsymbol{x},t))$ calculated for healthy and tumour cells as (4.5)

$$r(pO_2(\boldsymbol{x},t)) = V_{max}^{O_2} \frac{pO_2(\boldsymbol{x},t)}{pO_2(\boldsymbol{x},t) + K_M^{O_2}}. \tag{4.5}$$

Pre-existing and neo-created endothelial cells were supposed to have fixed pO_2 values pO_2^{preEnd} and pO_2^{neoEnd}, respectively. The steady state solution was obtained numerically using the finite differences method (see section 4.2.2 for further details). Healthy and tumour cells having a pO_2 lower than a threshold, pO_2^{nec}, were considered to die instantaneously due to hypoxia.

Division of tumour cells (Repopulation)

The tumour cell cycle was implemented like in the models proposed in [33] and [34]. It had a duration T_{tum} and was composed of 4 phases: G1 (gap 1), S (synthesis), G2 (gap 2) and M (mitosis). In our model, there existed a fifth phase, called G0 and placed out of the cycle, in which cells were quiescent. When an undamaged tumour cell arrived at the end of its cycle, it divided, replacing a healthy or dead cell of its Moore neighborhood of order N with a new tumour cell. If there was no adjacent healthy or dead cell, then it entered the phase G0.

Tumour cells with no available place in their Moore neighbourhood were initialised in phase G0. Tumour cells with at least an available place in their Moore neighbourhood were supposed to be distributed at the beginning of the simulation according to the following percentages: 60% in phase G1; 25%, in S; 7.5%, in G2 and 7.5%, in M [33].

Angiogenesis (Reoxygenation, repopulation)

The model of angiogenesis was based on the VEGF (vascular endothelial growth factor) diffusion. This protein, consumed by endothelial cells, is emitted by hypoxic cells to provoke the creation of blood vessels that satisfy their oxygen needs. The VEGF distribution was assumed to be given by the reaction-diffusion equation (4.6)

$$\frac{\partial v(\boldsymbol{x},t)}{\partial t} = D^{VEGF} \Delta v(\boldsymbol{x},t) - r(v(\boldsymbol{x},t)), \tag{4.6}$$

where D^{VEGF} is the diffusion coefficient and $r(v(\boldsymbol{x},t))$, the VEGF consumption, calculated, for endothelial cells, with the Michaelis-Menten equation

$$r(v(\boldsymbol{x},t)) = V_{max}^{VEGF}\frac{v(\boldsymbol{x},t)}{v(\boldsymbol{x},t)+K_M^{VEGF}}, \tag{4.7}$$

where V_{max}^{VEGF} is the maximum VEGF consumption ratio and K_M^{VEGF}, the Michaelis constant. Hypoxic cells (with a pO_2 value lower than a given threshold, pO_2^{hyp}) were supposed to have a fixed v value, v^{hyp} [39]. The finite differences method was used to obtain the numerical steady state solution (see section 4.2.2 for further details). A cycle duration, T_{end}, was defined for both pre-existing and neo-created endothelial cells. If at the end of its cycle, the VEGF concentration of an endothelial cell whose DNA had not been lethally damaged by irradiation exceeded a predetermined value $\bar{v}$, the cell in question divided. If not, it entered the quiescent phase G0, where it remained until a potential augmentation of $v(x,t)$. The new endothelial cell was placed in the most hypoxic direction [39].

Division of healthy cells

The duration of the healthy cell cycle T_{heal} was defined. When a cell whose DNA had not been lethally damaged by irradiation arrived at the end of its cycle, it divided, replacing a dead cell of its Moore neighborhood of order N with a new healthy cell. If there was no adjacent dead cell, then it entered the phase G0.

Response to irradiation (Redistribution in the cell cycle, radiosensitivity, DNA repair)

The response of every cell to irradiation was modeled as the survival fraction (SF) following the linear-quadratic equation and adjusted to consider the influence of the pO_2 (4.8) [31–33, 39]

$$SF = \exp\left(-\frac{\alpha}{m}d\ OER(pO_2) - \frac{\beta}{m^2}d^2 OER^2(pO_2)\right), \tag{4.8}$$

where α and β are the radiosensitivity parameters; d, the administered dose per session and OER, the oxygen enhancement ratio given by (7)

$$OER(pO_2) = \frac{m\ pO_2 + k}{pO_2 + k}, \tag{4.9}$$

with m, the maximum value of the OER (set to 3 [29]) and k, the partial pressure of oxygen such that $OER = (m+1)/2$ (3 mmHg). The radiosensitivity of tumour cells was supposed to vary throughout the cycle. Thus, cells were more sensitive in phases G2 and M and more resistant to irradiation in phase S [27]. Healthy and endothelial cells, significantly more radioresistant, had constant values of α and β throughout their cycle. Irradiated cells were arrested for a duration T_{arrest} at checkpoints located in transitions between phases G1/S and G2/M [31]. Cells lethally damaged by irradiation died by mitotic catastrophe.

4.2.2 Implementation of the model

The model was implemented in C++ using the Multiformalism Modeling and Simulation Library (M2SL) [44]. This in-house library previously developed in other biomedical modelling contexts [123], allows the integration of different processes arising at different temporal and spatial scales expressed with various formalisms (algebraic equations, partial differential equations and cell automata). In this work, we extended its functionalities to 2D and 3D arrays representing virtual tissues and allowing fast simulations of multiple simultaneous processes.

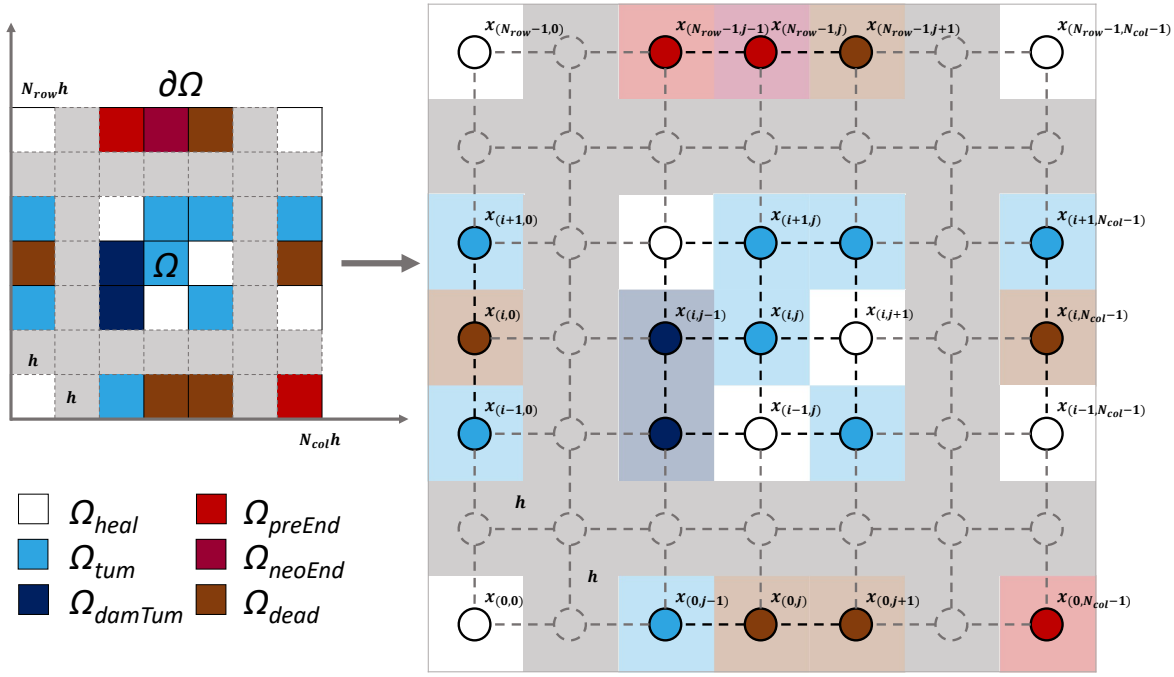

Figure 4.2 – Computational tissue Ω and regular mesh X considered to solve PDEs characterising oxygenation and the diffusion and consumption of VEGF

Numerical resolution of the PDEs characterising oxygenation and diffusion and consumption of VEGF

For each computational tissue Ω with boundary $\partial\Omega$ and containing $N_{row} \times N_{col}$ square cells of side h, we considered the discrete function $a(\boldsymbol{x})$ (4.10)

$$a(\boldsymbol{x}) = \begin{cases} 0, & if \quad healthy \\ 1, & if \quad undamaged\ tumour \\ 2, & if \quad lethally\ damaged\ tumour \\ 3, & if \quad pre\text{-}existing\ endothelial \\ 4, & if \quad neo\text{-}created\ endothelial \\ 5, & if \quad dead, \end{cases} \tag{4.10}$$

giving the type of every cell. Thus, the following sub-domains could be defined,

$$\begin{aligned}
&\Omega_{heal} = \{\boldsymbol{x} \in \Omega : a(\boldsymbol{x}) = 0\},\\
&\Omega_{tum} = \{\boldsymbol{x} \in \Omega : a(\boldsymbol{x}) = 1\},\\
&\Omega_{damTum} = \{\boldsymbol{x} \in \Omega : a(\boldsymbol{x}) = 2\},\\
&\Omega_{preEnd} = \{\boldsymbol{x} \in \Omega : a(\boldsymbol{x}) = 3\},\\
&\Omega_{neoEnd} = \{\boldsymbol{x} \in \Omega : a(\boldsymbol{x}) = 4\},\\
&\Omega_{dead} = \{\boldsymbol{x} \in \Omega : a(\boldsymbol{x}) = 5\},\\
&\Omega_{end} = \Omega_{preEnd} \cup \Omega_{neoEnd},\\
&\Omega_{nonEnd} = \Omega \backslash \Omega_{end}.
\end{aligned}$$

Oxygenation of the tissue is given by the following PDE system (4.11)

$$\begin{cases}
\frac{\partial pO_2(\boldsymbol{x},t)}{\partial t} = D^{O_2}\Delta pO_2(\boldsymbol{x},t) - r(pO_2(\boldsymbol{x},t)), \quad \forall \boldsymbol{x} \in \Omega_{nonEnd}, \quad t > 0\\
r(pO_2(\boldsymbol{x},t)) = V_{max}^{O_2}\frac{pO_2(\boldsymbol{x},t)}{pO_2(\boldsymbol{x},t)+K_M^{O_2}}, \quad \forall \boldsymbol{x} \in \Omega_{heal} \cup \Omega_{tum} \cup \Omega_{damTum}, \quad t \geq 0\\
r(pO_2(\boldsymbol{x},t)) = 0, \quad \forall \boldsymbol{x} \in \Omega_{dead}, \quad t \geq 0\\
pO_2(\boldsymbol{x},0) = 0, \quad \forall \boldsymbol{x} \in \Omega_{nonEnd}\\
pO_2(\boldsymbol{x},t) = pO_2^{preEnd}, \quad \forall \boldsymbol{x} \in \Omega_{preEnd}, \quad t \geq 0\\
pO_2(\boldsymbol{x},t) = pO_2^{neoEnd}, \quad \forall \boldsymbol{x} \in \Omega_{neoEnd}, \quad t \geq 0\\
\nabla pO_2(\boldsymbol{x},t) \cdot \boldsymbol{n} = 0, \quad \forall \boldsymbol{x} \in \partial\Omega, \quad t > 0.
\end{cases} \tag{4.11}$$

It was solved using the finite differences method. For this purpose, we defined a regular mesh X, in which each point $\boldsymbol{x_{(i,j)}}$, $i = 0, ..., N_{row} - 1$, $j = 0, ..., N_{col} - 1$ corresponded to the center of a cell of the computational tissue (Fig. 4.2).

The following subsets were considered

$$\begin{aligned}
&X_{heal} = \{\boldsymbol{x_{(i,j)}} \in \Omega_{heal}\},\\
&X_{tum} = \{\boldsymbol{x_{(i,j)}} \in \Omega_{tum}\},\\
&X_{damTum} = \{\boldsymbol{x_{(i,j)}} \in \Omega_{damTum}\},\\
&X_{preEnd} = \{\boldsymbol{x_{(i,j)}} \in \Omega_{preEnd}\},\\
&X_{neoEnd} = \{\boldsymbol{x_{(i,j)}} \in \Omega_{neoEnd}\},\\
&X_{dead} = \{\boldsymbol{x_{(i,j)}} \in \Omega_{dead}\},\\
&X_{end} = \{\boldsymbol{x_{(i,j)}} \in \Omega_{end}\},\\
&X_{nonEnd} = \{\boldsymbol{x_{(i,j)}} \in \Omega_{nonEnd}\}.
\end{aligned}$$

At each point of the mesh $\boldsymbol{x_{(i,j)}}$, the nth iteration of the pO_2 was therefore given by (4.12)

$$
\begin{aligned}
&pO_2{}^{(0)}_{(i,j)} = 0, \quad \forall i,j : \boldsymbol{x_{(i,j)}} \in X_{nonEnd} \\
&pO_2{}^{(n)}_{(i,j)} = pO_2^{preEnd}, \quad \forall i,j : \boldsymbol{x_{(i,j)}} \in X_{preEnd}, \quad \forall n \geq 0 \\
&pO_2{}^{(n)}_{(i,j)} = pO_2^{neoEnd}, \quad \forall i,j : \boldsymbol{x_{(i,j)}} \in X_{neoEnd}, \quad \forall n \geq 0 \\
&pO_2{}^{(n)}_{(i,j)} = pO_2{}^{(n-1)}_{(i,j)} + \Delta t \left(\frac{D^{O_2}}{h^2} \left(pO_2{}^{(n-1)}_{(i-1,j)} + pO_2{}^{(n-1)}_{(i,j-1)} - 4pO_2{}^{(n-1)}_{(i,j)} + pO_2{}^{(n-1)}_{(i,j+1)} + pO_2{}^{(n-1)}_{(i+1,j)} \right) \right. \\
&\quad \left. -r(pO_2{}^{(n-1)}_{(i,j)}) \right), \quad \forall i,j : \boldsymbol{x_{(i,j)}} \in X_{nonEnd}, \quad 0 < i < N_{row} - 1, \quad 0 < j < N_{col} - 1, \quad \forall n > 0 \\
&pO_2{}^{(n)}_{(0,j)} = pO_2{}^{(n-1)}_{(0,j)} + \Delta t \left(\frac{D^{O_2}}{h^2} \left(pO_2{}^{(n-1)}_{(0,j-1)} - 3pO_2{}^{(n-1)}_{(0,j)} + pO_2{}^{(n-1)}_{(0,j+1)} + pO_2{}^{(n-1)}_{(1,j)} \right) \right. \\
&\quad \left. -r(pO_2{}^{(n-1)}_{(0,j)}) \right), \quad \forall j : \boldsymbol{x_{(0,j)}} \in X_{nonEnd}, \quad j = 1, ..., N_{col} - 2, \quad \forall n > 0 \\
&pO_2{}^{(n)}_{(N_{row}-1,j)} = pO_2{}^{(n-1)}_{(N_{row}-1,j)} + \Delta t \left(\frac{D^{O_2}}{h^2} \left(pO_2{}^{(n-1)}_{(N_{row}-2,j)} + pO_2{}^{(n-1)}_{(N_{row}-1,j-1)} - 3pO_2{}^{(n-1)}_{(N_{row}-1,j)} \right. \right. \\
&\quad \left. \left. +pO_2{}^{(n-1)}_{(N_{row}-1,j+1)} \right) - r(pO_2{}^{(n-1)}_{(N_{row}-1,j)}) \right), \\
&\quad \forall j : \boldsymbol{x_{(N_{row}-1,j)}} \in X_{nonEnd}, \quad j = 1, ..., N_{col} - 2, \quad \forall n > 0 \\
&pO_2{}^{(n)}_{(i,0)} = pO_2{}^{(n-1)}_{(i,0)} + \Delta t \left(\frac{D^{O_2}}{h^2} \left(pO_2{}^{(n-1)}_{(i-1,0)} - 3pO_2{}^{(n-1)}_{(i,0)} + pO_2{}^{(n-1)}_{(i,1)} + pO_2{}^{(n-1)}_{(i+1,0)} \right) \right. \\
&\quad \left. -r(pO_2{}^{(n-1)}_{(i,0)}) \right), \quad \forall i : \boldsymbol{x_{(i,0)}} \in X_{nonEnd}, \quad i = 1, ..., N_{row} - 2, \quad \forall n > 0 \\
&pO_2{}^{(n)}_{(i,N_{col}-1)} = pO_2{}^{(n-1)}_{(i,N_{col}-1)} + \Delta t \left(\frac{D^{O_2}}{h^2} \left(pO_2{}^{(n-1)}_{(i-1,N_{col}-1)} + pO_2{}^{(n-1)}_{(i,N_{col}-2)} - 3pO_2{}^{(n-1)}_{(i,N_{col}-1)} \right. \right. \\
&\quad \left. \left. +pO_2{}^{(n-1)}_{(i+1,N_{col}-1)} \right) - r(pO_2{}^{(n-1)}_{(i,N_{col}-1)}) \right), \\
&\quad \forall i : \boldsymbol{x_{(i,N_{col}-1)}} \in X_{nonEnd}, \quad i = 1, ..., N_{row} - 2, \quad \forall n > 0 \\
&pO_2{}^{(n)}_{(0,0)} = pO_2{}^{(n-1)}_{(0,0)} + \Delta t \left(\frac{D^{O_2}}{h^2} \left(-2pO_2{}^{(n-1)}_{(0,0)} + pO_2{}^{(n-1)}_{(0,1)} + pO_2{}^{(n-1)}_{(1,0)} \right) - r(pO_2{}^{(n-1)}_{(0,0)}) \right), \\
&\quad if \quad \boldsymbol{x_{(0,0)}} \in X_{nonEnd}, \quad \forall n > 0 \\
&pO_2{}^{(n)}_{(0,N_{col}-1)} = pO_2{}^{(n-1)}_{(0,N_{col}-1)} \Delta t \left(\frac{D^{O_2}}{h^2} \left(pO_2{}^{(n-1)}_{(0,N_{col}-2)} - 2pO_2{}^{(n-1)}_{(0,N_{col}-1)} + pO_2{}^{(n-1)}_{(1,N_{col}-1)} \right) \right. \\
&\quad \left. -r(pO_2{}^{(n-1)}_{(0,N_{col}-1)}) \right), \quad if \quad \boldsymbol{x_{(0,N_{col}-1)}} \in X_{nonEnd}, \quad \forall n > 0 \\
&pO_2{}^{(n)}_{(N_{row}-1,0)} = pO_2{}^{(n-1)}_{(N_{row}-1,0)} + \Delta t \left(\frac{D^{O_2}}{h^2} \left(pO_2{}^{(n-1)}_{(N_{row}-2,0)} - 2pO_2{}^{(n-1)}_{(N_{row}-1,0)} + pO_2{}^{(n-1)}_{(N_{row}-1,1)} \right) \right. \\
&\quad \left. -r(pO_2{}^{(n-1)}_{(N_{row}-1,0)}) \right), \quad if \quad \boldsymbol{x_{(N_{row}-1,0)}} \in X_{nonEnd}, \quad \forall n > 0 \\
&pO_2{}^{(n)}_{(N_{row}-1,N_{col}-1)} = pO_2{}^{(n-1)}_{(N_{row}-1,N_{col}-1)} \Delta t \left(\frac{D^{O_2}}{h^2} \left(pO_2{}^{(n-1)}_{(N_{row}-2,N_{col}-1)} + pO_2{}^{(n-1)}_{(N_{row}-1,N_{col}-2)} \right. \right. \\
&\quad \left. \left. -2pO_2{}^{(n-1)}_{(N_{row}-1,N_{col}-1)} \right) - r(pO_2{}^{(n-1)}_{(N_{row}-1,N_{col}-1)}) \right), \\
&\quad if \quad \boldsymbol{x_{(N_{row}-1,N_{col}-1)}} \in X_{nonEnd}, \quad \forall n > 0
\end{aligned}
\tag{4.12}
$$

$$r(pO_{2_{(i,j)}}^{(n)}) = V_{max}^{O_2} \frac{pO_{2_{(i,j)}}^{(n)}}{pO_{2_{(i,j)}}^{(n)} + K_M^{O_2}}, \quad \forall i,j : \boldsymbol{x_{(i,j)}} \in X_{heal} \cup X_{tum} \cup X_{damTum}, \quad \forall n \geq 0$$
$$r(pO_{2_{(i,j)}}^{(n)}) = 0, \quad \forall i,j : \boldsymbol{x_{(i,j)}} \in X_{dead}, \quad \forall n \geq 0.$$

A time-step of $\Delta t = 10$ ms was taken. This value ensured the convergence of the algorithm.

The diffusion and consumption of VEGF is given by the PDE system (4.13)

$$\begin{cases} \frac{\partial v(\boldsymbol{x},t)}{\partial t} = D^{VEGF} \Delta v(\boldsymbol{x},t) - r(v(\boldsymbol{x},t)), \quad \forall \boldsymbol{x} \in \Omega_{nonHyp}, \quad t > 0 \\ r(v(\boldsymbol{x},t)) = V_{max}^{VEGF} \frac{v(\boldsymbol{x},t)}{v(\boldsymbol{x},t) + K_M^{VEGF}}, \quad \forall \boldsymbol{x} \in \Omega_{end}, \quad t \geq 0 \\ r(v(\boldsymbol{x},t)) = 0, \quad \forall \boldsymbol{x} \in \Omega_{nonEnd} \cap \Omega_{nonHyp}, \quad t \geq 0 \\ v(\boldsymbol{x},0) = 0, \quad \forall \boldsymbol{x} \in \Omega_{nonHyp} \\ v(\boldsymbol{x},t) = v^{hyp}, \quad \forall \boldsymbol{x} \in \Omega_{hyp}, \quad t \geq 0 \\ \nabla v(\boldsymbol{x},t) \cdot \boldsymbol{n} = 0, \quad \forall \boldsymbol{x} \in \partial\Omega, \quad t > 0, \end{cases} \tag{4.13}$$

with Ω_{hyp} and Ω_{nonHyp} defined as

$$\Omega_{hyp} = \{\boldsymbol{x} \in \Omega_{heal} \cup \Omega_{tum} \cup \Omega_{damTum} : pO_2(\boldsymbol{x},t) < pO_2^{hyp}\},$$
$$\Omega_{nonHyp} = \Omega \backslash \Omega_{hyp}.$$

As for the case of oxygenation, the finite differences method was used to solve (4.13). The same mesh (Fig. 4.2) and time-step were considered and the following subsets were defined

$$X_{hyp} = \{\boldsymbol{x_{(i,j)}} \in \Omega_{hyp}\},$$
$$X_{nonHyp} = \{\boldsymbol{x_{(i,j)}} \in \Omega_{nonHyp}\}.$$

The nth iteration of the VEGF concentration v was thus calculated at each point of the mesh $\boldsymbol{x_{(i,j)}}$ using (4.14)

$$v_{(i,j)}^{(0)} = 0, \quad \forall i,j : \boldsymbol{x_{(i,j)}} \in X_{nonHyp}$$

$$v_{(i,j)}^{(n)} = v^{hyp}, \quad \forall i,j : \boldsymbol{x_{(i,j)}} \in X_{hyp}, \quad \forall n \geq 0$$

$$v_{(i,j)}^{(n)} = v_{(i,j)}^{(n-1)} + \Delta t \left(\frac{D^{VEGF}}{h^2} \left(v_{(i-1,j)}^{(n-1)} + v_{(i,j-1)}^{(n-1)} - 4v_{(i,j)}^{(n-1)} + v_{(i,j+1)}^{(n-1)} + v_{(i+1,j)}^{(n-1)} \right) - r(v_{(i,j)}^{(n-1)}) \right),$$
$$\forall i,j : \boldsymbol{x_{(i,j)}} \in X_{nonHyp}, \quad 0 < i < N_{row} - 1, \quad 0 < j < N_{col} - 1, \quad \forall n > 0$$

$$v_{(0,j)}^{(n)} = v_{(0,j)}^{(n-1)} + \Delta t \left(\frac{D^{VEGF}}{h^2} \left(v_{(0,j-1)}^{(n-1)} - 3v_{(0,j)}^{(n-1)} + v_{(0,j+1)}^{(n-1)} + v_{(1,j)}^{(n-1)} \right) - r(v_{(0,j)}^{(n-1)}) \right),$$
$$\forall j : \boldsymbol{x_{(0,j)}} \in X_{nonHyp}, \quad j = 1, ..., N_{col} - 2, \quad \forall n > 0$$

$$
\begin{aligned}
&v^{(n)}_{(N_{row}-1,j)} = v^{(n-1)}_{(N_{row}-1,j)} + \Delta t \left(\frac{D^{VEGF}}{h^2} \left(v^{(n-1)}_{(N_{row}-2,j)} + v^{(n-1)}_{(N_{row}-1,j-1)} - 3v^{(n-1)}_{(N_{row}-1,j)} \right.\right. \\
&\left.\left. + v^{(n-1)}_{(N_{row}-1,j+1)} \right) - r(v^{(n-1)}_{(N_{row}-1,j)}) \right) \quad \forall j : \boldsymbol{x_{(N_{row}-1,j)}}, \in X_{nonHyp}, \quad j = 1, ..., N_{col} - 2, \quad \forall n > 0 \\
&v^{(n)}_{(i,0)} = v^{(n-1)}_{(i,0)} + \Delta t \left(\frac{D^{VEGF}}{h^2} \left(v^{(n-1)}_{(i-1,0)} - 3v^{(n-1)}_{(i,0)} + v^{(n-1)}_{(i,1)} + v^{(n-1)}_{(i+1,0)} \right) - r(v^{(n-1)}_{(i,0)}) \right), \\
&\forall i : \boldsymbol{x_{(i,0)}} \in X_{nonHyp}, \quad i = 1, ..., N_{row} - 2, \quad \forall n > 0 \\
&v^{(n)}_{(i,N_{col}-1)} = v^{(n-1)}_{(i,N_{col}-1)} + \Delta t \left(\frac{D^{VEGF}}{h^2} \left(v^{(n-1)}_{(i-1,N_{col}-1)} + v^{(n-1)}_{(i,N_{col}-2)} - 3v^{(n-1)}_{(i,N_{col}-1)} + v^{(n-1)}_{(i+1,N_{col}-1)} \right) \right. \\
&\left. - r(v^{(n-1)}_{(i,N_{col}-1)}) \right), \quad \forall i : \boldsymbol{x_{(i,N_{col}-1)}} \in X_{nonHyp}, \quad i = 1, ..., N_{row} - 2, \quad \forall n > 0 \\
&v^{(n)}_{(0,0)} = v^{(n-1)}_{(0,0)} + \Delta t \left(\frac{D^{VEGF}}{h^2} \left(-2v^{(n-1)}_{(0,0)} + v^{(n-1)}_{(0,1)} + v^{(n-1)}_{(1,0)} \right) - r(v^{(n-1)}_{(0,0)}) \right), \\
&if \quad \boldsymbol{x_{(0,0)}} \in X_{nonHyp}, \quad \forall n > 0 \\
&v^{(n)}_{(0,N_{col}-1)} = v^{(n-1)}_{(0,N_{col}-1)} + \Delta t \left(\frac{D^{VEGF}}{h^2} \left(v^{(n-1)}_{(0,N_{col}-2)} - 2v^{(n-1)}_{(0,N_{col}-1)} + v^{(n-1)}_{(1,N_{col}-1)} \right) - r(v^{(n-1)}_{(0,N_{col}-1)}) \right), \\
&if \quad \boldsymbol{x_{(0,N_{col}-1)}} \in X_{nonHyp}, \quad \forall n > 0 \\
&v^{(n)}_{(N_{row}-1,0)} = v^{(n-1)}_{(N_{row}-1,0)} + \Delta t \left(\frac{D^{VEGF}}{h^2} \left(v^{(n-1)}_{(N_{row}-2,0)} - 2v^{(n-1)}_{(N_{row}-1,0)} + v^{(n-1)}_{(N_{row}-1,1)} \right) \right. \\
&\left. - r(v^{(n-1)}_{(N_{row}-1,0)}) \right), \quad if \quad \boldsymbol{x_{(N_{row}-1,0)}} \in X_{nonHyp}, \quad \forall n > 0 \\
&v^{(n)}_{(N_{row}-1,N_{col}-1)} = v^{(n-1)}_{(N_{row}-1,N_{col}-1)} + \Delta t \left(\frac{D^{VEGF}}{h^2} \left(v^{(n-1)}_{(N_{row}-2,N_{col}-1)} + v^{(n-1)}_{(N_{row}-1,N_{col}-2)} \right.\right. \\
&\left.\left. - 2v^{(n-1)}_{(N_{row}-1,N_{col}-1)} \right) - r(v^{(n-1)}_{(N_{row}-1,N_{col}-1)}) \right), \quad if \quad \boldsymbol{x_{(N_{row}-1,N_{col}-1)}} \in X_{nonHyp}, \quad \forall n > 0 \\
&r(v^{(n)}_{(i,j)}) = V^{VEGF}_{max} \frac{v^{(n)}_{(i,j)}}{v^{(n)}_{(i,j)} + K^{VEGF}_{M}}, \quad \forall i, j : \boldsymbol{x_{(i,j)}} \in X_{end}, \quad \forall n \geq 0 \\
&r(v^{(n)}_{(i,j)}) = 0, \quad \forall i, j : \boldsymbol{x_{(i,j)}} \in X_{nonEnd} \cap X_{nonHyp}, \quad \forall n \geq 0.
\end{aligned}
\tag{4.14}
$$

Simulation sequence

M2SL provided the tools necessary for handling multi-scale simulations with different time-steps Δt. Oxygenation and diffusion and consumption of VEGF (fast mechanisms) were simulated considering $\Delta t_{fast} = 10$ ms. For the division of tumour, healthy and endothelial cells and their response to irradiation (slow mechanisms), $\Delta t_{slow} = 6$ h was taken. Results from both simulations were coupled every 6 h (Δt_{coup} = 6 h).

In deep, the following simulation sequence was considered (Fig. 4.3). A 2D array representing a computational tissue in which each element (pixel) corresponded to a cell was built. Firstly, based on the initial cell type map (giving the distribution of tumour, healthy and endothelial cells), oxygenation and

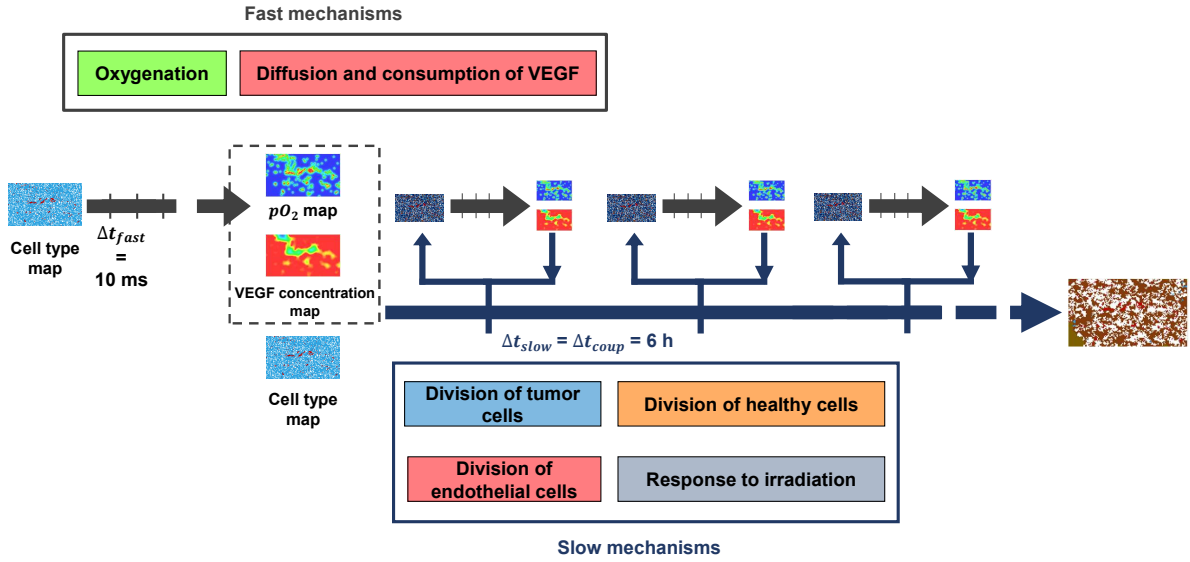

Figure 4.3 – Simulation sequence

diffusion and consumption of VEGF (fast mechanisms) were simulated with a time-step of 10 ms until finding steady values of pO_2 and VEGF concentration for every cell of the tissue. Secondly, considering the obtained pO_2 and VEGF concentration maps and the initial cell type distribution, a single iteration (6 h) of the division of tumour, healthy and endothelial cells and their response to irradiation (slow mechanisms) was simulated. Results were then coupled with those of the simulation of the fast mechanisms.

Subsequently, oxygenation and diffusion and consumption of VEGF were resimulated considering the updated cell type map, which could contain new endothelial cells providing O_2 or healthy, tumour and dead cells impacting on its consumption. Once the steady state had been reached for every cell of the tissue, a new iteration of the slow mechanisms was simulated considering the updated pO_2 and VEGF concentration maps. These latter two steps were repeated until the end of the simulation.

4.2.3 Morris screening method

The Morris screening method [96] offers an overall view of the influence of the parameters $\boldsymbol{x} = [x_1, ..., x_K]$ of a model $\mathbf{y} = f(\boldsymbol{x})$ on its outputs $\boldsymbol{y} = [y_1, .., y_L]$ with a low computational cost. Additionally, it provides information about the nature of the impact (linear or non-linear or having interactions with other parameters). It explores a K-dimensional cube regularly divided in p levels. In this space, for an output y_l, N elementary effects, given by (4.15) are calculated for each factor x_i. A clever experimental plan taking Δ, the discrete variation of the parameter, equal to $\frac{p}{2(p-1)}$ with p even, is used. It requires, in total, $N(K+1)$ evaluations of the model.

$$EE_i = \frac{f(x_1, ..., x_i, ..., x_K) - f(x_1, ..., x_i + \Delta, ..., x_K)}{\Delta}. \tag{4.15}$$

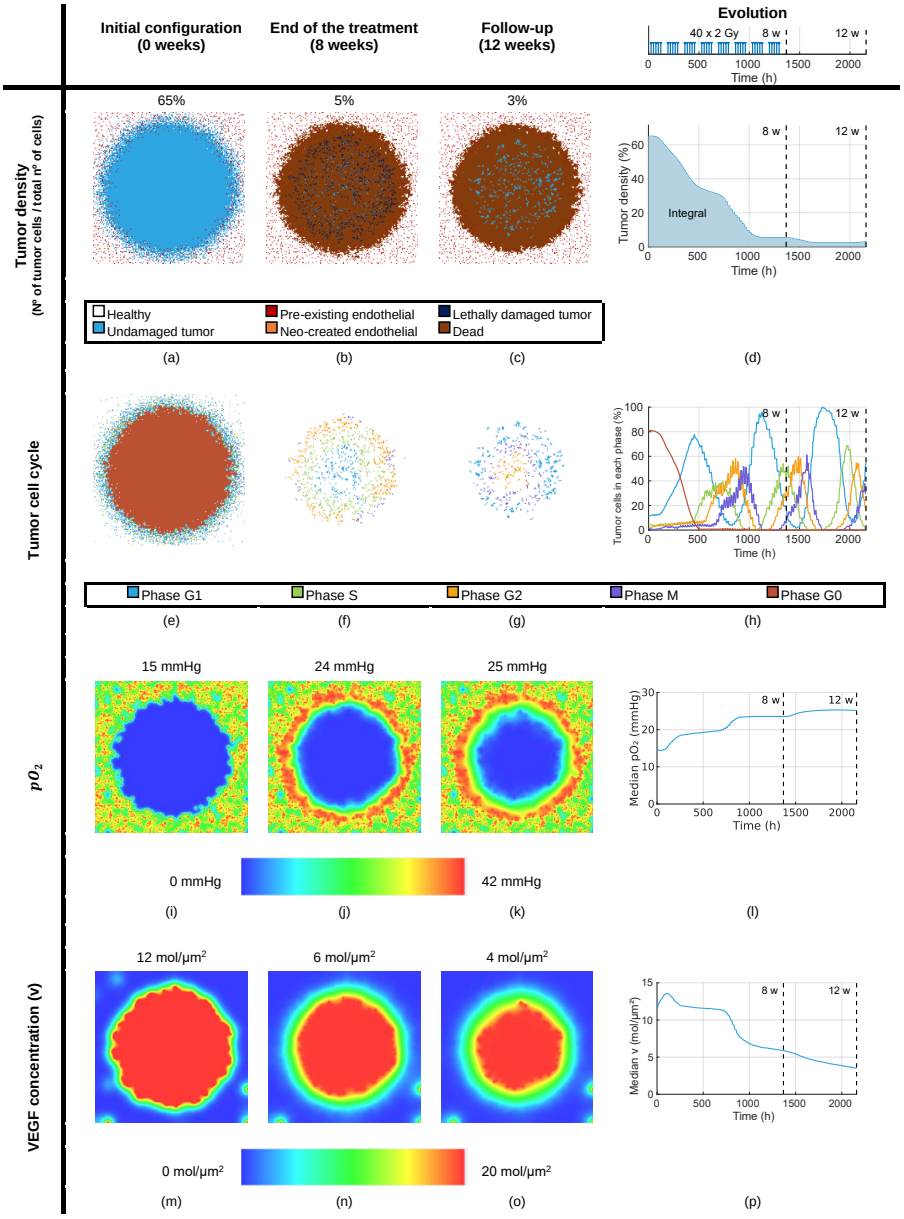

Figure 4.4 – Example of a 40 × 2 Gy treatment on a synthetic tissue. Tumour density at (a) the beginning of the simulation ($t = 0$ weeks); (b) the end of a 40 × 2 Gy treatment ($t = 8$ weeks) and (c) $t = 12$ weeks after the beginning of the treatment; (d) evolution of tumour density (the integral of tumour density can be deduced); corresponding distribution of tumour cells in the cycle at (e) $t = 0$ weeks, (f) $t = 8$ weeks and (g) $t = 12$ weeks; (h) evolution of the distribution of tumour cells in the cycle; pO_2 map at (i) $t = 0$ weeks; (j) $t = 8$ weeks and (k) $t = 12$ weeks; (l) evolution of the median pO_2 of the tissue; VEGF concentration map at (m) $t = 0$ weeks; (n) $t = 8$ weeks and (o) $t = 12$ weeks and (p) evolution of the median VEGF concentration of the tissue.

The mean and standard deviation ($\mu_i^* \pm \sigma_i$) over the absolute values [97] of the elementary effects are computed for each parameter. The Euclidean distance of each point (μ_i^*, σ_i) to the origin, $S_i = \sqrt{\mu_i^{*2} + \sigma_i^2}$, can be calculated as an indicator of the impact of the parameter in question [37]. The prostate-specific ranges presented in Table 4.1 were considered for the $K = 33$ parameters of the model. They were obtained calculating, respectively, 0.7 and 1.3 of the minimum P^{min} and maximum P^{max} values extracted from the literature or our radiobiological expertise. Ranges of the angiogenesis parameters were based on the global results of our previous study of vasculature in orthotopic mouse prostate cancer [124].

4.2.4 Tumour control probability curves

Tumour control probability (TCP) curves, typically used in clinical trials [121, 127], were generated as virtual endpoints in the simulations. A tumour was supposed to be controlled when the computational tissue did not contain any undamaged tumour cell [31, 39]. Using this definition, TCP curves can be fitted by the sigmoid function (4.16)

$$TCP(D) = \frac{1}{1 + \exp(-a(D - b))}, \tag{4.16}$$

where D is the total dose; a, the tangent at the inflection point and b, its shift. It can be noticed that a value of D equal to b leads to a TCP of 50% (TCP_{50}). Thus, b can be interpreted as the dose necessary to have a tumour control probability of 50% (TCD_{50}).

4.2.5 Simplification of the model

Based on the results of the sensitivity analysis, the initial comprehensive model was contrasted, through TCP curves, with simplified versions where different mechanisms or sub-mechanisms were progressively removed. Firstly, the complete model was compared with 4 reduced versions that did not consider angiogenesis, healthy cell division, cycle arrest or the response to irradiation of healthy and endothelial cells. Then, the differences between the comprehensive model and simplified versions that did not include 2-and-3-element combinations of these mechanisms were studied. Finally, the complete model was contrasted with a reduced version that integrated neither angiogenesis, nor healthy cell division nor cycle arrest, nor the response to irradiation of healthy and endothelial cells.

4.2.6 Initialisation of the model from prostate histological cuts

In order to perform simulations on realistic configurations of tumour and vascular cells, HES and CD31 prostate histological cuts from 7 patients treated with radical prostatectomy were used to initialise the model for the sensitivity analysis and the simplification experiments. Tumour foci were delineated on the HES axial slides (Fig. 4.5a) and a CD31 staining (Fig. 4.5b) was carried out to identify the blood vessels. Twenty-one regions of interest (ROI) of approximately 2 mm × 1.2 mm (100 pixels × 60 pixels) were selected from the tumour foci to create 21 initial computational tissues with different tumour and vascular densities. An example of ROI and the corresponding virtual tissue are presented in Fig. 4.5c and d, respectively.

Table 4.1 – Ranges and reference values of the 33 parameters of the comprehensive model, classified by radiobiological mechanism

Oxygenation		
Factor	**Range**	**Reference value**
pO_2^{nec} (mmHg)	0 - 1.3 [31, 33]	0.7
D^{O_2} (μm^2/ms)	1.02 - 2.87 [91]	1.84
$V_{max}^{O_2}$ (mmHg/ms)	0.006 - 0.029 [91]	0.015
$K_M^{O_2}$ (mmHg)	0.119 - 7.67 [91]	3.04
pO_2^{preEnd} (mmHg)	8.4 - 93.6 [104]	42
pO_2^{neoEnd} (mmHg)	8.4 - 93.6 [104]	42

(a)

Division of tumour cells		
Factor	**Range**	**Reference value**
T_{tum} (h)	85 - 1310 [32, 118]	565
N	1 - 3 [31]	1

(b)

Angiogenesis		
Factor	**Range**	**Reference value**
T_{end} (h)	1680 - 3120	2400
D^{VEGF} (μm^2/ms)	1.4 - 2.6	2
V_{max}^{VEGF} (mol/μm^{2}ms)	0.005 - 0.007	0.006
K_M^{VEGF} (mol/μm^2)	1.75 - 3.25	2.5
pO_2^{hyp} (mmHg)	3.5 - 6.5 [31]	5
$\bar{v}$ (mol/μm^2)	10.5 - 19.5	15
v^{hyp} (mol/μm^2)	14 - 26	20

(c)

Division of healthy cells		
Factor	**Range**	**Reference value**
T_{heal} (h)	171 - 2620	1130

(d)

Response to irradiation		
Factor	**Range**	**Reference value**
α_{heal} (Gy^{-1})	$7 \cdot 10^{-4}$ - $1.3 \cdot 10^{-3}$	0.001
α/β_{heal} (Gy)	0.7 - 13	5.5
α_{tumG1} (Gy^{-1})	0.024 - 0.356 [125, 126]	0.154
α/β_{tumG1} (Gy)	0.7 - 13 [125, 126]	5.5
α_{tumS} (Gy^{-1})	0.017 - 0.256 [125, 126]	0.111
α/β_{tumS} (Gy)	0.7 - 13 [125, 126]	5.5
α_{tumG2} (Gy^{-1})	0.025 - 0.381 [125, 126]	0.165
α/β_{G2} (Gy)	0.7 - 13 [125, 126]	5.5
α_{tumM} (Gy^{-1})	0.028 - 0.425 [125, 126]	0.184
α/β_{tumM} (Gy)	0.7 - 13 [125, 126]	5.5
α_{tumG0} (Gy^{-1})	0.105 - 0.195 [125, 126]	0.15
α/β_{tumG0} (Gy)	0.7 - 13 [125, 126]	5.5
α_{preEnd} (Gy^{-1})	$7 \cdot 10^{-4}$ - $1.3 \cdot 10^{-3}$ [31]	0.001
α/β_{preEnd} (Gy)	0.7 - 13 [31]	5.5
α_{neoEnd} (Gy^{-1})	$7 \cdot 10^{-4}$ - $1.3 \cdot 10^{-3}$ [31]	0.001
α/β_{neoEnd} (Gy)	0.7 - 13 [31]	5.5
T_{arrest} (h)	4.2 - 39	18

(e)

Parameters ranges, used for the sensitivity analysis, were extracted from the literature and our radiobiological expertise. Reference values were defined as intermediate values within the ranges.

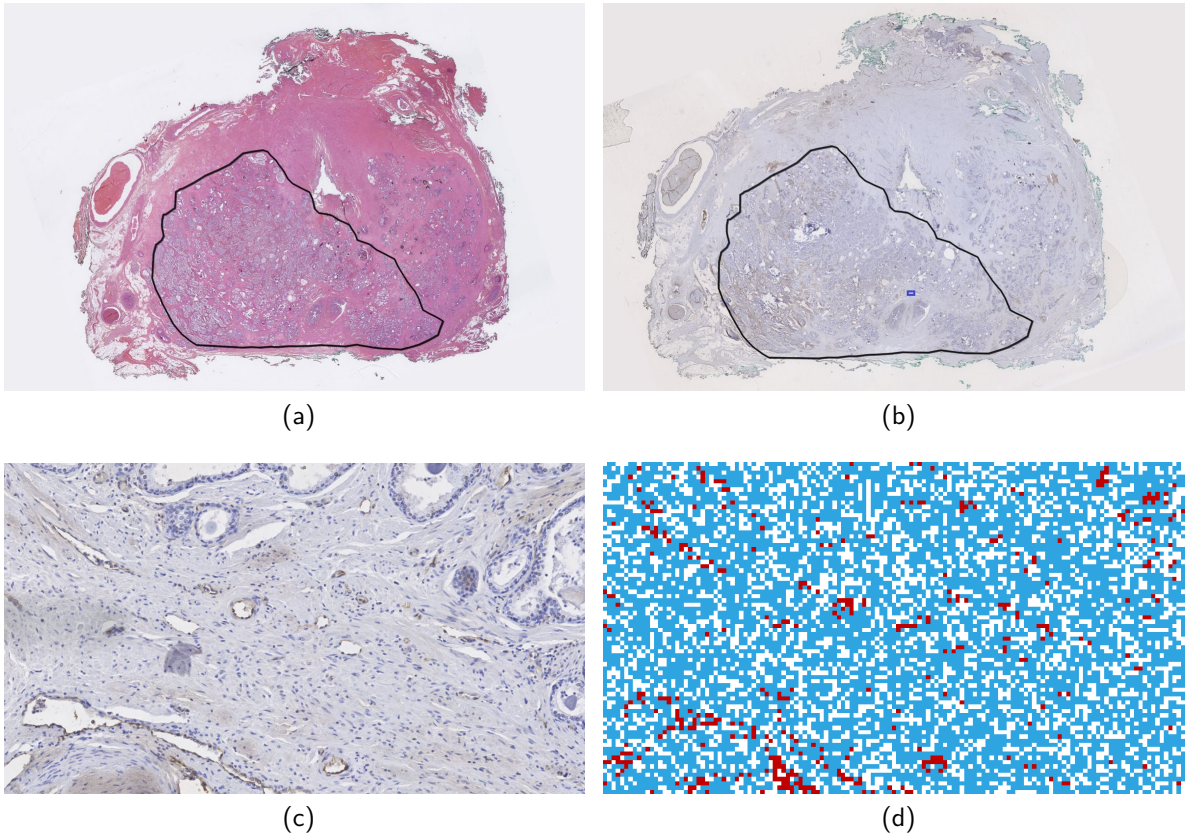

Figure 4.5 – Example of (a) HES staining of a prostate histological cut with tumour focus delineated by an anatomopathologist; (b) corresponding CD31 staining; (c) CD31 staining region of interest where vessels can be identified in brown and (d) initial computational tissue, where healthy cells are represented in white; undamaged tumour, in light blue and pre-existing endothelial, in red.

4.2.7 Validation of the model. Biochemical recurrence prediction

A first clinical validation of both the comprehensive and the reduced model in terms of biochemical recurrence prediction was performed. A cohort of 76 localised prostate cancer patients having undergone EBRT [12] was used for this purpose. Patient, tumour and treatment characteristics are presented in Supplementary Table I. Patients were followed up by means of clinical examination and PSA analysis every 6 months for 5 years after the end of irradiation. Nine patients suffered biochemical recurrence, defined according to the Phoenix criteria [128]. Our IRB approved this retrospective study.

The logistic model (stratified 3-fold cross-validation, 1000 repetitions) was used to predict biochemical recurrence. A first prediction was made from 3 pre-treatment imaging parameters, namely maximal tumour area and average ADC and T2w, obtained from 3.0 T MRI.

Biochemical recurrence was then predicted using the tumour area at $t = 8$ weeks output given by the comprehensive and reduced *in silico* models. For this purpose, 76 virtual tissues analogous to the 76 patients of the cohort were built from their respective average ADC and T2w values, correlated with cell density [129], and maximal tumour areas observed before treatment. The radiotherapy protocol

administered to each patient of the cohort (a total dose of 74 - 80 Gy delivered in 2 Gy fractions from Monday to Friday) was then simulated on the corresponding virtual tissue. Reference values given in Table 4.1 were taken for every parameter except for the highly influential hypoxic death threshold pO_2^{nec}, for which a low value was fixed. An initial vascular density of 3.8% [31], within the ranged observed in our histological cuts, was considered for every virtual tissue. Endothelial cells were supposed to be randomly distributed forming a poorly-vascularised tumour core. Given the stochastic component of the model, each simulation was repeated 5 times and the mean output value was taken.

4.3 Results

4.3.1 Integrative model of tumour response to radiotherapy

As a proof of concept, a 40 × 2 Gy treatment, typically applied in prostate cancer, was tested on a synthetic tissue. Results are presented in Fig. 4.4. Tumour density, cell cycle, $pO_2(x,t)$ and $v(x,t)$ maps at the beginning of the simulation ($t = 0$ weeks), $t = 8$ weeks (end of the treatment) and $t = 12$ weeks are shown. Curves of tumour density, cell cycle distribution and median pO_2 and v evolution through time are also presented.

4.3.2 Sensitivity analysis

The sensitivity analysis using the Morris method was performed on the 21 computational tissues obtained from the prostate histological cuts, considering a treatment of 40 × 2 Gy, administered every 24 h from Monday to Friday. The tumour density 12 weeks after the beginning of the treatment and its integral over time were used as endpoints. The value of Δ, considering $p = 20$, was normalised for each parameter as $\frac{\Delta}{1.3P^{max}-0.7P^{min}}$. In order to ensure convergence, $N = 100$ was taken. A total of $21 \times 100 \times (33 + 1) = 71400$ simulations were thus performed. The Euclidean distances S_i of the 33 parameters of the complete model for the 2 outputs considered are presented in Fig. 4.6.

The duration of the tumour cell cycle, T_{tum}, and the radiosensitivity parameter of tumour cells in the phase G1, α_{tumG1}, were identified as the factors having the highest impact on the tumour density at $t =$ 12 weeks (Fig. 4.6a). Other radiosensitivity parameters of tumour cells (α_{tumG2}, α/β_{tumG1}, α_{tumM} and α_{tumS}) and oxygenation factors, like pO_2^{nec}, $K_M^{O_2}$, pO_2^{preEnd} and $V_{max}^{O_2}$, had a considerable impact on this output as well.

T_{tum} was also the most influential parameter on the integral of tumour density (Fig. 4.6b). The hypoxic death threshold, pO_2^{nec}, had the second most important effect. Other factors of the oxygenation mechanism, like pO_2^{preEnd}, $V_{max}^{O_2}$, $K_M^{O_2}$ and D^{O_2} and the radiosensitivity parameters of tumour cells, especially those of the phase G1, also had a significant impact on the integral of tumour density.

In contrast, these results suggest that parameters associated with angiogenesis (in red), the division of healthy cells (in orange) and the response to irradiation of healthy and endothelial cells (in purple) were negligible for both the tumour density at $t = 12$ weeks and the integral of tumour density endpoints.

The impact of parameters located to the right of the dashed lines in Fig. 4.6 was indistinguishable from the uncertainty due to the stochastic nature of the model.

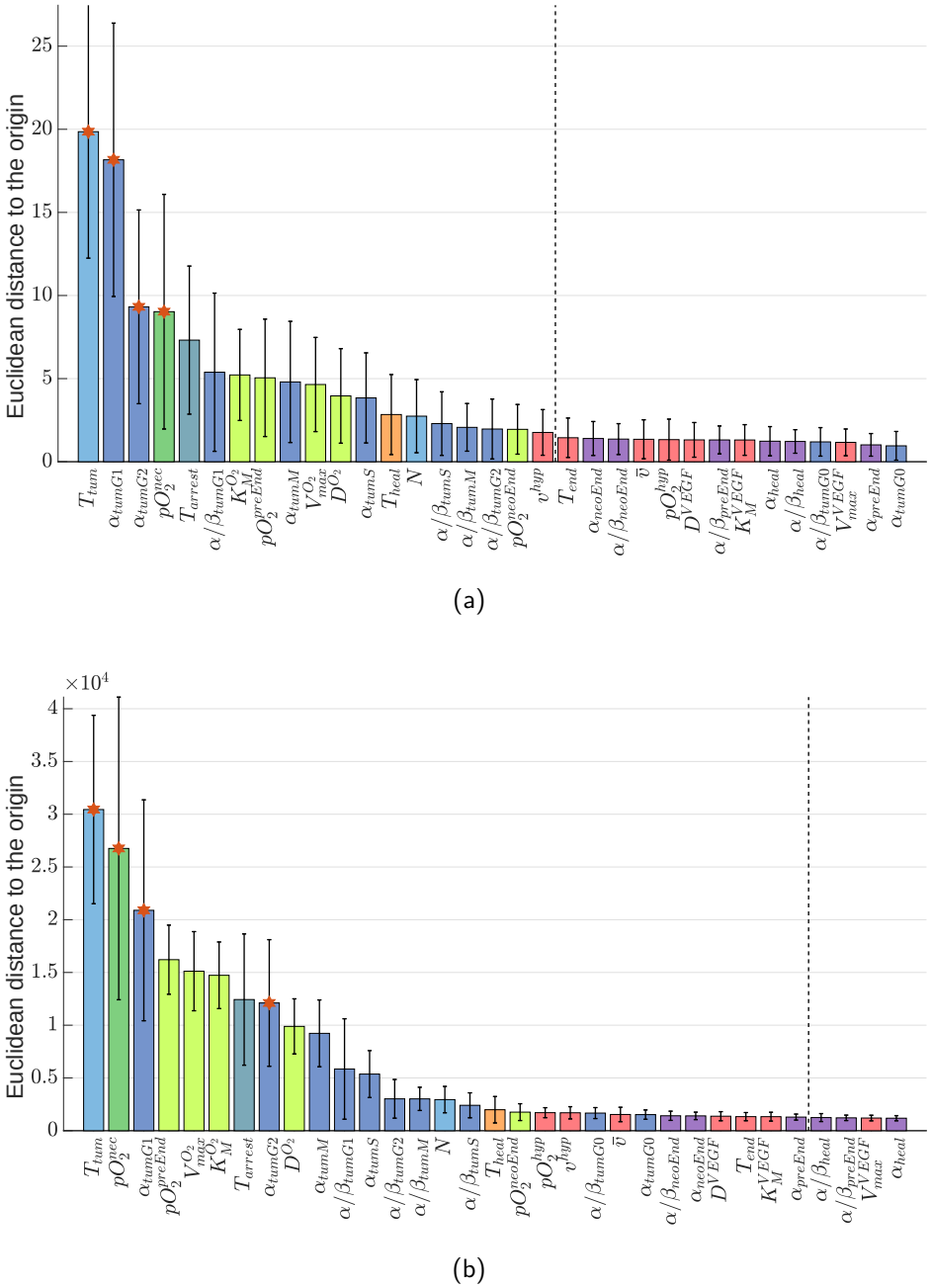

Figure 4.6 – Sensitivity analysis results. Euclidean distances to the origin, S_i, of the 33 parameters in descending order of importance taking as output: (a) the tumour density at $t = 12$ weeks and (b) the integral of tumour density. Twenty-ones computational tissues obtained from prostate histological cuts of 7 patients were used for this analysis. Error bars represent the heterogeneity of S_i among the different tissues. The same color code as in Table 4.1 is used. The effect of parameters to the right of the dashed lines is indistinguishable from the uncertainty caused by the intrinsic stochastic component of the model

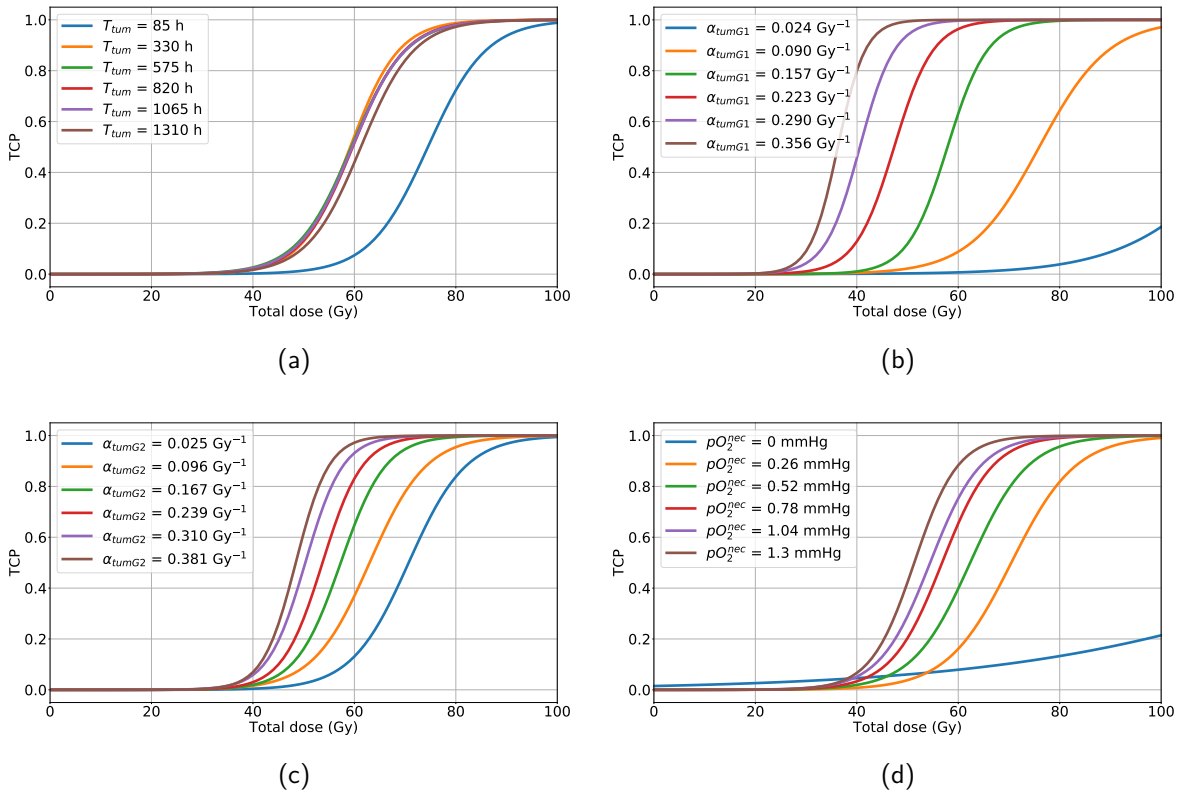

Figure 4.7 – TCP curves considering different values of (a) T_{tum}, (b) α_{tumG1}, (c) α_{tumG2} and (d) pO_2^{nec}, identified with a red star as the most important parameters in Fig. 4.6. A 2 Gy fractionation from Monday to Friday was used for every simulation. Six equidistant values within the ranges presented in Table 4.1 were considered for each studied factor. Reference values defined in the same table were used for the other parameters. A total of 210 simulations (10 repetitions × 21 computational tissues) were performed to build each TCP curve.

To better illustrate the impact of the most important parameters of the model, TCP curves are presented in Fig. 4.7 for 6 different values of T_{tum}, α_{tumG1}, α_{tumG2} and pO_2^{nec} within the ranges specified in Table 4.1. Reference values indicated in the same table were taken for the constant parameters. A 2 Gy fractionation administered every 24 h from Monday to Friday was considered. The experiment was repeated 10 times for each of the 21 computational tissues (a total of 210 simulations per curve).

It can be noticed that a small value of T_{tum} (85 h) complicated tumour control. There seemed to be no major variation between TCP curves for the other values of T_{tum} (Fig. 4.7a). Tumour control probabilities increased with the radiosensitivity parameters of tumour cells in phases G2, α_{tumG2}, and especially G1, α_{tumG1}, (Fig. 4.7c and b, respectively). Finally, the threshold of hypoxic death pO_2^{nec} (Fig. 4.7d) also had a significant effect on the TCP curves. Low values of this parameter, especially 0 mmHg (no hypoxic death at all), considerably complicated tumour control.

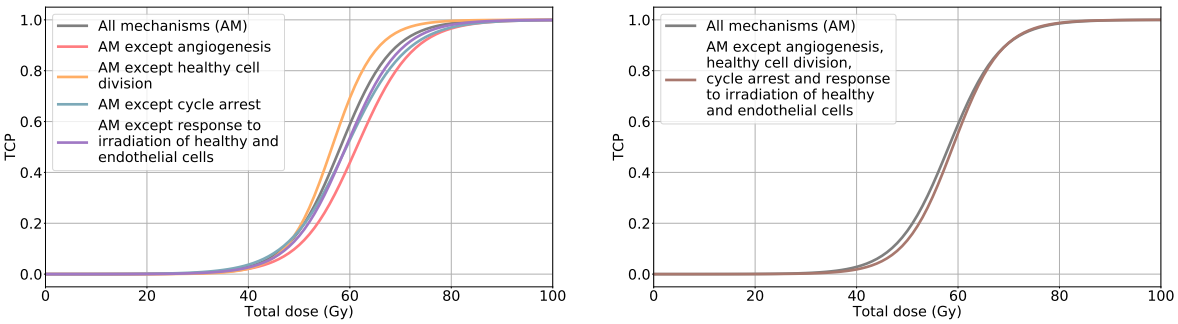

Figure 4.8 – TCP curves excluding (a) one and (b) 4 mechanisms or sub-mechanisms. A 2 Gy fractionation from Monday to Friday was simulated. The reference parameter values presented in Table 4.1 were considered. A total of 210 simulations (10 repetitions × 21 computational tissues) were performed to build each TCP curve. The same color code as in Table 4.1 is used.

4.3.3 Simplification of the model

The TCP curves obtained for the comprehensive model and the reduced versions are presented in Fig. 4.8. The reference parameter values presented in Table 4.1 and a 2 Gy fractionation were used for every repetition. As in Fig. 4.7, each TCP curve was built from $21 \times 10 = 210$ simulations.

The exclusion of angiogenesis from the model slightly complicated tumour control, whereas somewhat higher TCP values were obtained when the division of healthy cells was not considered. There seemed to be no major difference when the cycle arrest or the response to irradiation of healthy and endothelial cells were not included in the model (Fig. 4.8a).

The TCP curve obtained when angiogenesis, healthy cell division, cycle arrest and the response to irradiation of healthy and endothelial cells were simultaneously excluded is shown in Fig. 4.8b. No significant difference with respect to the reference TCP curve could be observed. It can be thus concluded that a simplified version of the model which considers neither angiogenesis nor healthy cell division nor cycle arrest nor the response to irradiation of healthy and endothelial cells (Fig. 4.9) is equivalent to the complete model integrating these mechanisms and sub-mechanism in terms of TCP. This reduced version includes only 18 parameters against 33 of the comprehensive model.

The TCP curves of the intermediate reduced versions excluding 2 and 3 mechanism or sub-mechanism combinations, as well as the values and the absolute and relative variations of the sigmoid constants a and b for every TCP curve can be found in Fig. 4.9.

4.3.4 Validation of the model. Biochemical recurrence prediction

Results of the biochemical recurrence predictions are presented in Fig. 4.10. Mean ROC curves and confidence intervals obtained after 1000 repetitions for the 3 different sets of features are shown. The corresponding mean AUC values are indicated. Biochemical recurrence predictions based on the tumour area at $t = 8$ weeks output of the comprehensive (AUC $= 0.81 \pm 0.02$) and reduced (AUC $= 0.82 \pm 0.02$) *in silico* models were significantly better than those obtained from the pre-treatment maximal tumour

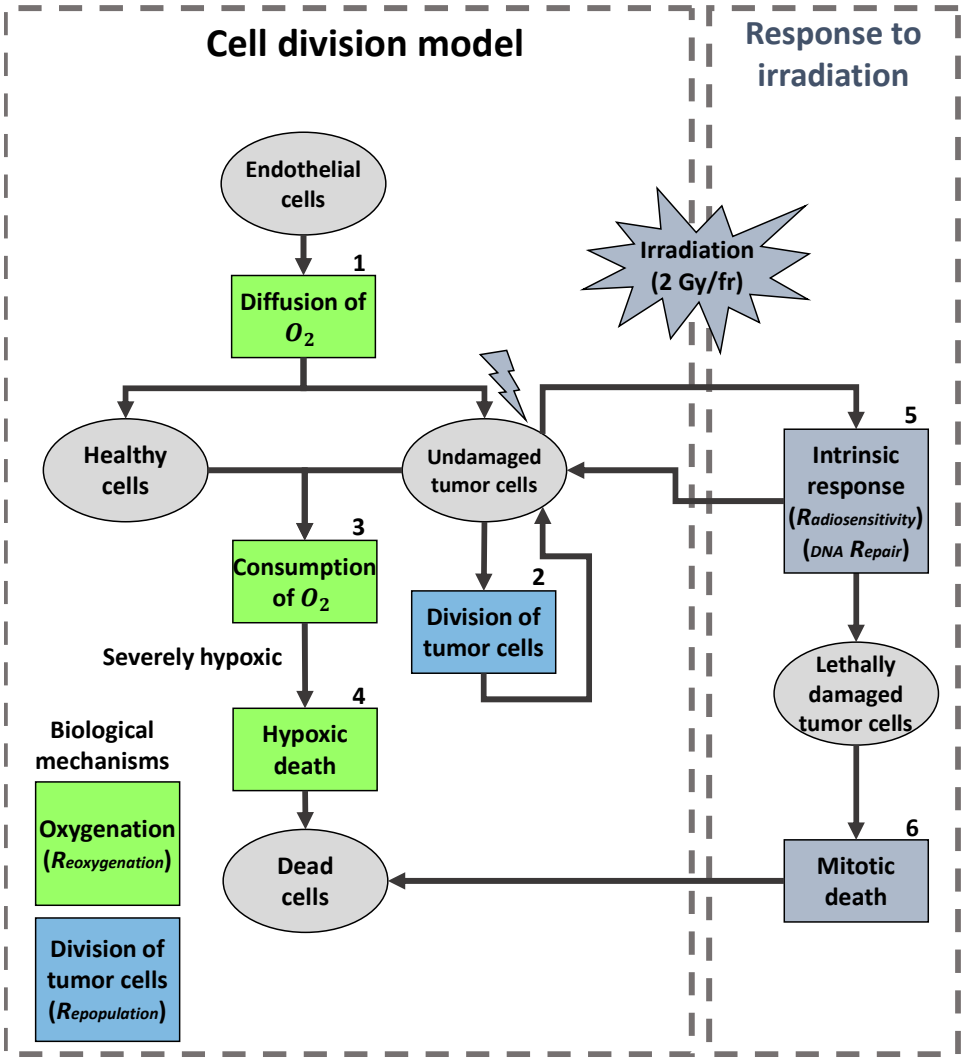

Figure 4.9 – Functional diagram of the reduced model. The different types of cells are represented with a gray ellipse. The different mechanisms are represented with a rectangle. The same color code as in Table 4.1 is used. Correspondences to the 5 R's are indicated in italics. Endothelial cells diffuse O_2 (1). Tumour cells divide (2). Healthy and tumour cells consume O_2 (3). As a result, if the O_2 levels are extremely low, they become severely hypoxic, which provokes their death (4). According to their intrinsic response to radiation (5), tumour cells irradiated with a dose of 2 Gy per fraction resume their division, if their DNA can be repaired, or die at the next mitosis (mitotic death) (6), if the damage caused by irradiation is lethal.

area and average ADC and T2w values (AUC = 0.75 ± 0.03). Furthermore, no major difference could be found between predictions made from the output of the comprehensive and the reduced versions of the model.

4.4 Discussion

The developed comprehensive model of tumour response to irradiation included the most relevant radiobiological mechanisms, which have been considered separately in previous multiscale approaches of the literature [31–34]. In particular, this is the first model simultaneously integrating, to our knowledge, mitotic catastrophe and cell cycle distribution, including checkpoints between phases G1/S and G2/M and a quiescence phase G0 affecting the radiosensitivity of tumour cells. This singularity offers a more realistic response to irradiation and opens doors to simulations considering cell cycle inhibitors or synchronisers [130]. In addition, this work introduced a novel approach of modelling angiogenesis, based on

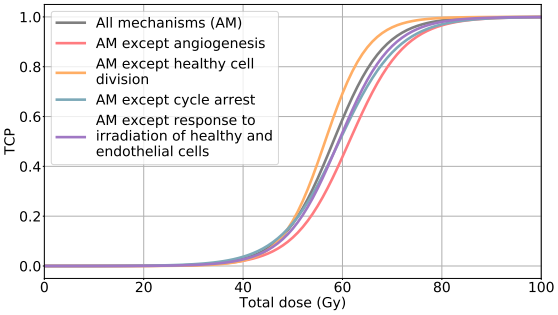

(a)

a (Gy^{-1})	b (Gy)	Δ_a (Gy^{-1})	Δ_b (Gy)	Δ_a^{rel} (%)	Δ_b^{rel} (%)
0.194	58.16	0	0	0	0
0.180	61.38	-0.014	3.22	-7.22	5.54
0.232	56.50	0.038	-1.66	19.59	-2.85
0.168	59.35	-0.026	1.19	-13.40	2.05
0.187	59.23	-0.007	1.07	-3.61	1.84

(b)

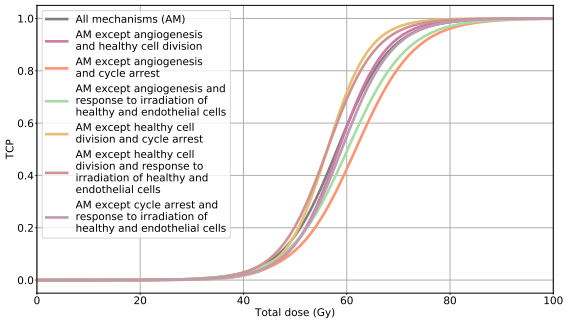

(c)

a (Gy^{-1})	b (Gy)	Δ_a (Gy^{-1})	Δ_b (Gy)	Δ_a^{rel} (%)	Δ_b^{rel} (%)
0.194	58.16	0	0	0	0
0.218	58.44	0.024	0.28	12.37	0.48
0.176	61.73	-0.018	3.57	-9.28	6.14
0.176	60.18	-0.018	2.02	-9.28	3.47
0.249	56.26	0.055	-1.90	28.35	-3.27
0.216	56.26	0.022	-1.90	11.34	-3.27
0.200	59.03	0.006	0.87	3.09	1.50

(d)

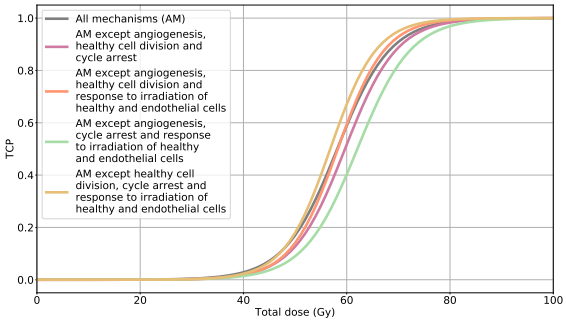

(e)

a (Gy^{-1})	b (Gy)	Δ_a (Gy^{-1})	Δ_b (Gy)	Δ_a^{rel} (%)	Δ_b^{rel} (%)
0.194	58.16	0	0	0	0
0.200	59.66	0.006	1.50	3.09	2.58
0.219	58.27	0.025	0.11	12.89	0.19
0.192	62.06	-0.002	3.90	-1.03	6.71
0.223	56.81	0.029	-1.35	14.95	-2.32

(f)

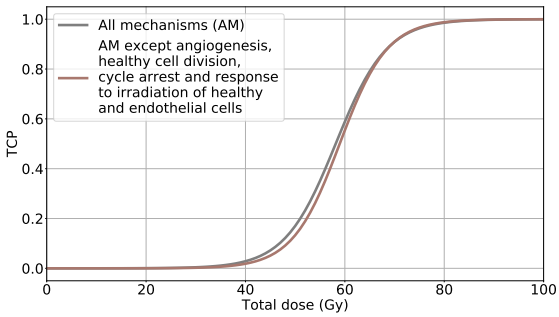

a (Gy^{-1})	b (Gy)	Δ_a (Gy^{-1})	Δ_b (Gy)	Δ_a^{rel} (%)	Δ_b^{rel} (%)
0.194	58.16	0	0	0	0
0.209	58.96	0.015	0.80	7.73	1.38

(g) (h)

Figure 4.9 – TCP curves excluding (a) 1, (c) 2, (e) 3 and (g) 4 mechanisms or sub-mechanisms and corresponding (b), (d), (f) and (h) constants a and b of the sigmoid functions fitting every TCP curve and absolute and relative differences with respect to the version considering all mechanisms (AM), defined as $\Delta_a = a - a_{AM}$, $\Delta_b = b - b_{AM}$, $\Delta_a^{rel} = \frac{\Delta_a}{a_{AM}}$ and $\Delta_b^{rel} = \frac{\Delta_b}{b_{AM}}$. A 2 Gy fractionation from Monday to Friday was simulated. The reference parameter values presented in Table 4.1 were considered. A total of 210 simulations (10 repetitions × 21 computational tissues) were performed to build each TCP curve. The same color code as in Table 4.1 is used.

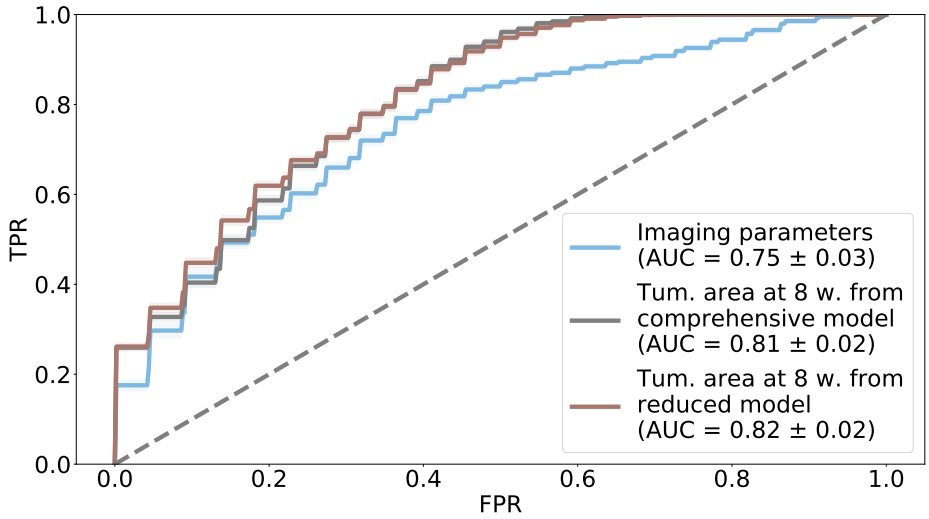

Figure 4.10 – ROC curves of biochemical recurrence predictions based on the maximal tumour area and average ADC and T2w values observed before treatment (blue) and the tumour area at $t = 8$ weeks outputs given by the comprehensive (gray) and reduced (brown) *in silico* models. Mean AUC values are indicated.

the calculation of dynamic VEGF distributions using a reaction-diffusion equation. Dynamic pO_2 maps were obtained, as in the works of Espinoza *et al.* [91] and others [39, 131], using partial differential equations. The stochastic intrinsic radiosensitivity of tumour, endothelial and healthy cells was given by the linear-quadratic formalism, adjusted to consider the influence of O_2, as in[31–34, 39, 89].

The complexity of the model lay, thus, in the integration of all these different mathematical for-

malisms, including stochastic and deterministic, as well as continuous and discrete approaches using a single computational framework based on M2SL. Furthermore, it must be remarked that the considered radiobiological mechanisms take place at different timescales. Tumour, healthy and endothelial cell division and response to irradiation were simulated with a time-step in the order of hours while oxygenation and VEGF diffusion and consumption are much faster processes happening at the scale of milliseconds. M2SL provided the tools to couple all the simulations at adapted frequencies without unnecessary computational burden.

The described model allowed *in silico* simulations of a complete radiotherapy protocol (40×2 Gy). The obtained oxygenation maps (Fig. 4.4) showed that cells situated in the poorly vascularised tumour core presented low pO_2 values. As O_2 diffusion is limited to a certain range, vessels located in the tumour rim could not fully oxygenate too distant cells situated in the central region, which therefore developed hypoxia and, in severe cases, necrosis. Consequently, since VEGF is emitted by hypoxic cells, a higher concentration of this protein was found in the tumour core. All these results are in line with the literature consensus [29, 132, 133].

Furthermore, TCP curves could be obtained. It must be noticed that the tumour was supposed to be controlled when there were not any undamaged tumour cells in the tissue. This consideration might prove to be too strict in clinical cases as the immune system, which was not integrated in the model, may be capable of destroying small quantities of tumour cells remaining after a radiotherapy treatment, assuring tumour control [121].

As far as we can tell, this is the first work presenting the results of an exhaustive sensitivity analysis (71400 simulations) of an integrative *in silico* model of tumour response to irradiation. Other studies of the literature [31, 32, 39] have only performed partial approaches to individually evaluate the impact of certain mechanisms or parameters. Those one-at-a-time analysis provide a preliminary view of the effect of a given factor with very few evaluations of the model. However, they prove to be insufficient and their results must be taken cautiously since these approaches cannot detect interactions between parameters. The Morris screening method used in this work provided qualitative information about the effect of the 33 parameters, including their interactions. This made it possible to rank, for the first time to our knowledge, all the parameters of an integrative model of tumour response to radiotherapy in order of importance. These results allowed to better assess the importance of the different radiobiological mechanisms and were used to reduce the dimension of the comprehensive model. Numerous examples of model reduction based on sensitivity analysis can be found in the biomedical literature [36, 93, 94].

Prostate histological cuts from 7 patients were used to initialise computational tissues for the sensitivity analysis and the model reduction simulations. These represent a large variability of tumour configurations. Results presented in this work are thus based on realistic tumour and vascular architectures.

The duration of the tumour cell cycle, T_{tum}, was identified as the parameter having the highest impact on tumour density at $t = 12$ weeks and its integral. This is in agreement with previous partial results of the literature. Harting *et al.* [39] also noted that the mechanism of division of tumour cells had an important effect on TCP. Espinoza *et al.* [32] explored the effect of different values of the doubling time of tumour cells. This parameter, comparable to the T_{tum} of our model, was found to have a significant influence on tumour cell density. Furthermore, the impact was higher when the value was decreased, which resulted in an increased division of tumour cells. All this is in consonance with results presented

in our Fig. 4.7a in the form of TCP curves.

The impact of T_{tum} can be interpreted as the sum of 2 contributions that apparently affect tumour density in opposite directions. On the one hand, it has an obvious effect on the proliferation of tumour cells. A low value of T_{tum} results in a fast division of this kind of cells. On the other hand, as tumour cells die by mitotic catastrophe, T_{tum} also impacts on their response to irradiation. A low value provokes a slow destruction of tumour cells.

Our parameters of dynamic oxygenation also had a significant effect on the studied outputs. In particular, hypoxic death had a great impact on tumour control. It can be suggested that, when this mechanism was not considered ($pO_2^{nec} = 0$ mmHg), extremely hypoxic cells, which are very radioresistant, did not die due to this lack of oxygen but had to be killed by irradiation, therefore at the expense of tumour control. The importance of oxygenation on tumour control was already illustrated by TCP curves presented by Harting *et al.* and Paul-Gilloteaux *et al.* [31].

In contrast, angiogenesis parameters had a negligible effect on both tumour density at $t = 12$ weeks and its integral. When the whole angiogenesis mechanism was excluded, tumour was slightly more difficult to control. It can be hypothesised that the tissue was less oxygenated and, consequently, more radioresistant. However, the difference was not enormous. On this matter, Espinoza *et al.* showed that versions of their model considering an increased angiogenesis or no angiogenesis at all presented no significant differences in terms of tumour density.

The duration of the healthy cell cycle, T_{heal}, also had a negligible effect on the tumour density at $t = 12$ weeks and its integral. When the whole mechanism was not considered, tumour control was slightly easier to achieve. It can be suggested that, in this case, the tissue contained more dead cells, which did not consume O_2. Consequently, it was better oxygenated and, therefore somewhat less radioresistant. Nevertheless, the difference was not substantial. This is in agreement with the results of Espinoza *et al.* The analogous mechanism of resorption of dead tumour cells of their model was found to have no influence on tumour density.

The impact on tumour control of the 3 radiobiological mechanisms retained in the reduced model (oxygenation, division of tumour cells and their response to irradiation) has been largely reported in the literature [21–26]. In particular, the relationship between hypoxia and tumour response to irradiation has been widely discussed [117, 132, 134, 135]. Hypoxic regions, situated at a certain distance from blood vessels, are known to be more resistant to irradiation that well-oxygenated areas. To consider this heterogeneity, in this work, as in most of the previous *in silico* models [32, 39], we included, at the cell scale, the oxygen enhancement ratio (OER). This factor establishes a relation between the doses administered under hypoxic and aerobic conditions producing the same biological effect [29]. It can be expressed in alternative ways [31, 33, 34, 89].

Biochemical recurrence predictions made with the tumour area at $t = 8$ weeks output of the comprehensive and the reduced versions of the model significantly improved those based on pre-treatment imaging parameters. These results show a potential application of the model as a useful tool in a clinical context. In addition, they corroborate the equivalence of the comprehensive and the reduced model, already suggested by the sensitivity analysis and demonstrated in terms of TCP curves, as no major difference was observed between the predictions made from the outputs of the 2 versions.

It must be remarked that this preliminary validation was performed taking the intermediate reference

values of Table 4.1 for every parameter of the model, except for the highly influential hypoxic death threshold, pO_2^{nec}. Future model calibration, especially of the other parameters having an important impact on tumour area at $t = 8$ weeks, should improve the quality of the predictions. Furthermore, an initial vascular density of 3.8% [31] was supposed for the 76 virtual tissues. Individual values for each sample deduced from PET images, may also lead to better biochemical recurrence predictions, as the sensitivity analysis showed that oxygenation parameters had an important impact on tumour regression.

As a first step, the presented results were obtained considering only a dose per fraction of 2 Gy, typically applied in prostate cancer. However, the flexible implementation of the model with MS2L will allow to simulate hypo-and-hyperfractionated treatments [7, 125, 136, 137] in the future. Using optimisation algorithms [138, 139], the total dose, the dose per fraction and the interval between sessions maximising tumour control will be identified.

This work presents several limitations which will be tackled in the future. Firstly, the comprehensive model intended to integrate the most relevant biological mechanisms of the literature, in particular those described by the 5 R's [17]. Nevertheless, some mechanisms which may also play a role on tumour regression, such as the immune response [121], were not included as only short-term evolution was considered. Furthermore, it must be remarked that the linear-quadratic equation, almost universally used to model the response to irradiation, may not be valid for every value of dose per fraction. The applicability of this formalism to high doses (more than 6 Gy) remains controversial [140].

Secondly, it must be borne in mind that the validity of the conclusions of the sensitivity analysis can only be guaranteed within the studied prostate-specific limit values of the parameters. The definition of appropriate ranges is, thus, a key aspect of the Morris method. Due to ethical or technical reasons, the vast majority of the parameters of cancer models have never been measured *in vivo* and, for many of them, a panoply of *in vitro* values exists [31, 32, 91, 104, 118, 125, 126]. Ranges in this work were defined from maximum and minimum values of the literature and our radiobiological expertise. This should assure the significance of the obtained results. Nevertheless, to complement this approach, a more precise, but also more computationally expensive, sensitivity analysis using, for example, the Sobol method will be performed in the future on the reduced model, including only the most relevant parameters identified by the Morris analysis.

Thirdly, the results of the first validation of the model at the population scale need to be corroborated on an external cohort including a larger number of patients. Furthermore, although each mechanism has been previously considered in the literature, the model should still be validated at the microscopic and macroscopic scales. Several options to cope with this issue may be considered. Time-lapse imaging of prostate tumour cells cultured *in vitro* and irradiated with different fraction schedules can be used to carry out a rough validation of tumour cells division and response to irradiation at the microscopic scale. Cells can be tracked using detection strategies [141]. Nevertheless, a cell-based approach presents several limitations, the most important being the lack of consideration of realistic tumour microenvironment. At a macroscopic scale, several mechanisms can also be validated. Using longitudinal mpMRI [142], CBCT [89] and PET images [34] of irradiated patients, tumour volumes and cell densities can be obtained and compared with the results of *in silico* simulations. Additionally, PET images can be used to validate the oxygenation of the tissue [143, 144].

4.5 Conclusion

An original multiscale *in silico* model of tumour response to radiotherapy (33 parameters) integrating 5 radiobiological mechanisms (oxygenation, division of tumour cells, angiogenesis, division of healthy cells and phase-and-oxygen-dependent response to irradiation, considering cycle arrest and mitotic catastrophe) was developed. A thorough sensitivity analysis (71400 simulations) using the Morris method, applied for the first time to a whole integrative model of tumour response to radiotherapy, allowed to obtain a reduced version (18 parameters), equivalent in terms of tumour control probability and biochemical recurrence prediction. This simplified model included only 3 radiobiological mechanisms: oxygenation, given by a reaction-diffusion equation, division of tumour cells, considering their cycle, and cycle-phase-and-oxygen-dependent response to irradiation of tumour cells, based on the linear-quadratic formalism. Biochemical recurrence predictions obtained with the reduced model were significantly better than those performed from pre-treatment imaging parameters. The reduced model should still be thoroughly validated at the microscopic and macroscopic scales using experimental data. Other radiobiological mechanisms, such as the radio-induced tissue inflammation provoking neovascularisation and immune cell recruitment, should be explored and potentially integrated. In the future, the model will be used to simulate different radiotherapy fractionation schedules (hypo/hyper fractionation), paving the way for the clinical optimisation of patient-specific treatments.

In this chapter, an original reduced mechanistic model of tumour growth and response to radiotherapy was developed. After an exhaustive sensitivity analysis, it integrates only three radiobiological mechanisms: oxygenation, the division of tumour cells and their response to irradiation. It is equivalent in terms of TCP and tumour cell density to a comprehensive version integrating the main radiobiological mechanisms of the literature.

To demonstrate the clinical usefulness of our model, a first prediction of biochemical recurrence after EBRT was performed on a cohort of 76 localised prostate cancer patients using the tumour area after treatment obtained through simulation. This prediction was significantly better than those performed directly from pre-treatment mpMRI parameters This clinical application of our reduced model will be fully explored in the next chapter.

Chapter 5

Mechanistic simulation of tumour response outperforms radiomics predicting recurrence in prostate cancer radiotherapy

---

In this chapter, our reduced mechanistic *in silico* model of tumour growth and response to irradiation was used to predict biochemical recurrence in the context of prostate cancer. Digital tissues, representing 76 patients with localised prostate adenocarcinoma having undergone EBRT, were built from pre-treatment MRI. The prescribed irradiation protocols were simulated using the mechanistic model. Logistic regression was then performed to predict recurrence directly from MRI features following a conventional radiomics approach and from different outputs given by the mechanistic model.

The content of this chapter has been presented at the international conference IEEE ISBI 2021, in the form of peer-reviewed 4-page paper and oral communication.

C. Sosa-Marrero, P. Fontaine, E. Mylona, K. Gnep, A. Hernández, F. Paris, R. de Crevoisier and O. Acosta, «Mechanistic simulation of tumour response outperforms radiomics predicting recurrence in prostate cancer radiotherapy», in *IEEE ISBI 2021*, pp. 1-4, 2021. (Oral communication)

5.1 Introduction

Radiomics approaches based on imaging biomarkers [76, 77] have emerged over the last few years as appealing tools to predict tumour recurrence and survival [12–14]. Nevertheless, their performance is still limited in terms of prediction scores (e. g. AUC, C-index). Furthermore, they require a large amount of population data in order to be statistically significant and they are usually based on complex machine learning methods, which raises the question of interpretability. In addition, radiomics-based studies are frequently confronted with the class imbalanced problem, i.e. most of the individuals of the cohort belong to the majority class and only a few of them constitute the complimentary minority class. This phenomenon is particularly evident in the context of the present work.

As opposed to these data-driven techniques, mechanistic modelling appears as a groundbreaking approach based on the integration of the different biological mechanisms underlying the behavior of a given clinical endpoint. Through *in silico* simulation, they allow to better comprehend the response of patients to a certain treatment and their results are easily explainable. Their predictive capabilities have already been shown in other contexts [15, 16].

The objective of the present work was thus to predict biochemical recurrence using our reduced mechanistic *in silico* model of tumour growth and response to radiotherapy [145] in the context of prostate cancer. It integrates the most relevant radiobiological mechanisms, identified by the Morris sensitivity analysis: oxygenation, division of tumour cells and their response to irradiation. It allows to create digital patients from pre-treatment mpMRI scans, representing real individuals, on which different irradiation protocols can be simulated *in silico*. Its predictive capabilities were compared to those of a radiomics workflow using mpMRI features and oversampling techniques.

5.2 Material and methods

5.2.1 Population dataset

A cohort of 76 patients with peripheral zone localised prostate adenocarcinoma having undergone EBRT [12] was used for this study. Prior to the beginning of treatment, 3 T MRI was performed. Sequences, fully described in [12], included axial turbo spin echo T2-w and axial diffusion using multiple b-values. Apparent diffusion coefficient (ADC) maps were calculated. Patients were followed up by means of clinical examination and PSA analysis every 6 months for 5 years after the end of irradiation. Nine patients suffered biochemical recurrence, defined according to the Phoenix criteria [128] Our Institutional Review Board approved this retrospective study.

5.2.2 Experimental design

The experimental design (depicted in Fig. 5.1) consisted of the following steps:

– *Step 0: Tumour segmentation.* In previous work [12], tumours had been manually segmented on pre-treatment T2-w sequences and contours propagated onto the corregistered ADC images.

– *Step 1: Feature extraction.* Tumour volume and average T2-w and ADC were calculated from the corresponding images.

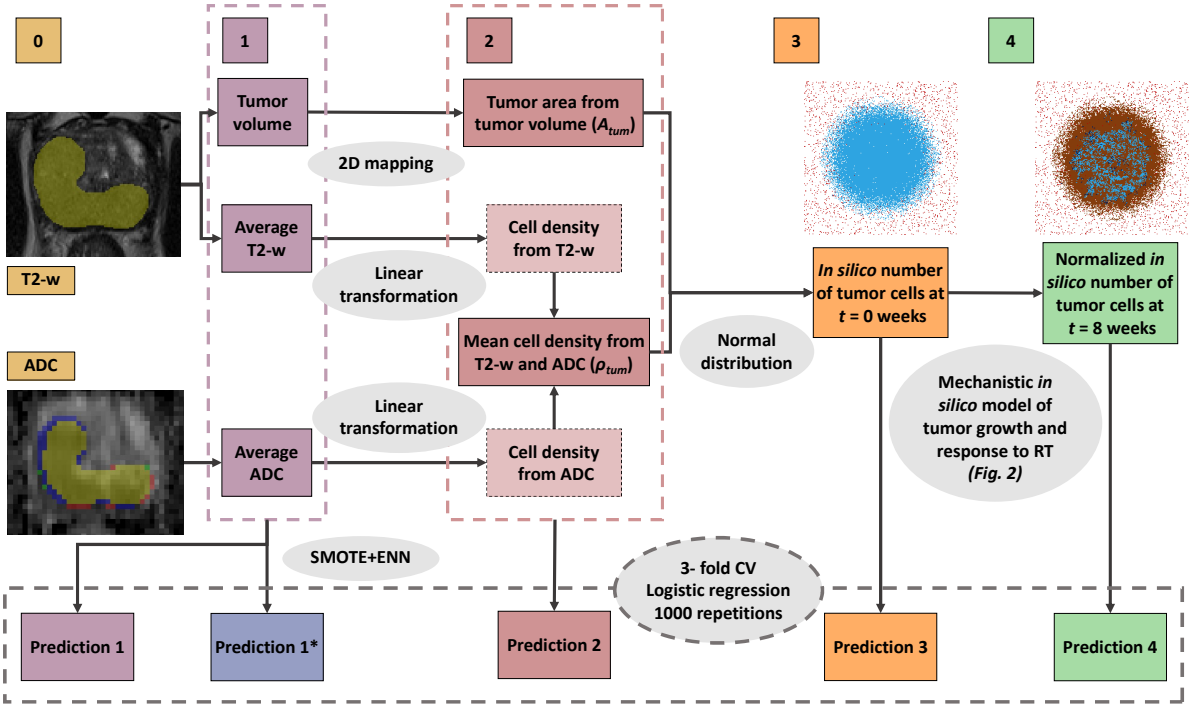

Figure 5.1 – Workflow. Tumour segmentation (0). Feature extraction (1). Digital tissue characterization (2). Digital tissue initialization (3). *In silico* simulation (4). At every step, biochemical recurrence was predicted using 3-fold cross-validation logistic regression.

– *Step 2: Digital tissue characterization.* In order to simulate tumour response to radiotherapy with our mechanistic model, 76 2D digital tissues representing the 76 patients of the cohort were characterised. Every tumour was mapped to an equivalent spherical volume. Then, the area of its great circle, A_{tum}, [31] was calculated. In addition, 2 cell density measures were obtained from the corresponding average T2-w and ADC through a linear transformation [129]. The mean density value, ρ_{tum}, was then calculated.

– *Step 3: Digital tissue initialization.* The 76 digital tissues were initialised using the corresponding 2 input parameters previously obtained: A_{tum} and ρ_{tum}. A fraction ρ_{tum} of a disk of area A_{tum} was initialised with tumour cells. They were placed following a normal distribution around the centre of the disk taking $\sigma = 0.33$. An initial prostate-specific vascular density of 3.8% [31] was taken for every digital tissue. Endothelial cells were supposed to be randomly distributed forming a poorly-vascularised tumour core.

– *Step 4: In silico simulation.* The radiotherapy protocol administered to each patient of the cohort (total dose of 74 - 80 Gy delivered in 2 Gy fractions from Monday to Friday) was simulated on the corresponding digital tissue and the evolution of the number of tumour cells throughout the 8 weeks of treatment was obtained. For the sake of interpatient comparison, numbers of tumour cells were normalised by their initial values (at $t = 0$ weeks). Model parameters were manually calibrated considering prostate-specific ranges reported in the literature [125, 126]. Given its stochastic component, each simulation was repeated 5 times and the mean output was taken.

At each step, the logistic model (stratified 3-fold cross-validation, 1000 repetitions) was used to predict biochemical recurrence. "Prediction 1" was made from the 3 pre-treatment imaging parameters, namely tumour volume and average T2-w and ADC. It was set as a baseline. "Prediction 1*" was performed from the same MRI features after oversampling the dataset with the SMOTE+ENN technique to obtain a minority-majority ratio of 1:2. "Prediction 2" was based on the calculated tumour area and mean cell density. "Prediction 3" was made from the number of tumour cells in the digital tissue before the start of simulation, at $t = 0$ weeks. "Prediction 4" was performed using the normalised number of tumour cells at the end of treatment ($t = 8$ weeks) provided by the mechanistic model.

5.2.3 Mechanistic *in silico* model

To simulate the irradiation protocols administered to each patient, our previously developed mechanistic *in silico* model of tumour growth and response to radiotherapy [145] was used. As described in chapter 4, it considers a digital tissue in which each pixel corresponds to a healthy, tumour, endothelial or dead cell. It integrates 3 major radiobiological mechanisms: oxygenation, division of tumour cells and their response to irradiation (Fig. 5.2). A sensitivity analysis using the Morris screening method performed on 21 digital tissues, built from prostate histological cuts, showed that parameters characterizing these mechanisms had a high impact on tumour regression [145]. Dynamic oxygenation is given by a reaction-diffusion equation. Endothelial cells have a fixed O_2 value and diffusion is considered isotropic. Hypoxic stress is included. The cycle of tumour cells, composed of the 4 classical phases G1, S, G2 and M and a quiescent state G0, is implemented to model their division. The response to irradiation is based on the linear-quadratic formalism [41]. Radiosensitivity depends on the oxygenation levels and the cycle phase. Mitotic catastrophe is integrated.

5.3 Results and discussion

Results of the simulations using the mechanistic model are shown in Fig. 5.3. Mean curves of the evolution of the normalised *in silico* number of tumour cells are presented for patients with and without biochemical recurrence. Interpatient standard deviations are indicated. It was shown that the tumour cell reduction during the course of the treatment was higher for patients who did not suffer biochemical recurrence. Differences between the 2 curves were significant (p-value ≤ 0.001, given by a Mann-Whitney U test) since week 4, demonstrating the efficiency of the proposed mechanistic model. Particularly, a p-value ≤ 0.0005 was obtained at $t = 8$ weeks.

Results of the biochemical recurrence predictions are presented in Fig. 5.4. "Prediction 4", based on the normalised *in silico* number of tumour cells at $t = 8$ weeks, was significantly better (p-value ≤ 0.0001, given by a Wilcoxon signed-rank test) than predictions "1" and "1*", performed directly from pre-treatment imaging parameters without and with oversampling: median AUC = 0.85 vs. AUC = 0.77 and 0.80, respectively. Median AUC values of 0.81 and 0.82 were obtained for the intermediate predictions "2" and "3", based on the calculated tumour area and mean cell density and the number of tumour cells on the digital tissue before simulation, respectively.

These results show the potential of our mechanistic model of tumour growth and response to radio-

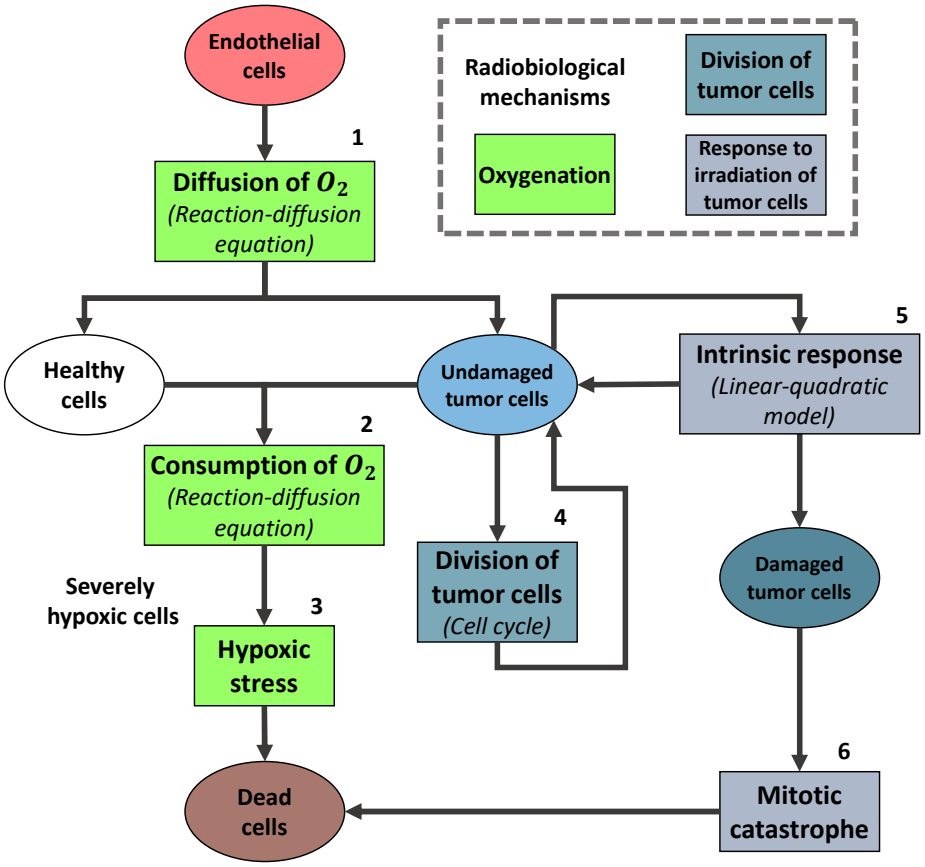

Figure 5.2 – Functional diagram of the mechanistic *in silico* model of tumour growth and response to radiotherapy. The different types of simulated cells are represented with an ellipse. The different mechanisms are represented with a rectangle. Endothelial cells diffuse O_2 (1). Healthy and tumour cells consume O_2 (2). As a result, if the O_2 levels are extremely low, they become severely hypoxic, which provokes their death (3). Tumour cells divide (4). According to their intrinsic response to radiation (5), irradiated tumour cells resume their division, if their DNA can be repaired, or die at the next mitosis (6), if the damage caused by irradiation is lethal.

therapy as a robust tool to predict recurrence in prostate cancer. By simulating the prescribed irradiation protocol on virtual tissues representing the 76 patients of the cohort, we obtained an easily-explainable marker of biochemical failure (the number of tumour cells at the end of treatment). It can be readily inferred from the results of the logistic regression that a great number of tumour cells at $t = 8$ weeks resulted in a high probability of suffering recurrence. This intuitive explanation contrasts with the difficulties frequently experienced when interpreting the results of radiomics approaches of the literature, in which complex machine learning methods are often used as black boxes and fed with hundreds of imaging parameters, whose clinical significance is not always clear.

The use of SMOTE+ENN to oversample the cohort resulted in an improvement in predictions from MRI features. However, performance was still limited. Indeed, the median AUC value of "Prediction 1*" was similar to the one obtained for "Prediction 2", which required no oversampling. Furthermore, it

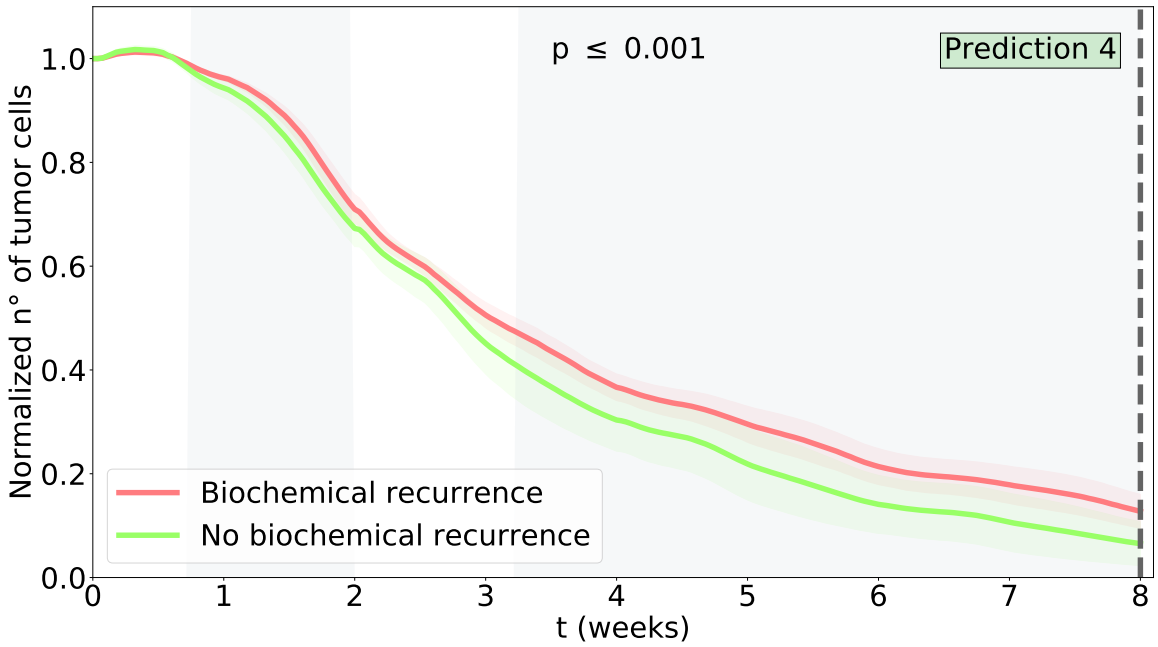

Figure 5.3 – Evolution of the number of tumour cells throughout simulation, normalised by the initial value, for the 2 groups of patients, with and without recurrence (red and green, respectively). Differences between the 2 curves were significant (p-value ≤ 0.001) in the gray area. "Prediction 4" was made from values at $t = 8$ weeks.

must be noted that the use of this technique adds considerable complexity to the process, which reduces explainability and entails computational burden.

Due to its interpretability and robustness, the logistic model was chosen for this study. Only 3 parameters significantly associated with biochemical recurrence [12] and clinically meaningful (tumour volume and average T2-w and ADC) were considered. Other classifiers frequently used in the medical context such as random forests or support-vector machines, considering a wider range of radiomic features, or ensemble methods could be explored for the baseline "Prediction 1". However, their results would be less explainable from a clinical point of view.

This study presents several limitations that are going to be addressed in future work. Firstly, the results need to be corroborated on an external cohort including a larger number of patients. Secondly, it has been widely reported in the literature that oxygenation has a crucial impact on biochemical recurrence [18, 146], which was confirmed by our previous sensitivity analysis [145]. However, in this work, a single average prostate-specific vascular density [31] was considered for every digital tissue. In future work, individual values may be deduced from MR-DCE images.

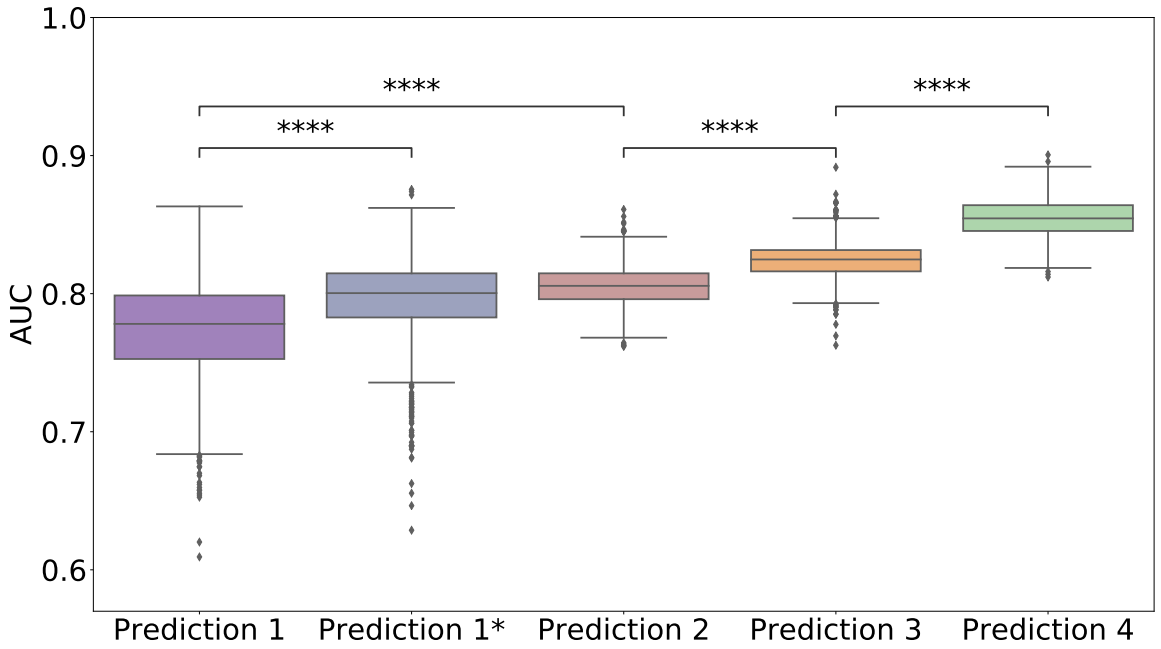

Figure 5.4 – AUC. Same color code as in Fig. 5.1 is used. "Prediction 1" is represented in purple; "prediction 1*", in blue; "prediction 2", in red; "prediction 3", in orange, and "prediction 4", in green.

5.4 Conclusion

Biochemical recurrence prediction based on the output of our mechanistic *in silico* model of tumour growth and response to radiotherapy was significantly better (p-value ≤ 0.0001) than those made directly from pre-treatment imaging parameters (AUC = 0.85 vs. AUC = 0.77, respectively), even when the original dataset was oversampled (in this case, AUC = 0.80 was obtained from MRI features). These results reinforce the potential of digital patients to perform personalised predictions based on the mechanistic understanding of tumour response to radiotherapy.

In this chapter, our reduced mechanistic model was used to predict biochemical recurrence in the context of prostate cancer EBRT and results were compared with a conventional radiomics approach. Significantly better biochemical recurrence predictions in terms of AUC were obtained when using simulation-based markers.

The next and final chapter presents a general discussions on the main contributions and limitations of this thesis. Suggestions about future work on the prediction of biochemical recurrence using our mechanistic model are also offered.

Part IV

Conclusion

Chapter 6

Conclusion

6.1 Overview

This thesis aimed to better comprehend, through *in silico* simulation, the tumour response to EBRT in the context of prostate cancer. For this purpose, as a first step, the model of Espinoza *et al.* was adapted and used to simulate conventional and hypofractionated prostate irradiation schedules, as described in part II of this document. This adaptation considered 4 radiobiological mechanisms: static oxygenation, modelled with a reaction-diffusion equation; proliferation of tumour cells, based on a proliferation factor; oxygen-dependent response to irradiation, considering the LQM, and resorption of dead cells, given by a resorption constant. The OAT local sensitivity analysis performed on this adapted model showed that the oxygen-diffusion factors and the intrinsic radiosensitivity parameter of the LQM α had the most important effect on tumour cell survival right after EBRT. The pO_2 distributions obtained after simulation were inline with prostate clinical values from the literature. *In silico* total doses to achieve tumour control within the clinical ranges were obtained for conventional and hypofractionated prostate irradiation schedules.

Nevertheless, this approach presented several limitations, mainly due to the implementation of the model in the simulation software Netlogo. Some radiobiological mechanisms which may play a major role in tumour control, such as the cell cycle distribution, mitotic catastrophe or angiogenesis resulting in the reoxygenation of the tissue, were not integrated. In addition, only a 2D configuration could be considered. Furthermore, the OAT local sensitivity analysis performed in this part of the thesis had to be taken cautiously. It did not fully explore the parameter space and could not detect interactions and non-linear effects.

For these reasons, as described in part III of this document, an original mechanistic *in silico* model of tumour response to EBRT was developed. It was implemented in C++ using the in-house simulation library M2SL and both 2D and 3D configurations could be considered. It integrated 5 radiobiological mechanisms: dynamic oxygenation, modelled with a reaction-diffusion equation and including hypoxic death; division of tumour cells, considering their cell-cycle, VEGF-driven angiogenesis, given by a reaction-diffusion equation; division of healthy cells and cell-cycle-phase-and-oxygen-dependent response to irradiation, based on the LQM and considering cycle arrest and mitotic catastrophe. A thorough sensitivity analysis (71400 simulations) using the Morris screening method, was performed for the first time to a whole integrative model of tumour response to radiotherapy. It showed that the duration of the cycle of tumour cell cycle, the radiosensitivity parameters of tumour cells in the phases G1 (α_{tumG1}) and G2 (α_{tumG2}) and the hypoxic death threshold had the most important effect on tumour cell density 12 weeks after the beginning of the treatment and its integral over time. In contrast, parameters associated with angiogenesis the division of healthy cells and the response to irradiation of healthy and endothelial cells

had a negligible impact. TCP curves of the comprehensive model and 15 simplified version excluding certain mechanisms were compared. Based on these results, a reduced version, equivalent in terms of tumour cell density and TCP, was proposed. This simplified model included only 3 radiobiological mechanisms: oxygenation, given by a reaction-diffusion equation, division of tumour cells, considering their cycle, and cell-cycle-phase-and-oxygen-dependent response to irradiation of tumour cells, based on the LQM.

This original reduced model was used to predict biochemical recurrence in a cohort of 76 patients with localised prostate adenocarninoma having undergone EBRT. For this purpose, 2D digital tissues representing the individuals of the cohort were built from pre-treatment mpMRI features. Then, the radiotherapy protocol administered to each patient was simulated on the corresponding digital tissue and the evolution of the number of tumour cells throughout the 8 weeks of treatment was obtained. Logistic regression was performed to predict biochemical recurrence directly from pre-treatment mpMRI features or from the *in silico* number of tumour cells at the end of the treatment. Predictions obtained with the simulation-based marker were significantly better than those performed from pre-treatment imaging parameters in terms of AUC. These results reinforce the potential of digital patients to perform personalised predictions based on the mechanistic understanding of tumour response to EBRT.

6.2 Main contributions

The main contributions of this thesis were therefore:

1. the adaptation and comparison with prostate clinical data of an existing model of tumour response to irradiation
2. the development of an original mechanistic model of tumour growth and response to radiotherapy integrating the main radiobiological mechanisms of the literature
3. the identification of the radiobiological parameters and mechanisms having the most important impact on tumour cell density and TCP
4. the development of a reduced mechanistic model integrating only the most important radiobiological mechanisms
5. the generation of significantly better biochemical recurrence predictions using the reduced mechanistic model, compared to a conventional radiomics approach, in the context of prostate cancer EBRT

6.3 Limitations

This work presents however several limitations. Firstly, the original comprehensive model intended to integrate the most relevant biological mechanisms of the literature, in particular those described by the 5 R's [17]. Nevertheless, some mechanisms which may also play a role on tumour regression, such as the immune response [121], were not included as only short-term evolution was considered. Furthermore, it must be remarked that the LQM, almost universally used to model the response to irradiation, may not be valid for every value of dose per fraction. The applicability of this formalism to high doses (more than 6 Gy) remains controversial [140].

Secondly, it must be borne in mind that the validity of the conclusions of the Morris sensitivity analysis can only be guaranteed within the studied prostate-specific limit values of the parameters. The definition of appropriate ranges is, thus, a key aspect of the Morris method. Due to ethical or technical reasons, the vast majority of the parameters of cancer models have never been measured *in vivo* and, for many of them, a panoply of *in vitro* values exists [31, 32, 91, 104, 118, 125, 126]. Furthermore, the Morris screening analysis provided a rough view of the hierarchy of the parameters of the model. The Euclidean distance of each point to the origin on the plane μ^* vs. σ was calculated as an indicator of the impact of the parameter in question [37]. However, the effect was not precisely quantified and non-linear relations and interactions between parameters could not be distinguished.

Thirdly, the results of the first validation of the model in terms of biochemical recurrence prediction at the population scale need to be corroborated on an external cohort including a larger number of patients. Furthermore, and most importantly, although each mechanism has been previously considered in the literature, the model should still be thoroughly validated at the microscopic and macroscopic scales.

Finally, it has been widely reported in the literature that oxygenation has a crucial impact on biochemical recurrence [18, 146], which was confirmed by our local and Morris sensitivity analyses. However, in this work, every digital tissue used to predict biochemical recurrence was initialised considering a single average prostate-specific vascular density value. Furthermore, for the sake of simplicity and, especially, rapidity of the simulations, every tumour of the cohort was mapped to an analogous 2D disk where cells were placed following a normal distribution around its centre. However, the shape of tumours may also play a major role in tumour control. More realistic initial configurations may lead to better biochemical recurrence predictions. In addition, due to its interpretability and robustness, only logistic regression was performed in this study. Moreover, the most important parameters of the mechanistic model (duration of the cycle of tumour cells, α of tumour cells in phase G1 and hypoxic death threshold) were manually calibrated within the ranges of the literature to maximise AUC. For every other factor, intermediate values were taken. This rudimentary technique could not assure that optimal parameter values giving the best AUC were used.

6.4 Future work

The limitations of this work explained in the previous section could be tackled in the future as follows. To complement the results of the screening analysis, a more precise, but also more computationally expensive, sensitivity study using, for example, the Sobol method may be performed in the future on the reduced model, including only the most relevant parameters identified by the Morris analysis.

Furthermore, several options may be considered to validate the reduced model at the microscopic and macroscopic scales. Time-lapse imaging of prostate tumour cells cultured *in vitro* and irradiated with different fraction schedules can be used to carry out a rough validation of tumour cells division and response to irradiation at the microscopic scale. Cells can be tracked using detection strategies [141]. Nevertheless, a cell-based approach presents several limitations, the most important being the lack of consideration of realistic tumour microenvironment. High resolution bioprinting technologies allow to design and generate *in vitro* cell patterns [147] mimicking the structural organization of prostate tumours. An equivalent tumour and endothelial architecture can be generated to initialise the computational model.

Then, tumour growth and the response to different fractionations can be studied in the analogous *in vitro* and *in silico* tissues. Tumour and endothelial densities and even spatial disposition can be thus compared.

At a macroscopic scale, several mechanisms can also be validated. Using longitudinal mpMRI [142], CBCT [89] and PET images [34] of irradiated patients, tumour volumes and cell densities can be obtained and compared with the results of *in silico* simulations. Additionally, PET images can be used to validate the oxygenation of the tissue [143, 144]. The correspondence in terms of cell density between the microscopic level and *in vivo* mpMRI data at the macroscopic scale can be established using voxel-wise machine learning techniques as proposed by Sun *et al* [148].

Concerning the biochemical recurrence predictions, in future work, individual vascular densities for each digital tissue could be deduced from MR-DCE images. Furthermore, the construction of 3D avatars mimicking the shape of every tumour of the cohort is being explored (Fig. 6.1).

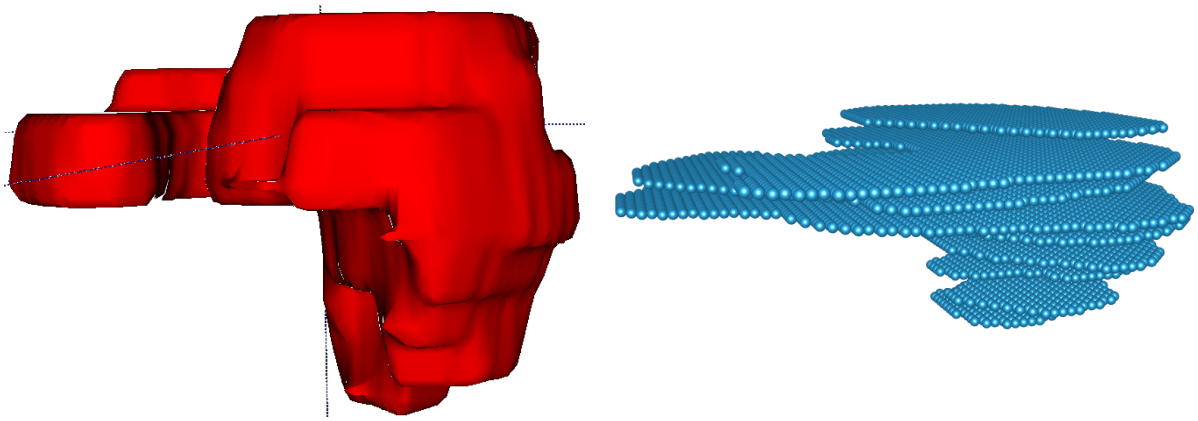

Figure 6.1 – Example of (a) tumour of the cohort and (b) corresponding 3D avatar at the beginning of simulations

In addition, other classifiers frequently used in the medical context such as random forests or support-vector machines or ensemble methods could be explored for the biochemical recurrence predictions. However, their results would be less explainable from a clinical point of view. Finally, the parameter values of the reduced model, at least for the most important factors, giving maximal AUC, could be identified using optimization algorithms [149].

In the long term, once the model is fully validated and calibrated, it may be used as a planning platform to simulate alternative irradiation schedules (such as hypofractionated treatments) for patients with the highest risks of biochemical failure. This work paves the way for the clinical optimisation of patient-specific therapies.

An overview of the thesis structure, indicating its main contributions and perspectives is depicted in Fig. 6.2.

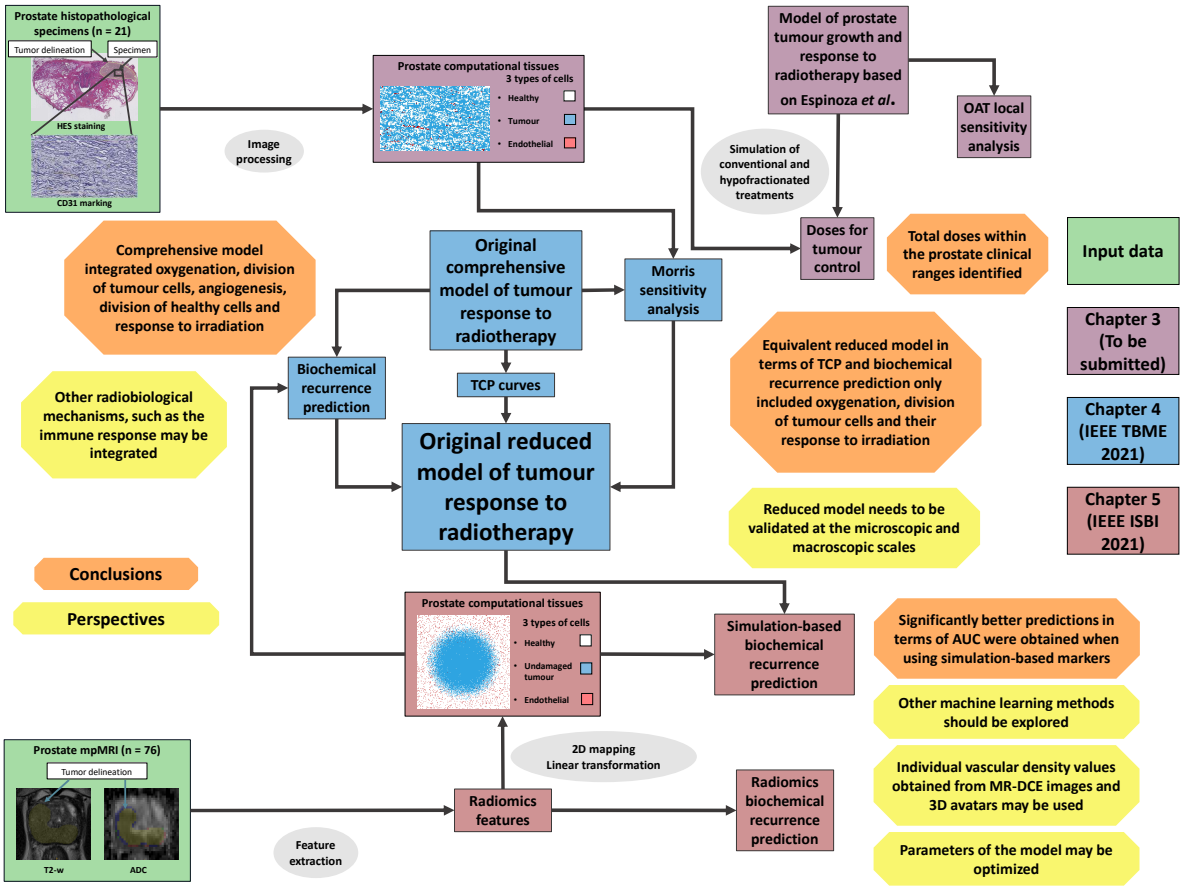

Figure 6.2 – Overview of the thesis structure, indicating the main contributions (in orange) and perspectives (in yellow)

LIST OF PUBLICATIONS

International journal papers

C. Sosa-Marrero, R. de Crevoisier, A. Hernández, P. Fontaine, N. Rioux-Leclercq, R. Mathieu, A. Fautrel, F. Paris and O. Acosta, «Towards a reduced *in silico* model predicting biochemical recurrence after radiotherapy in prostate cancer», *IEEE Trans. Biomed. Eng.*, **68**, pp. 2718-2729, 2021.

Peer-reviewed international conference papers

C. Sosa-Marrero, P. Fontaine, E. Mylona, K. Gnep, A. Hernández, F. Paris, R. de Crevoisier and O. Acosta, «Mechanistic simulation of tumour response outperforms radiomics predicting recurrence in prostate cancer radiotherapy», in *IEEE ISBI 2021*, pp. 1-4, 2021. (Oral communication)

C. Sosa-Marrero, O. Acosta, M. Castro, A. Hernández, N. Rioux-Leclercq, F. Paris and R. de Crevoisier, «Sensitivity analysis of an *in silico* model of tumour growth and radiation response», in *IEEE ISBI 2019*, pp. 1497-1500, 2019. (Oral communication)

Communications at international conferences

C. Sosa-Marrero, O. Acosta, M. Castro, A. Hernández, N. Rioux-Leclerq, F. Paris and R. de Crevoisier, «Sensitivity analysis of an *in silico* model of tumour growth and response to radiotherapy», *Radiother. Oncol.* **133**, S527-S528, 2019. (In ESTRO 38 as poster)

Communications at national conferences

C. Sosa-Marrero, O. Acosta, M. Castro, A. Hernández, N. Rioux-Leclercq, J. Castelli, F. Paris and R. de Crevoisier, «Modélisation/simulation de prolifération tumorale et de réponse à la radiothérapie», 30ème Congrès Société Française de Radiotherapie Oncologique (SFRO), 2019. (Poster)

C. Sosa-Marrero, O. Acosta, N. Rioux-Leclercq, R. Mathieu, N. Foray and R. de Crevoisier, «Simulation numérique de croissance tumorale et réponse à la radiothérapie», Journées Recherche en Imagerie et Technologies pour la Santé (RITS), 2019. (Oral communication)

BIBLIOGRAPHY

1. Bray, F. *et al.,* Global cancer statistics 2018: GLOBOCAN estimates of incidence and mortality worldwide for 36 cancers in 185 countries, *CA: A Cancer Journal for Clinicians* **68**, 394–424 (2018).
2. D'Amico, A. V. *et al.,* Biochemical Outcome After Radical Prostatectomy, External Beam Radiation Therapy, or Interstitial Radiation Therapy for Clinically Localized Prostate Cancer, *JAMA* **280**, 969–974 (1998).
3. De Vries, K. C. *et al.,* Hypofractionated Versus Conventionally Fractionated Radiation Therapy for Patients with Intermediate- or High-Risk, Localized, Prostate Cancer: 7-Year Outcomes From the Randomized, Multicenter, Open-Label, Phase 3 HYPRO Trial. eng, *Int. J. Radiat. Oncol. Biol. Phys.* **106**, 108–115 (2020).
4. Martin, J. M., Supiot, S., Keall, P. J. & Catton, C. N., Moderately hypofractionated prostate external-beam radiotherapy: an emerging standard. eng, *Brit. J. Radiol.* **91**, 20170807 (2018).
5. Bruner, D. W. *et al.,* Quality of Life in Patients With Low-Risk Prostate Cancer Treated With Hypofractionated vs Conventional Radiotherapy: A Phase 3 Randomized Clinical Trial. eng, *JAMA Oncol.* **5**, 664–670 (2019).
6. Catton, C. N. *et al.,* Randomized Trial of a Hypofractionated Radiation Regimen for the Treatment of Localized Prostate Cancer. eng, *J. Clin. Oncol.* **35**, 1884–1890 (2017).
7. Dearnaley, D. *et al.,* Conventional versus hypofractionated high-dose intensity-modulated radiotherapy for prostate cancer: 5-year outcomes of the randomised, non-inferiority, phase 3 CHHiP trial, *Lancet Oncol.* **17**, 1047–1060 (2016).
8. Lee, W. R. *et al.,* Randomized Phase III Noninferiority Study Comparing Two Radiotherapy Fractionation Schedules in Patients With Low-Risk Prostate Cancer, *J. Clin. Oncol.* **34**, 2325–2332 (2016).
9. Moore, J. V., Hendry, J. H. & Hunter, R. D., Dose-incidence curves for tumour control and normal tissue injury, in relation to the response of clonogenic cells. eng, *Radiother. Oncol.* **1**, 143–157 (1983).
10. Walker, A. M. & Suit, H. D., *Choosing between two formulations of a dose/cure function.* eng, 1981.
11. Källman, P, Agren, A & Brahme, A, Tumour and normal tissue responses to fractionated non-uniform dose delivery. eng, *Int. J. Radiat. Biol.* **62**, 249–262 (1992).
12. Gnep, K *et al.,* Haralick textural features on T2-weighted MRI are associated with biochemical recurrence following radiotherapy for peripheral zone prostate cancer, *J. Magn. Reson. Imaging* **45**, 103–117 (2017).

13. Shiradkar, R. *et al.,* Radiomic features from pretreatment biparametric MRI predict prostate cancer biochemical recurrence: Preliminary findings, *J. Magn. Reson. Imaging* **48**, 1626–1636 (2018).

14. Yang, D., Rao, G., Martinez, J., Veeraraghavan, A. & Rao, A., Evaluation of tumor-derived MRI-texture features for discrimination of molecular subtypes and prediction of 12-month survival status in glioblastoma. eng, *Med. Phys.* **42**, 6725–6735 (2015).

15. Nicolò, C. *et al.,* Machine Learning and Mechanistic Modeling for Prediction of Metastatic Relapse in Early-Stage Breast Cancer, *JCO Clin. Cancer Inform.,* 259–274 (2020).

16. Lorenzo, G. *et al.,* Mechanistic modelling of prostate-specific antigen dynamics shows potential for personalized prediction of radiation therapy outcome. eng, *J. R. Soc. Interface* **16**, 20190195 (2019).

17. Klement, R. J., The influence of ketogenic therapy on the 5 R's of radiobiology, *Int. J. Radiat. Biol.* **95**, 394–407 (2019).

18. Milosevic, M. *et al.,* Tumor Hypoxia Predicts Biochemical Failure following Radiotherapy for Clinically Localized Prostate Cancer, *Clin. Cancer Res.* **18**, 2108–2114 (2012).

19. Fraga, A., Ribeiro, R., Príncipe, P., Lopes, C. & Medeiros, R., Hypoxia and Prostate Cancer Aggressiveness: A Tale With Many Endings, *Clin. Genitourin. Cancer* **13**, 295–301 (2015).

20. Horsman, M. R. & Overgaard, J., The impact of hypoxia and its modification of the outcome of radiotherapy, eng, *J. Radiat. Res.* **57**, i90–i98 (2016).

21. Kim, J. J. & Tannock, I. F., Repopulation of cancer cells during therapy: an important cause of treatment failure, *Nat. Rev. Cancer* **5**, 516–525 (2005).

22. Withers, H. R., Taylor, J. M. G. & Maciejewski, B, The hazard of accelerated tumor clonogen repopulation during radiotherapy, *Acta Oncol.* **27**, 131–146 (1988).

23. Wang, J. Z. & Li, X. A., Impact of tumor repopulation on radiotherapy planning, *Int. J. Radiat. Oncol. Biol. Phys.* **61**, 220–227 (2005).

24. Fertil, B & Malaise, E. P., Intrinsic radiosensitivity of human cell lines is correlated with radioresponsiveness of human tumors: Analysis of 101 published survival curves, *Int. J. Radiat. Oncol. Biol. Phys.* **11**, 1699–1707 (1985).

25. Gerweck, L. E., Vijayappa, S., Kurimasa, A., Ogawa, K. & Chen, D. J., Tumor Cell Radiosensitivity Is a Major Determinant of Tumor Response to Radiation, *Cancer Res.* **66**, 8352 –8355 (2006).

26. West, C. M. L., Intrinsic radiosensitivity as a predictor of patient response to radiotherapy, *Brit. J. Radiol.* **68**, 827–837 (1995).

27. Sinclair, W & Morton, R, X-ray sensitiviy during the cell generation cycle of cultured Chinese hamster cells, *Radiat. Res.* **29**, 450–474 (1966).

28. Castedo, M. *et al.,* Cell death by mitotic catastrophe: a molecular definition, *Oncogene* **23**, 2825–2837 (2004).

29. Hall, E. J. & Giaccia, A. J., *Radiobiology for the Radiologist* 7th (Lippincott Williams & Wilkins, 2012).

30. Joiner, M & van der Kogel, A, *Basic Clinical Radiobiology* (Hodder Arnold, London, 2009).

31. Paul-Gilloteaux, P *et al.,* Optimizing radiotherapy protocols using computer automata to model tumour cell death as a function of oxygen diffusion processes, *Sci. Rep.* **7**, 2280 (2017).

32. Espinoza, I, Peschke, P & Karger, C. P., A voxel-based multiscale model to simulate the radiation response of hypoxic tumor, *Med. Phys.* **42.1**, 90–102 (2015).

33. Titz, B & Jeraj, R, An imaging-based tumour growth and treatment response model: investigating the effect of tumour oxygenation on radiation therapy response, *Phys. Med. Biol.* **53(17)**, 4471–4488 (2008).

34. Apeke, S *et al.,* Multi-Scale Modeling and Oxygen Impact on Tumor Temporal Evolution: Application on Rectal Cancer During Radiotherapy, *IEEE Trans. Med. Imag.* **37**, 871–880 (2018).

35. Gago-Arias, A., Sánchez-Nieto, B., Espinoza, I., Karger, C. P. & Pardo-Montero, J., Impact of different biologically-adapted radiotherapy strategies on tumor control evaluated with a tumor response model, *PLOS ONE* **13**, 1–18 (2018).

36. Papoutsoglou, G. S. & Balas, C, Estimation of Neoplasia-Related Biological Parameters Through Modeling and Sensitivity Analysis of Optical Molecular Imaging Data, *IEEE Trans. Biomed. Eng.* **60**, 1241–1249 (2013).

37. Ojeda, D *et al.,* Sensitivity Analysis and Parameter Estimation of a Coronary Circulation Model for Triple-Vessel Disease, *IEEE Trans. Biomed. Eng.* **61**, 1208–1219 (2014).

38. Ojeda, D, Rolle, V. L., Romero-Ugalde, H. M., Gallet, C & Bonnet, J.-L., Sensitivity Analysis of Vagus Nerve Stimulation Parameters on Acute Cardiac Autonomic Responses: Chronotropic, Inotropic and Dromotropic Effects, *PLOS ONE* **11** (2016).

39. Harting, C., Peschke, P., Borkenstein, K. & Karger, C. P., Single-cell-based computer simulation of the oxygen-dependent tumour response to irradiation, *Phys. Med. Biol.* **52**, 4775–4789 (2007).

40. For Connected Learning, C. & Modeling, C.-B., *NetLogo* 2018.

41. Fowler, J. F., The linear-quadratic formula and progress in fractionated radiotherapy, *Brit. J. Radiol.* **62**, 679–694 (1989).

42. Brenner, D. J., The Linear-Quadratic Model Is an Appropriate Methodology for Determining Isoeffective Doses at Large Doses Per Fraction, *Semin. Radiat. Oncol.* **18**, 234–239 (2008).

43. Brand, D. & Yarnold, J., The Linear–Quadratic Model and Implications for Fractionation, *Clin. Oncol.* **31**, 673–677 (2019).

44. Hernandez, A. I., Le Rolle, V, Defontaine, A & Carrault, G, A multiformalism and multiresolution modelling environment: application to the cardiovascular system and its regulation, *Phil. Trans. Math. Phys. Eng. Sci.* **367(1908)**, 4923–4940 (2009).

45. Gleason, D. F. & Mellinger, G. T., Prediction of Prognosis for Prostatic Adenocarcinoma by Combined Histological Grading and Clinical Staging. eng, *J. Urol* **11**, 58–64 (1974).

46. Brierley, J. D., Gospodarowicz, M. K. & Wittekind, C., *TNM Classification of Malignant Tumors* 8th (John Wiley & Sons, Ltd, 2017).

47. Wallace, T. *et al.,* Current Approaches, Challenges and Future Directions for Monitoring Treatment Response in Prostate Cancer, *J. Cancer* **5**, 3–24 (2014).

48. Zaorsky, N. G. *et al.,* Impact of Radiation Therapy Dose Escalation on Prostate Cancer Outcomes and Toxicities. eng, *Am. J. Clin. Oncol.* **41**, 409–415 (2018).

49. Dearnaley, D. P. *et al.,* Escalated-dose versus control-dose conformal radiotherapy for prostate cancer: long-term results from the MRC RT01 randomised controlled trial. eng, *Lancet Oncol.* **15**, 464–473 (2014).

50. Young, M. R. & Yu, J. B., in *Prostate Cancer* (eds Mydlo, J. H. & Godec, C. J. B. T. P. C. S. E.) 413–426 (Academic Press, San Diego, 2016).

51. Fischer-Valuck, B. W., Rao, Y. J. & Michalski, J. M., Intensity-modulated radiotherapy for prostate cancer. eng, *Transl. Androl. Urol.* **7**, 297–307 (2018).

52. Sonke, J.-J., Aznar, M. & Rasch, C., Adaptive Radiotherapy for Anatomical Changes, *Semin. Radiat. Oncol.* **29**, 245–257 (2019).

53. Alasti, H, Petric, M. P., Catton, C. N. & Warde, P. R., Portal imaging for evaluation of daily on-line setup errors and off-line organ motion during conformal irradiation of carcinoma of the prostate. eng, *Int. J. Radiat. Oncol. Biol. Phys.* **49**, 869–884 (2001).

54. Dang, A., Kupelian, P. A., Cao, M., Agazaryan, N. & Kishan, A. U., Image-guided radiotherapy for prostate cancer. eng, *Transl. Androl. Urol.* **7**, 308–320 (2018).

55. Pang, E. P. P. *et al.,* Analysis of intra-fraction prostate motion and derivation of duration-dependent margins for radiotherapy using real-time 4D ultrasound, *Phys. Imag. Radiat. Oncol.* **5**, 102–107 (2018).

56. Mottet, N. *et al.,* EAU-EANM-ESTRO-ESUR-SIOG Guidelines on Prostate Cancer-2020 Update. Part 1: Screening, Diagnosis, and Local Treatment with Curative Intent, eng, *Eur. Urol.* **79**, 243–262 (2021).

57. Mohler, J. L. *et al.,* Prostate Cancer, Version 2.2019, NCCN Clinical Practice Guidelines in Oncology, English, *J. Natl. Compr. Canc. Netw.* **17**, 479–505 (2019).

58. Rozet, F *et al., French ccAFU guidelines - update 2020-2022: prostate cancer* fre, 2020.

59. Jacob, R. *et al.,* Role of prostate dose escalation in patients with greater than 15% risk of pelvic lymph node involvement. eng, *Int. J. Radiat. Oncol. Biol. Phys.* **61**, 695–701 (2005).

60. Stock, R. G., Stone, N. N., Tabert, A, Iannuzzi, C & DeWyngaert, J. K., A dose-response study for I-125 prostate implants. eng, *Int. J. Radiat. Oncol. Biol. Phys.* **41**, 101–108 (1998).

61. Hanks, G. E., Martz, K. L. & Diamond, J. J., The effect of dose on local control of prostate cancer. eng, *Int. J. Radiat. Oncol. Biol. Phys.* **15**, 1299–1305 (1988).

62. Hanks, G. E. *et al.,* Optimization of conformal radiation treatment of prostate cancer: report of a dose escalation study. eng, *Int. J. Radiat. Oncol. Biol. Phys.* **37**, 543–550 (1997).

63. Carlone, M. C., Warkentin, B., Stavrev, P. & Fallone, B. G., Fundamental form of a population TCP model in the limit of large heterogeneity. eng, *Med. Phys.* **33**, 1634–1642 (2006).

64. Niemierko, A & Goitein, M, Implementation of a model for estimating tumor control probability for an inhomogeneously irradiated tumor. eng, *Radiother. Oncol.* **29**, 140–147 (1993).

65. Webb, S & Nahum, A. E., A model for calculating tumour control probability in radiotherapy including the effects of inhomogeneous distributions of dose and clonogenic cell density. eng, *Phys. Med. Biol.* **38**, 653–666 (1993).

66. Nahum, A. & Sanchez, B., Tumor control probability modeling: Basic principles and applications in treatment planning, *Phys. Med.* **17**, 13–23 (2001).

67. Cheung, R., Tucker, S. L., Dong, L. & Kuban, D., Dose-response for biochemical control among high-risk prostate cancer patients after external beam radiotherapy, *Int. J. Radiat. Oncol. Biol. Phys.* **56**, 1234–1240 (2003).

68. Cheung, R. *et al.,* Dose-response characteristics of low- and intermediate-risk prostate cancer treated with external beam radiotherapy. eng, *Int. J. Radiat. Oncol. Biol. Phys.* **61**, 993–1002 (2005).

69. Sanchez-Nieto, B & Nahum, A. E., The delta-TCP concept: a clinically useful measure of tumor control probability. eng, *Int. J. Radiat. Oncol. Biol. Phys.* **44**, 369–380 (1999).

70. Xiong, W, Li, J & Ma, C.-M., Effect of patient variation on standard- and hypo-fractionated radiotherapy of prostate cancer. eng, *Phys. Med. Biol.* **50**, 1483–1492 (2005).

71. Nguyen, P. L. *et al.,* Quantifying the impact of seminal vesicle invasion identified using endorectal magnetic resonance imaging on PSA outcome after radiation therapy for patients with clinically localized prostate cancer. eng, *Int. J. Radiat. Oncol. Biol. Phys.* **59**, 400–405 (2004).

72. McKenna, D. A. *et al.,* Prostate cancer: role of pretreatment MR in predicting outcome after external-beam radiation therapy–initial experience. eng, *Radiology* **247**, 141–146 (2008).

73. Joseph, T. *et al.,* Pretreatment endorectal magnetic resonance imaging and magnetic resonance spectroscopic imaging features of prostate cancer as predictors of response to external beam radiotherapy. eng, *Int. J. Radiat. Oncol. Biol. Phys.* **73**, 665–671 (2009).

74. Riaz, N. *et al.,* Pretreatment endorectal coil magnetic resonance imaging findings predict biochemical tumor control in prostate cancer patients treated with combination brachytherapy and external-beam radiotherapy. eng, *Int. J. Radiat. Oncol. Biol. Phys.* **84**, 707–711 (2012).

75. Haralick, R. M., Shanmugam, K & Dinstein, I., Textural Features for Image Classification, *IEEE Trans. Syst. Man Cybern.* **SMC-3**, 610–621 (1973).

76. Lambin, P. *et al.,* Radiomics: Extracting more information from medical images using advanced feature analysis, *Eur. J. Cancer* **48**, 441–446 (2012).

77. Avanzo, M. *et al.,* Machine and deep learning methods for radiomics, *Med. Phys.* **47**, e185–e202 (2020).

78. Viswanath, S. E. *et al.,* Central gland and peripheral zone prostate tumors have significantly different quantitative imaging signatures on 3 Tesla endorectal, in vivo T2-weighted MR imagery. eng, *J. Magn. Reson. Imaging* **36**, 213–224 (2012).

79. Vignati, A *et al.,* Texture features on T2-weighted magnetic resonance imaging: new potential biomarkers for prostate cancer aggressiveness. eng, *Phys. Med. Biol.* **60**, 2685–2701 (2015).

80. Wibmer, A. *et al.,* Haralick texture analysis of prostate MRI: utility for differentiating non-cancerous prostate from prostate cancer and differentiating prostate cancers with different Gleason scores. eng, *Eur. Radiol.* **25**, 2840–2850 (2015).

81. Fernández, A., Garcia, S., Herrera, F. & Chawla, N. V., SMOTE for learning from imbalanced data: progress and challenges, marking the 15-year anniversary, *J. Artif. Intell. Res.* **61**, 863–905 (2018).

82. Wilson, D. L., Asymptotic Properties of Nearest Neighbor Rules Using Edited Data, *IEEE Trans. Syst. Man Cybern.* **SMC-2**, 408–421 (1972).

83. Hadjicharalambous, M., Wijeratne, P. A. & Vavourakis, V., From tumour perfusion to drug delivery and clinical translation of in silico cancer models, *Methods* (2020).

84. Hamis, S., Powathil, G. G. & Chaplain, M. A. J., Blackboard to Bedside: A Mathematical Modeling Bottom-Up Approach Toward Personalized Cancer Treatments, *JCO Clin. Cancer Inform.,* 1–11 (2019).

85. Borkenstein, K., Levegrün, S. & Peschke, P., Modeling and Computer Simulations of Tumor Growth and Tumor Response to Radiotherapy, *Radiat. Res.* **162**, 71–83 (2004).

86. Powathil, G, Kohandel, M, Sivaloganathan, S, Oza, A & Milosevic, M, Mathematical modeling of brain tumors: effects of radiotherapy and chemotherapy. eng, *Phys. Med. Biol.* **52**, 3291–3306 (2007).

87. Kohandel, M, Kardar, M, Milosevic, M & Sivaloganathan, S, Dynamics of tumor growth and combination of anti-angiogenic and cytotoxic therapies. eng, *Phys. Med. Biol.* **52**, 3665–3677 (2007).

88. Rockne, R *et al.,* Predicting the efficacy of radiotherapy in individual glioblastoma patients in vivo: a mathematical modeling approach. eng, *Phys. Med. Biol.* **55**, 3271–3285 (2010).

89. Belfatto, A *et al.,* Modeling the Interplay Between Tumor Volume Regression and Oxygenation in Uterine Cervical Cancer During Radiotherapy Treatment, *IEEE J. Biomed. Health Inform.* **20**, 596–605 (2016).

90. Belfatto, A *et al.,* Adaptive Mathematical Model of Tumor Response to Radiotherapy Based on CBCT Data, *IEEE J. Biomed. Health Inform.* **20**, 802–809 (2016).

91. Espinoza, I, Peschke, P & Karger, C. P., A model to simulate the oxygen distribution in hypoxic tumors for different vascular architectures, *Med. Phys.* **40** (2013).

92. Titz, B., Kozak, K. R. & Jeraj, R., Computational modelling of anti-angiogenic therapies based on multiparametric molecular imaging data, *Phys. Med. Biol.* **57**, 6079 (2012).

93. Saltelli, A. *et al., Global Sensitivity Analysis. The Primer* (2008).

94. Hu, Z & Shi, P, Sensitivity Analysis for Biomedical Models, *IEEE Trans. Med. Imag.* **29**, 1870–1881 (2010).

95. Sobol', I. M., Sensitivity estmiates for non linear mathematical models, *Math. Modelling Comput. Experiments* **1**, 407–414 (1993).

96. Morris, M, Factorial sampling plans for preliminary computational experiments, *Technometrics* **33.2**, 161–174 (1991).

97. Campolongo, F, Cariboni, J, Saltelli, A & Schoutens, W, *Enhancing the Morris method* in *SAMO 2004* ().

98. Valdagni, R. *et al.,* Is the alpha-beta ratio of prostate cancer really low? A prospective, non-randomized trial comparing standard and hyperfractionated conformal radiation therapy, *Radiotherapy and Oncology* **75**, 74–82 (2005).

99. Walsh, S. & van der Putten, W., A TCP model for external beam treatment of intermediate-risk prostate cancer. *Med. Phys.* **40**, 031709 (2013).

100. Wang, J., Guerrero, M & Li Allen, X, How low is the alpha/beta ratio for prostate cancer?, *Int. J. Radiat. Oncol. Biol. Phys.* **57**, 1116–1121 (2003).

101. Miralbell, R., Roberts, S. A., Zubizarreta, E. & Hendry, J. H., Dose-fractionation sensitivity of prostate cancer deduced from radiotherapy outcomes of 5,969 patients in seven international institutional datasets: alpha/beta = 1.4 (0.9-2.2) Gy, *Int. J. Radiat. Oncol. Biol. Phys.* **82**, 17–24 (2012).

102. Brenner, D. J. & Hall, E. J., Fractionation and protraction for radiotherapy of prostate carcinoma, *Int. J. Radiat. Oncol. Biol. Phys.* **43**, 1095–1101 (1999).

103. Lamprecht, M. R., Sabatini, D. M. & Carpenter, A. E., CellProfiler™: free, versatile software for automated biological image analysis, *BioTechniques* **42**, 71–75 (2007).

104. Dewhirst, M. W. *et al.,* Perivascular Oxygen Tensions in a Transplantable Mammary Tumor Growing in a Dorsal Flap Window Chamber, *Radiat. Res.* **130**, 171–182 (1992).

105. Nichols, M. G. & Foster, T. H., Oxygen diffusion and reaction kinetics in the photodynamic therapy of multicell tumour spheroids, *Phys. Med. Biol.* **39**, 2161–2181 (1994).

106. Evans, N. T. S., Naylor, P. F. D. & Quinton, T. H., The diffusion coefficient of oxygen in respiring kidney and tumour tissue, *Respiration Physiology* **43**, 179–188 (1981).

107. Grote, J, Süsskind, R & Vaupel, P, Oxygen diffusivity in tumor tissue (DS-Carcinosarcoma) under temperature conditions within the range of 20–40°C, *Pflügers Archiv* **372**, 37–42 (1977).

108. Dewhirst, M. W., Secomb, T. W., Ong, E. T., Hsu, R. & Gross, J. F., Determination of Local Oxygen Consumption Rates in Tumors, *Cancer Res.* **54**, 3333 LP –3336 (1994).

109. Rago, R. P., Brazy, P. C. & Wilding, G., Disruption of Mitochondrial Function by Suramin Measured by Rhodamine 123 Retention and Oxygen Consumption in Intact DU145 Prostate Carcinoma Cells, *Cancer Res.* **52**, 6953 LP –6955 (1992).

110. Wagner, B. A., Venkataraman, S. & Buettner, G. R., The rate of oxygen utilization by cells, eng, *Free radical biology & medicine* **51**, 700–712 (2011).

111. Chow, D. C., Wenning, L. A., Miller, W. M. & Papoutsakis, E. T., Modeling pO(2) distributions in the bone marrow hematopoietic compartment. I. Krogh's model, eng, *Biophysical journal* **81**, 675–684 (2001).

112. Gnaiger, E., Steinlechner-Maran, R., Méndez, G., Eberl, T. & Margreiter, R., Control of mitochondrial and cellular respiration by oxygen, *Journal of Bioenergetics and Biomembranes* **27**, 583–596 (1995).

113. Chanrion, M.-A. *et al.,* The influence of the local effect model parameters on the prediction of the tumor control probability for prostate cancer, *Phys. Med. Biol.* **59**, 3019–3040 (2014).

114. Shaffer, R., Pickles, T., Lee, R. & Moiseenko, V., Deriving Prostate Alpha-Beta Ratio Using Carefully Matched Groups, Long Follow-Up and the Phoenix Definition of Biochemical Failure, *Int. J. Radiat. Oncol. Biol. Phys.* **79**, 1029–1036 (2011).

115. Ghobadi, G. *et al.,* Histopathology-derived modeling of prostate cancer tumor control probability: Implications for the dose to the tumor and the gland, *Radiotherapy and Oncology* **119**, 97–103 (2016).

116. Hall, E. J., Roizin-Towle, L. A. & Colvett, R. D., RBE and OER Determinations for Radium and Californium 252, *Radiology* **110**, 699–704 (1974).

117. Palcic, B & Skarsgard, L. D., Reduced Oxygen Enhancement Ratio at Low Doses of Ionizing Radiation, *Radiat. Res.* **100**, 328–339 (1984).

118. Haworth, A *et al.,* Validation of a radiobiological model for low-dose-rate prostate boost focal therapy treatment planning, *Brachytherapy* **12(6)**, 628–636 (2013).

119. Movsas, B. *et al.,* Hypoxia in Human Prostate Carcinoma An Eppendorf PO2 Study, *American journal of Clinical Oncology* **24**, 458–461 (2001).

120. Parker, C. *et al.,* Polarographic electrode study of tumor oxygenation in clinically localized prostate cancer, *Int. J. Radiat. Oncol. Biol. Phys.* **58**, 750–757 (2004).

121. Mayles, P., Nahum, A. & Rosenwald, J. C., *Handbook of Radiotherapy Physics* 1st (CRC Press, 2007).

122. Krock, B. L., Skuli, N. & Simon, M. C., Hypoxia-induced angiogenesis: good and evil, eng, *Genes & cancer* **2**, 1117–1133 (2011).

123. Ojeda, D, *Multi-resolution physiological modeling for the analysis of cardiovascular pathologies* PhD thesis (Univ. Rennes 1, 2013).

124. Potiron, V. A. *et al.,* Improved Functionality of the Vasculature during Conventionally Fractionated Radiation Therapy of Prostate Cancer, *PLOS ONE* **8**, 1–10 (2014).

125. Brenner, D. J. & Hall, E. J., Hypofractionation in prostate cancer radiotherapy, *Transl. Cancer Res.* **7** (2018).

126. Carlson, D. J. *et al.,* Comparison of in vitro and in vivo ratios for prostate cancer, *Phys. Med. Biol.* **49**, 4477–4491 (2004).

127. Bernier, J., Hall, E. J. & Giaccia, A., Radiation oncology: a century of achievements, *Nat. Rev. Cancer* **4**, 737–747 (2004).

128. Abramowitz, M. C. *et al.,* The Phoenix definition of biochemical failure predicts for overall survival in patients with prostate cancer. eng, *Cancer* **112**, 55–60 (2008).

129. Kwak, J. T. *et al.,* Prostate Cancer: A Correlative Study of Multiparametric MR Imaging and Digital Histopathology. eng, *Radiology* **285**, 147–156 (2017).

130. Otani, K. *et al.,* Cell-cycle-controlled radiation therapy was effective for treating a murine malignant melanoma cell line in vitro and in vivo, *Sci. Rep.* **6**, 30689 (2016).

131. Daşu, A., Toma-Daşu, I. & Karlsson, M., Theoretical simulation of tumour oxygenation and results from acute and chronic hypoxia, *Phys. Med. Biol.* **48**, 2829–2842 (2003).

132. Thomlinson, R. H. & Gray, L. H., The histological structure of some human lung cancers and the possible implications for radiotherapy. eng, *Br. J. Cancer* **9**, 539–549 (1955).

133. Bao, B. *et al.,* Hypoxia Induced Aggressiveness of Prostate Cancer Cells Is Linked with Deregulated Expression of VEGF, IL-6 and miRNAs That Are Attenuated by CDF, *PLOS ONE* **7**, 1–11 (2012).

134. Gray, L. H., Conger, A. D., Ebert, M, Hornsey, S & Scott, O. C., The concentration of oxygen dissolved in tissues at the time of irradiation as a factor in radiotherapy. eng, *Brit. J. Radiol.* **26**, 638–648 (1953).

135. Wright, E. A. & Howards-Flanders, P, The influence of oxygen on the radiosensitivity of mammalian tissues. eng, *Acta Radiol.* **48**, 26–32 (1957).

136. Arcangeli, S. *et al.,* Updated Results and Patterns of Failure in a Randomized Hypofractionation Trial for High-risk Prostate Cancer, *Int. J. Radiat. Oncol. Biol. Phys.* **84**, 1172–1178 (2012).

137. Incrocci, L. *et al.,* Hypofractionated versus conventionally fractionated radiotherapy for patients with localised prostate cancer (HYPRO): final efficacy results from a randomised, multicentre, open-label, phase 3 trial, *Lancet Oncol.* **17**, 1061–1069 (2016).

138. Gago-Arias, A., Aguiar, P., Espinoza, I., Sánchez-Nieto, B. & Pardo-Montero, J., Modelling radiation-induced cell death and tumour re-oxygenation: local versus global and instant versus delayed cell death, *Phys. Med. Biol.* **61**, 1204–1216 (2016).

139. Leder, K. *et al.,* Mathematical Modeling of PDGF-Driven Glioblastoma Reveals Optimized Radiation Dosing Schedules, *Cell* **156**, 603–616 (2014).

140. Kirkpatrick, J. P., Meyer, J. J. & Marks, L. B., The Linear-Quadratic Model Is Inappropriate to Model High Dose per Fraction Effects in Radiosurgery, *Semin. Radiat. Oncol.* **18**, 240–243 (2008).

141. Ulman, V. *et al.,* An Objective Comparison of Cell Tracking Algorithms, *Nat. Methods* **14** (2017).

142. Roque, T *et al.,* A DCE-MRI Driven 3-D Reaction-Diffusion Model of Solid Tumor Growth, *IEEE Trans. Med. Imag.* **37**, 724–732 (2018).

143. Warren, D. & Partridge, M., The role of necrosis, acute hypoxia and chronic hypoxia in 18F-FMISO PET image contrast: A computational modelling study, *Phys. Med. Biol.* **61**, 8596–8624 (2016).

144. Adhikarla, V. & Jeraj, R., An imaging-based computational model for simulating angiogenesis and tumour oxygenation dynamics, *Phys. Med. Biol.* **61**, 3885–3902 (2016).

145. Sosa-Marrero, C *et al.,* Towards a reduced in silico model predicting biochemical recurrence after radiotherapy in prostate cancer, *IEEE Trans. Biomed. Eng.* **68**, 2718–2729 (2021).

146. Lalonde, E. *et al.,* Tumour genomic and microenvironmental heterogeneity for integrated prediction of 5-year biochemical recurrence of prostate cancer: a retrospective cohort study, *Lancet Oncol.* **15**, 1521–1532 (2014).

147. Murphy, S. V. & Atala, A., 3D bioprinting of tissues and organs, *Nature Biotechnology* **32**, 773 (2014).

148. Sun, Y. *et al.,* Voxel-wise prostate cell density prediction using multiparametric magnetic resonance imaging and machine learning, *Acta Oncol.* **57**, 1540–1546 (2018).

149. Goldberg, D. E., *Genetic Algorithms in Search, Optimization and Machine Learning* 1st (Addison-Wesley Longman Publishing Co., Inc., USA, 1989).

DOCTORAT BRETAGNE LOIRE / MATHSTIC

UNIVERSITÉ DE RENNES 1

Titre : Modélisation et simulation numérique de croissance tumorale et réponse à la radiothérapie

Mot clés : Modélisation mécaniste, cancer de la prostate, radiothérapie, analyse de sensibilité, récidive biochimique, probabilité de contrôle tumoral

Résumé : La radiothérapie externe (RTE) est le traitement le plus courant du cancer localisé de la prostate. Une dose totale comprise entre 74 et 80 Gy, délivrée en fractions de 2 Gy, est généralement prescrite. Le contrôle local de la tumeur est atteint dans 60 % à 90 % des cas, selon le groupe de risque. Des thérapies modifiées, telles que des traitements hypofractionnés, qui pourraient augmenter ces pourcentages ont été récemment proposées. Cependant, les connaissances sur la réponse des patients à ces nouveaux schémas sont encore limitées. L'objectif principal de cette thèse est donc de simuler numériquement la réponse tumorale à la RTE dans le contexte du cancer de la prostate. À cette fin, dans un premier temps, un modèle mécaniste existant est adapté et différents schémas d'irradiation sont testés. Ensuite, un modèle original intégrant les principaux mécanismes radiobiologiques est développé. Une analyse de sensibilité exhaustive est réalisée et les courbes de probabilité de contrôle tumoral (TCP) du modèle complet et de 15 versions excluant certains mécanismes sont comparées. Un modèle simplifié, équivalent en termes de TCP et de densité cellulaire tumorale est proposé. Enfin, les prédictions de récidive biochimique utilisant le modèle réduit sont comparées à celles d'une approche radiomique classique. Ces travaux ouvrent la voie à l'optimisation clinique des traitements d'irradiation spécifiques aux patients.

Title: *In silico* modelling and simulation of tumour growth and response to radiotherapy

Keywords: Mechanistic modelling, prostate cancer, radiotherapy, sensitivity analysis, biochemical recurrence, tumour control probability

Abstract: External beam radiotherapy (EBRT) is the most common treatment for localised prostate cancer. A total dose between 74 and 80 Gy, delivered in 2 Gy fractions, is typically prescribed. Local tumour control is achieved in 60% to 90% of cases, depending on the risk group. Modified therapies, such as hypofractionated treatments, that may increase these percentages have been recently proposed. However, the knowledge about the response of patients to these new schedules is still limited. The main objective of this thesis is thus to simulate *in silico* the tumour response to EBRT in the context of prostate cancer. For this purpose, as a first step, an existing mechanistic model is adapted and different irradiation schedules are tested. Then, an original model integrating the main radiobiological mechanisms is developed. A thorough sensitivity analysis is performed and tumour control probability (TCP) curves of the comprehensive model and 15 versions excluding certain mechanisms are compared. A simplified model, equivalent in terms of TCP and tumour cell density is proposed. Finally, biochemical recurrence predictions using the reduced model are compared with those of a conventional radiomics approach. This work paves the way for the clinical optimisation of patient-specific irradiation treatments.